Perturbation theory for the $\pi^+\pi^-$ atom

V. E. Lyubovitskij[a)]
Bogoliubov Laboratory of Theoretical Physics, JINR, 141980 Dubna, Russia

E. Z. Lipartia[b)]
Laboratory for Computational Technique and Automation, JINR, 141980 Dubna, Russia; IHEP, Tbilisi State University, 380086 Tbilisi, Georgia

A. G. Rusetsky[c)]
Bogoliubov Laboratory of Theoretical Physics, JINR, 141980 Dubna, Russia; IHEP, Tbilisi State University, 380086 Tbilisi, Georgia

(Submitted 4 November 1997)
Pis'ma Zh. Éksp. Teor. Fiz. **66**, No. 12, 747–752 (25 December 1997)

A perturbation-theory framework is developed for calculation of the characteristics of the $\pi^+\pi^-$ atom on the basis of the field-theoretic Bethe–Salpeter approach. A closed expression is obtained for the first-order correction to the lifetime of the $\pi^+\pi^-$ atom. © *1997 American Institute of Physics.* [S0021-3640(97)00124-2]

PACS numbers: 36.10.Gv, 31.15.Md

Experimental studies of the hadronic atoms $\pi\pi$ (Ref. 1), πp, and πd (Ref. 2) have now been carried out. The first estimate of the lifetime of the $\pi^+\pi^-$ atom was given in Ref. 1. The DIRAC collaboration is now designing an experiment at CERN for the high-precision measurement of the lifetime of $\pi^+\pi^-$ atoms. This experiment might provide a decisive improvement in the direct determination of the difference of the S-wave $\pi\pi$ scattering lengths and thus serve as a valuable test for the predictions of chiral perturbation theory.[3] In view of these experiments there arises a need for a theoretical framework which would enable one to calculate the characteristics of such atoms with a high accuracy on the basis of the ideas of standard model.

The theoretical study of hadronic atoms starts from Refs. 4–6, where the nonrelativistic formulas for the lifetime of a hadronic atom and the shift of its energy levels due to the strong interactions are obtained, which relate these quantities to the strong scattering lengths. The expression for the width Γ_0 of the $\pi^+\pi^-$ atom in the ground state is

$$\Gamma_0=\frac{16\pi}{9}\sqrt{\frac{2\Delta m_\pi}{m_\pi}}(a_0^0-a_0^2)^2\phi_0^2, \tag{1}$$

where Δm_π is the $m_{\pi^\pm}-m_{\pi^0}$ mass difference, and ϕ_0 is the value of the Coulomb wave function of pionium at the origin.

The approach to the problem of hadronic atoms which was developed in Ref. 4 makes use of a general characteristic feature of hadronic atoms — the factorization of strong and electromagnetic interactions. Formula (1) demonstrates this factorization property explicitly, expressing the atom lifetime as a product of two factors: the Coulomb

wave function at the origin, and the strong interaction factor, which is completely concentrated in the $\pi\pi$ strong scattering lengths.

The problem of evaluation of the electromagnetic and strong corrections to the basic formula (1) within different approaches is addressed in Refs. 7–14. For a brief review see Ref. 12. In that paper we derived the relativistic analog of formula (1) within the Bethe–Salpeter (BS) approach, taking into account the first-order correction due to the displacement of the bound state pole position by the strong interactions (strong correction). This correction was found to be of relative order 10^{-3}. It should be stressed that the field-theoretical approaches[10,12–14] to the problem, unlike the potential treatment,[7,11] do not refer to the concept of a phenomenological strong interaction $\pi\pi$ potential, which is a source of additional ambiguity in calculations of the characteristics of hadronic atoms. In the former approaches these characteristics are expressed directly in terms of the underlying strong-interaction (chiral) Lagrangian, and the results can be compared to experiment, providing a consistent test of the predictions of the chiral theory.

In the present work we suggest a relativistic perturbation-theory framework for the calculation of the energy levels and lifetime of hadronic atoms. The main purpose of this work is to demonstrate the possibility (not only in potential scattering theory but in the BS treatment as well) of the clear-cut factorization of the strong and electromagnetic interactions in the observable characteristics of hadronic atoms, thus avoiding the double-counting problem in the calculation of these quantities. It should be noted that the suggested approach allows one to calculate the strong and electromagnetic corrections in all orders of perturbation theory. At the present stage we apply the general formalism to the calculation of the first-order strong and electromagnetic corrections to the pionium lifetime. The results for the strong corrections obtained in Ref. 12 are reproduced in these calculations.

Our approach is based on a perturbation expansion about the solution of the BS equation with a Coulomb kernel similar to that introduced in Ref. 15:

$$V_C(\mathbf{p},\mathbf{q})=\sqrt{w(\mathbf{p})}\,\frac{4im_\pi e^2}{(\mathbf{p}-\mathbf{q})^2}\,\sqrt{w(\mathbf{q})},\quad w(\mathbf{p})=\sqrt{m_\pi^2+\mathbf{p}^2}. \tag{2}$$

The factor $\sqrt{w(\mathbf{p})w(\mathbf{q})}$ introduced in the kernel (2) enables one to reduce the BS equation with such a kernel to the exactly solvable Schrödinger equation with the Coulomb potential. Then the exact solution of the BS equation with this kernel is written in the form

$$\psi_C(p)=iG_0(M^\star;p)\,4\sqrt{w(\mathbf{p})}\,\frac{4\pi\alpha m_\pi\phi_0}{\mathbf{p}^2+\gamma^2},\quad \overline{\psi}_C(p)=\psi_C(p), \tag{3}$$

where $\gamma=m_\pi\alpha/2$, $M^{\star 2}=m_\pi^2(4-\alpha^2)$ is the eigenvalue corresponding to the unperturbed ground-state solution, and G_0 denotes the free Green′s function of the $\pi^+\pi^-$ pair. The exact Green′s function corresponding to the Coulomb kernel (2) is given by the well-known expression

$$G_C(P^\star;p,q)=(2\pi)^4\delta^{(4)}(p-q)G_0(P^\star;p)+G_0(P^\star;p)T_C(E^\star;\mathbf{p},\mathbf{q})G_0(P^\star;q). \tag{4}$$

Here T_C is given by

$$T_C(E^\star;\mathbf{p},\mathbf{q})=16i\pi m_\pi\alpha\sqrt{w(\mathbf{p})w(\mathbf{q})}\left[\frac{1}{(\mathbf{p}-\mathbf{q})^2}+\int_0^1\frac{\nu d\rho\rho^{-\nu}}{D(\rho;\mathbf{p},\mathbf{q})}\right], \tag{5}$$

$$D(\rho;\mathbf{p},\mathbf{q})=(\mathbf{p}-\mathbf{q})^2\rho-\frac{m_\pi}{4E^\star}\left(E^\star-\frac{\mathbf{p}^2}{m_\pi}\right)\left(E^\star-\frac{\mathbf{q}^2}{m_\pi}\right)(1-\rho)^2,$$

where $\nu=\alpha\sqrt{m_\pi/(-4E^\star)}$ and $E^\star=(P^{\star 2}-4m_\pi^2)/(4m_\pi)$.

The full BS equation for the $\pi^+\pi^-$ atom wave function $\chi(p)$ is written as

$$G_0^{-1}(P;p)\chi(p)=\int\frac{d^4k}{(2\pi)^4}V(P;p,q)\chi(q), \tag{6}$$

where $V(P;p,q)$ denotes the full BS kernel, which is constructed from the underlying (effective) Lagrangian according to the general rules and includes all the strong and electromagnetic two-charged-pion irreducible diagrams. In particular, it contains the diagrams with two neutral pions in the intermediate state which govern the decay of the $\pi^+\pi^-$ atom into $\pi^0\pi^0$. Note that in addition $V(P;p,q)$ contains the two-particle reducible charged-pion self-energy diagrams attached to the outgoing pionic legs (with the relative momentum q). These diagrams arise in the definition of the kernel $V(P;p,q)$ because the free two-particle Green′s function instead of the dressed one is used in the left-hand side of Eq. (6). The c.m. momentum squared P^2 of the atom has a complex value, corresponding to the fact that the atom is an unstable system. According to the conventional parametrization, we can write $P^2=\overline{M}^2=M^2-iM\Gamma$ where M denotes the ''mass'' of the atom, and Γ is the atom decay width.

The full four-point Green's function $G(P)$ for the kernel V has a pole in the complex P^2 plane at the bound-state energy. The relation between the exact wave function $\chi(p)$ and the Coulomb wave function ψ_C is given by[12]

$$\langle\chi|=C\langle\psi_C|G_C^{-1}(P^\star)G(P),\quad P^{\star 2}\to M^{\star 2},P^2\to\overline{M}^2 \tag{7}$$

where C is the normalization constant. In what follows we assume that the limiting procedure is performed with the use of the prescription[12] $P^{\star 2}=M^{\star 2}+\lambda$, $P^2=\overline{M}^2+\lambda$, $\lambda\to 0$. The validity of Eq. (7) can be trivially checked by extracting the bound-state pole in $G(P)$ and using the BS equation for ψ_C.

In order to perform the perturbation expansion of the bound-state characteristics M and Γ about the unperturbed values, we, as in Ref. 12, split the full BS kernel V into two parts as $V=V_C+V'$ and consider V' as a perturbation. It can be shown that Eq. (7) is equivalent to

$$\langle\chi|=-C^{-1}\langle\psi_C|[1+(\Delta G_0^{-1}-V')G_RQ]^{-1},\quad \Delta G_0^{-1}=G_0^{-1}(P)-G_0^{-1}(P^\star). \tag{8}$$

With the use of Eq. (8) the following identity is easily obtained

$$\langle\psi_C|[1+(\Delta G_0^{-1}-V')G_RQ]^{-1}(\Delta G_0^{-1}-V')|\psi_C\rangle=0, \tag{9}$$

which is an exact relation and serves as a basic equation for performing the perturbation expansion for the bound-state energy.

In Eqs. (8) and (9) G_RQ stands for the regular (pole-subtracted) part of the Coulomb Green's function (4), projected onto the subspace orthogonal to the ground-state unperturbed solution. This quantity can be further split into two pieces, according to $G_RQ = G_0(M^\star) + \delta G$. Here the function δG corresponds to the ladder of the exchanged Coulomb photons and thereby contains explicit powers of α. It is given by the following expression:

$$\delta G = i\sqrt{w(\mathbf{p})w(\mathbf{q})}\left[\Phi(\mathbf{p},\mathbf{q}) - S(\mathbf{p})S(\mathbf{q})\frac{8}{M^\star}\frac{\partial}{\partial M^\star}\right]G_0(M^\star,p)G_0(M^\star,q),$$

$$\Phi(\mathbf{p},\mathbf{q}) = 16\pi m_\pi \alpha\left[\frac{1}{(\mathbf{p}-\mathbf{q})^2} + I_R(\mathbf{p},\mathbf{q})\right] + (m_\pi\alpha)^{-2}S(\mathbf{p})S(\mathbf{q})R(\mathbf{p},\mathbf{q}), \tag{10}$$

$$S(\mathbf{p}) = 4\pi m_\pi \alpha \phi_0(\mathbf{p}^2+\gamma^2)^{-1}, \quad R(\mathbf{p},\mathbf{q}) = 25 - \sqrt{\frac{8}{\pi m_\pi \alpha}}\,[S(\mathbf{p})+S(\mathbf{q})] + \cdots,$$

where the ellipses stand for the higher-order terms in α. The integral $I_R(\mathbf{p},\mathbf{q})$ is given by

$$I_R(\mathbf{p},\mathbf{q}) = \int_0^1 \frac{d\rho}{\rho}[D^{-1}(\rho;\mathbf{p},\mathbf{q}) - D^{-1}(0;\mathbf{p},\mathbf{q})], \quad E^\star = -\frac{1}{4}m_\pi\alpha^2. \tag{11}$$

Equation (8) expresses the exact BS wave function of the atom in terms of the unperturbed wave function via the perturbation expansion in the perturbation potential V'. This potential consists of the following pieces.

1. The purely strong part, which is isotopically invariant. This part survives when the electromagnetic interactions are ''turned off'' in the Lagrangian.

2. A part containing the diagrams with finite mass insertions, which are responsible for the $m_{\pi^\pm} - m_{\pi^0}$ electromagnetic mass difference.

3. A part containing the exchanges of one, two, ... virtual photons and an arbitrary number of strong interaction vertices.

Note that the terms 1 and 2 are the more important, for the following reasons. The first term includes the strong interactions, which are responsible for the decay of the pionium. The second term makes this decay kinematically allowed due to the finite difference of the charged and neutral pion masses. Consequently, it seems to be natural to consider pieces 1 and 2 together. We refer to the corresponding potential as V_{12}. The T matrix corresponding to the potential V_{12} is defined by $T_{12}(P) = V_{12}(P) + V_{12}(P)G_0(P)T_{12}(P)$. The rest of the potential V' is referred to as $V_3 = V' - V_{12}$. In what follows we restrict ourselves to the first order in the fine structure constant α, i.e., we consider the diagrams with only one virtual photon contained in V_3.

Returning to the basic equation (9), we expand it in a perturbation series, treating V_3 and δG as perturbations. Meanwhile we expand ΔG_0^{-1} in a Taylor series in $\delta M = \overline{M} - M^\star$ and make the substitution $\overline{M} = M^\star + \Delta E^{(1)} + \Delta E^{(2)} - i/2\,\Gamma^{(1)} - i/2\Gamma^{(2)} + (8M^\star)^{-1}\Gamma^{(1)^2} + \cdots$.

Restricting ourselves to the first order of the perturbation expansion, we arrive at the following relations:

$$\Delta E^{(1)}=\mathrm{Re}\left(\frac{i}{2M^\star}\frac{T_{12}}{m_\pi}\phi_0^2\right),\quad -\frac{1}{2}\Gamma^{(1)}=\mathrm{Im}\left(\frac{i}{2M^\star}\frac{T_{12}}{m_\pi}\phi_0^2\right). \tag{12}$$

Hereafter we use the local approximation for T_{12}, assuming that it does not depend on the relative momenta. Equations (12) coincide with the well-known Deser-type formulas for the energy-level shift and lifetime.[4] Note that on the mass shell

$$\mathrm{Re}(iT_{12})\sim T(\pi^+\pi^-\to\pi^+\pi^-),\quad \mathrm{Im}(iT_{12})\sim\sqrt{\Delta m_\pi}|T(\pi^+\pi^-\to\pi^0\pi^0)|^2. \tag{13}$$

If we assume $V_3=\delta G=0$, we arrive at the result

$$\frac{\Gamma^{(2)}}{\Gamma^{(1)}}=-\frac{9}{8}\frac{\Delta E^{(1)}}{E_1}-0.763\alpha,\quad \text{where } E_1=-\frac{1}{4}m_\pi\alpha^2. \tag{14}$$

The first term of this expression, called the ''strong correction,'' was obtained in our previous paper.[12] However, as opposed to the present derivation, in Ref. 12, we used the Born approximation for the calculation of $\Delta E^{(1)}$, i.e., in Eq. (12) T_{12} was replaced by V_{12}. The second term comes from the relativistic normalization factor $\sqrt{w(\mathbf{p})w(\mathbf{q})}$ in the kernel (2) and corresponds to the relativistic modification of the pionium Coulomb wave function $|\int d^4p/(2\pi)^4\psi_C(p)|^2=\phi_0^2(1-0.381\alpha)^2/m_\pi$. Since this correction comes from the Coulomb wave function of the atom, it does not depend on the parameters of the strong $\pi\pi$ interaction, and for this reason it was neglected in Ref. 12.

Inclusion of δG introduces a correction in the lifetime due to the exchange of an infinite number of Coulomb photons. The integrals emerging in the calculation of this correction are ultraviolet convergent, containing, however (in complete analogy with a well-known result from nonrelativistic scattering theory), an infrared enhancement $\alpha\ln\alpha$ which stems from the one-photon exchange piece in Eq. (5). Collecting all terms together and using Eqs. (12) for relating Im T_{12} to $\Delta E^{(1)}$, we finally arrive at the first-order correction to the pionium rate,

$$\Gamma=\Gamma_0\Bigg(1+\underbrace{\left(-\frac{9}{8}\frac{\Delta E^{(1)}}{E_1}\right)}_{\text{strong}}+\underbrace{(-0.763\alpha)}_{\text{relativistic w.f.}}+\underbrace{(1/2+2.694-\ln\alpha)\frac{\Delta E^{(1)}}{E_1}}_{\text{Coulomb photon exchanges}}+\delta_M$$
$$-(M^\star\Gamma^{(1)})^{-1}\mathrm{Re}\langle\psi_C|(1+T_{12}G_0(M^\star))V_3(1+G_0(M^\star)T_{12})|\psi_C\rangle\Bigg), \tag{15}$$

where δ_M stands for the mass shift correction[14] and the last term collects the radiative corrections[13,14] (including the retardation correction,[10] the correction due to vacuum polarization,[8] etc.). In Eq. (15) all the first-order strong and electromagnetic corrections are given in closed form, thus avoiding any difficulties connected with the double-counting problem. The kernel which appears in the last term, $(1+T_{12}G_0(M^\star))V_3(1+G_0(M^\star)T_{12})$, is constructed from the underlying Lagrangian

with the use of the conventional Feynman diagrammatic technique. A detailed reexamination of the above-mentioned corrections within the BS approach will be addressed in our forthcoming publications.

In order to estimate the size of the calculated corrections to the pionium lifetime (Eq. (15)) we have used the following value of the singlet scattering length: $m_\pi(2a_0^0+a_0^2)=0.49$, corresponding to a value $\Delta E^{(1)}/E_1=0.24\%$. The first, second, and third terms then contribute, respectively, -0.26%, -0.55%, and $+1.85\%$, and the total contribution amounts to $\sim 1\%$ of the decay width (apart from the mass shift and radiative corrections). The largest contribution comes from the $\alpha\ln\alpha$ term in Eq. (15).

We thank J. Gasser, M. A. Ivanov, E. A. Kuraev, H. Leutwyler, P. Minkowski, L. L. Nemenov and H. Sazdjian for helpful discussions, comments, and remarks. A. G. R. thanks Bern University, where part of this work was completed, for hospitality. This work was supported in part by INTAS Grant 94-739 and by the Russian Fund for Fundamental Research (RFFR) under contract 96-02-17435-a.

[a)]e-mail: lubovit@thsun1.jinr.dubna.su
[b)]e-mail: lipartia@thsun1.jinr.dubna.su
[c)]e-mail: rusetsky@thsun1.jinr.dubna.su

---

[1] L. G. Afanasyev, A. S. Chvyrov, O. E. Gorchakov *et al.*, Phys. Lett. B **308**, 200 (1993); Phys. Lett. B **338**, 478 (1994).
[2] D. Sigg, A. Badertscher, M. Bogdan *et al.*, Phys. Rev. Lett. **75**, 3245 (1995); D. Chattelbard, J.-P. Egger, E. Jeannet *et al.*, Phys. Rev. Lett. **74**, 4157 (1995).
[3] J. Gasser and H. Leutwyler, Ann. Phys. (N.Y.) **158**, 142 (1984).
[4] S. Deser, M. L. Goldberger, K. Baumann *et al.*, Phys. Rev. **96**, 774 (1954).
[5] J. L. Uretsky and T. R. Palfrey, Phys. Rev. **121**, 1798 (1961).
[6] S. M. Bilenky, Nguen Van Hiew, L. L. Nemenov *et al.*, Yad. Fiz. **10**, 812 (1969) [Sov. J. Nucl. Phys. **10**, 812 (1969)].
[7] T. L. Trueman, Nucl. Phys. **26**, 57 (1961).
[8] G. V. Efimov, M. A. Ivanov and V. E. Lyubovitskiĭ, Yad. Fiz. **44**, 460 (1986) [Sov. J. Nucl. Phys. **44**, 296 (1986)].
[9] A. A. Bel'kov, V. N. Pervushin and F. G. Tkebuchava, Yad. Fiz. **44**, 466 (1986) [Sov. J. Nucl. Phys. **44**, 300 (1986)].
[10] Z. Silagadze, JETP Lett. **60**, 689 (1994).
[11] U. Moor, G. Rasche and W. S. Woolcock, Nucl. Phys. A **587**, 747 (1995).
[12] V. Lyubovitskij and A. Rusetsky, Phys. Lett. B **389**, 181 (1996).
[13] E. A. Kuraev, Preprint http://xxx.lanl.gov/hep-ph/9702327.
[14] H. Jallouli and H. Sazdjian, Preprint IPNO/TH 97-01 (1997).
[15] R. Barbieri and E. Remiddi, Nucl. Phys. B **141**, 78 (1983).

Published in English in the original Russian journal. Edited by Steve Torstveit.

Self-similar potentials and Ising models

I. Loutsenko[a)]
Centre de Recherches Mathématiques, Université de Montréal, H3C 3J7 Montréal (Québec), Canada

V. Spiridonov[b)]
Centre de Recherches Mathématiques, Université de Montréal, H3C 3J7 Montréal (Québec), Canada; Laboratory of Theoretical Physics, JINR, 141980 Dubna, Moscow District, Russia

(Submitted 4 September 1997; resubmitted 30 October 1997)
Pis'ma Zh. Éksp. Teor. Fiz. **66**, No. 12, 753–758 (25 December 1997)

A new link between soliton solutions of integrable nonlinear equations and one-dimensional Ising models is established. Translational invariance of the spin lattice associated with the KdV equation is related to self-similar potentials of the Schrödinger equation. This gives antiferromagnets with exponentially decaying interaction between the spins. The partition function is calculated exactly for a uniform magnetic field and two discrete values of the temperature. © *1997 American Institute of Physics.* [S0021-3640(97)00224-7]

PACS numbers: 05.50.+q

The one-dimensional Schrödinger equation

$$L\psi(x)\equiv-\psi_{xx}(x)+u(x)\psi(x)=\lambda\psi(x) \tag{1}$$

lies at the foundation of quantum mechanics and the theory of solitons. The class of potentials $u(x)$ for which the spectrum and eigenfunctions of the operator L are known in closed form is of particular interest. It includes simple potentials related to the Gauss hypergeometric function (for a review, see Ref. 1), finite-gap potentials, and potentials whose discrete spectra consist of a number of arithmetic or geometric progressions (see Refs. 2 and 3 and references cited therein). The latter potentials appear after a self-similar reduction of the factorization chain or the chain of Darboux transformations. In this note we discuss the relationship of the self-similar potentials to the one-dimensional Ising-type spin chain models. Below we use the language of the soliton theory described, e.g., in Refs. 4 and 5.

It is well known that if the potential $u(x,t)$ and the wave function $\psi(x,t)$ in Eq. (1) depend on the ''time'' t in such a way that

$$\psi_t(x,t)=B\psi(x,t),\quad B\equiv-4\partial_x^3+6u(x,t)\partial_x+3u_x(x,t), \tag{2}$$

then the condition of compatibility of Eqs. (1) and (2), $L_t=[B,L]$, is equivalent to the Korteweg–de Vries (KdV) equation $u_t+u_{xxx}-6uu_x=0$. The N-soliton solution of this equation can be represented in the form $u(x,t)=-2\partial_x^2\ln\tau_N(x,t)$, where $\tau_N=\det C$ is the determinant of the matrix

$$C_{ij}=\delta_{ij}+\frac{2\sqrt{k_i k_j}}{k_i+k_j}e^{(\theta_i+\theta_j)/2},\quad \theta_i=k_i x-k_i^3 t+\theta_i^{(0)}. \tag{3}$$

Here k_i are the amplitudes of solitons related to the bound state energies of (1), $\lambda_i=-k_i^2/4$, and $\theta_i^{(0)}/k_i$ are the zero-time phases. The ordering $0<k_N<\ldots<k_1$ is assumed. Equivalently, this τ function can be rewritten in the form[4,5]

$$\tau_N=\sum_{\mu_i=0,1}\exp\left(\sum_{1\leqslant i<j\leqslant N}A_{ij}\mu_i\mu_j+\sum_{1\leqslant i\leqslant N}\theta_i\mu_i\right), \tag{4}$$

where the phase shifts A_{ij} are determined by the formula

$$e^{A_{ij}}=\frac{(k_i-k_j)^2}{(k_i+k_j)^2}. \tag{5}$$

There are generalizations of expressions (3)–(5) such that the corresponding $u(x,t,\ldots)$ satisfy higher order members of the KdV hierarchy, sine-Gordon, Kadomtsev–Petviashvili (KP), Toda, and some other integrable equations.[4]

We start from the observation that expression (4) has a nice interpretation within statistical mechanics. Namely, for $\theta_i=\theta^{(0)}=$ const it defines the grand partition function of the lattice gas model.[6] In this case the μ_i play the role of filling factors of the lattice sites by mutually repulsive molecules, $\theta^{(0)}$ is proportional to the chemical potential, and the A_{ij} are proportional to the interaction energy between the ith and jth molecules.

Simultaneously, the function (4) is closely related to the partition function of the one-dimensional Ising model:[6]

$$Z_N=\sum_{\sigma_i=\pm 1}e^{-\beta E},\quad E=\sum_{i<j}J_{ij}\sigma_i\sigma_j-\sum_{1\leqslant i\leqslant N}H_i\sigma_i, \tag{6}$$

where N is the number of spins $\sigma_i=\pm 1$, $J_{ij}=J_{ji}$ is the coupling between ith and jth spins, H_i is the external magnetic field, and $\beta=1/kT$ is the inverse temperature. Indeed, let us introduce into (4) the spin variables via the substitution $\mu_i=(\sigma_i+1)/2$. After some simple calculations one finds

$$\tau_N=e^{\Phi}Z_N,\quad \Phi=\tfrac{1}{4}\sum_{i<j}A_{ij}+\tfrac{1}{2}\sum_{1\leqslant j\leqslant N}\theta_j, \tag{7}$$

provided that

$$A_{ij}=-4\beta J_{ij},\quad \theta_i=2\beta\left(H_i+\sum_{1\leqslant j\neq i\leqslant N}J_{ij}\right). \tag{8}$$

As a result, one arrives at an interesting fact: from a given N-soliton τ function of the KdV equation (4), one recovers the partition function of the N-spin Ising model (7). The τ function is defined only up to a gauge factor $\exp(ax+b)$, and the function (7) fits this freedom. Therefore one may identify (6) as the N-soliton τ function itself for the specific exchange interaction (5). This fact alone does not help much in the evaluation of Z_N. However, the recursive way of building N-soliton potentials with the help of Darboux

transformations or the factorization method appears to be quite useful. Let us give the representation of Z_N following from the Wronskian form of τ_N (Refs. 7 and 8):

$$Z_N=\frac{2^{N(N+1)/2}W_N}{\prod_{i<j}(k_i^2-k_j^2)^{1/2}},\quad W_N=\det\left(\frac{d^{i-1}\Psi_j}{dx^{i-1}}\right), \tag{9}$$

where $\Psi_{2j-1}=\cosh\beta H_{N-2j+2}$, $\Psi_{2j}=\sinh\beta H_{N-2j+1}$. The dependence of H_j on the soliton parameters is read from (8).

The factorization method transforms a given potential $u_j(x)=f_j^2(x)-f_{jx}(x)+\lambda_j$ with some discrete spectrum to the potential $u_{j+1}(x)=u_j(x)+2f_{jx}(x)$ containing an additional (the lowest) bound state with the prescribed energy λ_j. Within the Ising-model context, this corresponds to the extension of the lattice by one more site. Then the infinite-soliton potentials correspond to the thermodynamic limit $N\to\infty$. Characterization of a general τ_N at $N\to\infty$ is a challenging problem, but for the specific choice of parameters $k_i,\theta_i^{(0)}$ this function can be analyzed to some extent through the basic infinite chain of equations[1]

$$(f_j(x)+f_{j+1}(x))_x+f_j^2(x)-f_{j+1}^2(x)=\rho_j\equiv\lambda_{j+1}-\lambda_j,\quad j\in\mathbf{Z}. \tag{10}$$

In general both τ_N and Z_N diverge in the limit $N\to\infty$. If the corresponding solutions of (10) are finite, then the divergences gather into the gauge factor.

A key observation of the present work is that the simplest physical constraints imposed upon the form of spin interactions J_{ij} of the infinite Ising chain select the potentials with a discrete spectrum composed from a number of geometric progressions. First, let us demand that all the spins are situated on equal distance from each other and that they are identical, i.e., that there is a translational invariance, $A_{i+1,j+1}=A_{ij}$. This means that the interaction intensities A_{ij} depend only on the distance between the sites $|i-j|$, $A_{ij}=A(|i-j|)$. Such a natural constraint has the *unique* solution

$$k_i=k_1q^{i-1},\quad q=e^{-2\alpha},\quad A_{ij}=2\ln|\tanh\alpha(i-j)|, \tag{11}$$

where $\alpha>0$ is an arbitrary constant. For finite N this spectrum corresponds to reflectionless potentials with the eigenvalues condensing near $\lambda=0$. For $q>1$, one should write $k_i=k_1q^{-i+1}$ for correct ordering of k_i. (The exponentially growing spectrum is formally obtained for purely imaginary k_1 and $q>1$, but the corresponding potential contains singularities.) In the limit $N\to\infty$, one gets an infinite soliton potential with the discrete spectrum $\lambda_j=-k_1^2q^{2(j-1)}/4$ describing a specific semi-infinite spin chain (j takes only positive values). As $q^j\to0$ for $j\to\infty$, the x and t depending part of the magnetic field is decaying exponentially from the edge of the lattice. The limits $x,t\to\infty$ correspond to the growing penetration depth of the magnetic field inside the bulk. Note that one can analyze boundary effects by working with a difference of the free energy at two fixed values of the magnetic field.

Since $0<|\tanh\alpha(i-j)|<1$, one has $J_{ij}>0$, i.e., an antiferromagnetic interaction (the spins are not aligned in the ground state). It has nice physical characteristics — its intensity falls exponentially fast with the distance between the sites. It is well known that the one-dimensional systems with finite-range interactions do not have phase transitions

at nonzero temperature. There is a model with the exponential interaction $J_{ij}=-\gamma|J_0|e^{-\gamma|i-j|}$ solved in the limit $\gamma\to 0$ by M. Kac.[9] This limit corresponds to the very weak but long-range interaction and exhibits a phase transition with the Van der Waals equation of state.

There should be some relation of our model to the Kac one, but it is not clear whether there exists a direct connection. A similar molecular-approximation limit is reached in our case if $\alpha\to 0$. Formally the $A_{ij}\propto J_{ij}/kT$ diverge in this limit. If we renormalize the interaction constants as $J_{ij}^{\rm ren}=J_{ij}(q^{-1}-q)$ and the temperature as $T_{\rm ren}=T(q^{-1}-q)$, then the maximal interaction energy of a single ith spin (determined by the summation of $J_{ij}^{\rm ren}$ over j) will be finite for $\alpha\to 0$ (or $q\to 1$). Therefore the limit $q\to 1$ corresponds to the *long-range interaction* model *at low temperature*. Note that one should simultaneously rescale the magnetic field $H=h/(q^{-1}-q)$ to imitate the change of the temperature.

The particular form of the renormalization factor $q^{-1}-q$ was chosen so as to recover the interaction $J_{ij}^{\rm ren}\propto\delta_{i+1,j}$ in the limit $q\to 0$. If one takes h as a real magnetic field then one gets the nearest-neighbor interaction Ising model at high temperature. If the magnetic field is not rescaled, then the $q\to 0$ limit corresponds to completely noninteracting spins. Thus our formalism allows us to analyze the partition function on two-dimensional planes in the space of variables (T,H,q). Unfortunately, for fixed q the temperature is fixed as well, and we may normalize the ''KdV temperature'' to $kT=1$.

The discrete spectrum does not characterize completely even the reflectionless potentials — one has to fix the phases θ_i. Only for a special choice of these parameters does one arrive at self-similar potentials. For example, the simplest case is determined by the condition that the scaling of x and t by q and q^3 respectively is equivalent to removing one soliton. Formally this corresponds to the constraint $\theta_i(qx,q^3t)=\theta_{i+1}(x,t)$, assuming the choice $\theta_i^{(0)}=\theta^{(0)}=$ const. However, τ_N, Z_N, and Φ in (7) diverge for $N\to\infty$, and a more careful analysis is thus called for. Note that the shift of H_i in (8) remains finite, and it becomes a fixed constant for $i\to\infty$. This means that in the thermodynamic limit the zero chemical potential in the lattice-gas partition function corresponds to a fixed nonzero magnetic field in the Ising model, and, vice versa, zero magnetic field corresponds to a prescribed value of the chemical potential.

Let us consider now the ''M-color'' Ising model for which the chain is formed by embedded sublattices in which blocks of M spins with different distances between them are periodically repeated. Within each of this block the distances between spins are not equal, so that the interaction constants between the first M sites are given by arbitrary (random) numbers. Equivalently, one may think that at equidistant lattice points one has particles with different magnetic moments, i.e., some kind of ferrimagnetic interaction. Such physical constraints are bound to the condition $A_{i+M,j+M}=A_{ij}$, which leads to a constraint on the soliton energies in the form $k_{j+M}=qk_j$, generalizing the previous case. For a specific choice of the phases $\theta_{i+M}^{(0)}=\theta_i^{(0)}$ one arrives at general self-similar potentials, for which one has $\theta_i(qx,q^3t)=\theta_{i+M}(x,t)$. The rigorous definition of these potentials for fixed time is given by the constraints[2]

$$f_{j+M}(x)=qf_j(qx),\quad \rho_{j+M}=q^2\rho_j \tag{12}$$

imposed upon the chain (10). The system of mixed differential and q-difference equa-

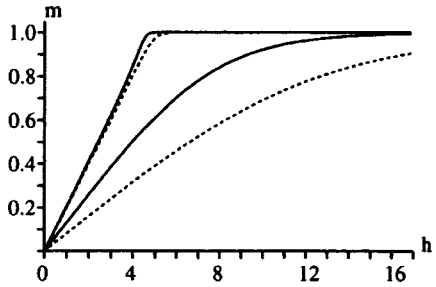

FIG. 1. Dependence of the magnetization $m(h)$ on h for the KdV case $n=1$ (dotted curves) and for the BKP case $n=2$ (solid curves). The lower curves correspond to $q=0.1$ and the upper ones to $q=0.8$.

tions arising after this reduction describes q-deformation of the Painlevé transcendents and their higher order analogs. For $M=1$ one has a q-harmonic oscillator model, for $M=2$ a system with the $su_q(1,1)$ symmetry algebra, etc.

Using the Wronskian representation (9), we calculated exactly the free energy per site f_I in the thermodynamic limit $Z_N \to e^{-\beta N f_I}$, $N \to \infty$, for a uniform magnetic field and arbitrary M. For $M=1$ one has

$$-\beta f_I(H)=\ln \frac{2(q^4;q^4)_\infty \cosh \beta H}{(q^2;q^2)_\infty^{1/2}}+\frac{1}{2\pi}\int_0^\pi d\nu \ln(|\rho(\nu)|^2-q \tanh^2 \beta H), \tag{13}$$

where $(a;q)_\infty=\Pi_{j=0}^\infty(1-aq^j)$ and

$$|\rho(\nu)|^2=\frac{(q^2e^{2i\nu};q^4)_\infty^2(q^2e^{-2i\nu};q^4)_\infty^2}{4\sin^2\nu(q^4e^{2i\nu};q^4)_\infty^2(q^4e^{-2i\nu};q^4)_\infty^2}=q\frac{\theta_4^2(\nu,q^2)}{\theta_1^2(\nu,q^2)}. \tag{14}$$

The Jacobi θ functions are defined in the standard way.[10] The density function $\rho(\nu)$ has integrable singularities near the points $\nu=0,\pi$. Note that it satisfies a curious identity such that the second term in (13) vanishes for $H=0$.

The dependence of the magnetization $m(H)=-\partial_H f_I(H)$ on H has the form

$$m(H)=\left(1-\frac{1}{\pi}\int_0^\pi \frac{\theta_1^2(\nu,q^2)d\nu}{\theta_4^2(\nu,q^2)\cosh^2\beta H-\theta_1^2(\nu,q^2)\sinh^2\beta H}\right)\tanh \beta H. \tag{15}$$

Substituting $\beta H=h/(q^{-1}-q)$ into this expression and plotting $m(h)$, we obtain the dotted curves in Fig. 1 $q=0.1$ (the lower curve) and $q=0.8$. We would like to note that it is not clear how to solve the Ising model under consideration with the help of the traditional Bethe ansatz and transfer matrix methods.[6]

As was mentioned, a drawback of the given construction is that the KdV-generated partition function has a fixed temperature for fixed α. In order to obtain the full thermodynamic description it is necessary to extend the formalism and replace A_{ij} (11) at least by nA_{ij}, where n is a positive integer. The KdV temperature is thus normalized to $\beta=n=1$ (for $n>1$ one has to renormalize the magnetic field $H_i \to nH_i$ in order to imitate the effect of lowering the temperature). This means that we need to look for an integrable

model with phase shifts given by powers of expression (5). Then one may hope to recover the partition function at arbitrary values of the temperature $\propto 1/n$ by an analytical continuation.

The phase shifts A_{ij} for a given Hirota polynomial $P(x_1,x_3,\dots)$ specifying a particular evolution equation can be represented in the form[5]

$$e^{A_{ij}}=-\frac{P(k_1-k_2,k_2^3-k_1^3,\dots,(-1)^{\ell}(k_1^{2\ell+1}-k_2^{2\ell+1}))}{P(k_1+k_2,-k_2^3-k_1^3,\dots,(-1)^{\ell}(k_1^{2\ell+1}+k_2^{2\ell+1}))}, \tag{16}$$

where ℓ is the number of variables in P. We have looked for equations admitting N-soliton solutions with the prescribed phase shifts, substituting homogeneous (with the weights of the variables taken into account) polynomials with undefined coefficients into (16). It turns out that the taken conditions are very restrictive. The only solution we were able to find is the hierarchy which starts from $P(x_1,x_3,x_5)=16x_1^6+20x_1^3x_3+9x_1x_5-5x_3^2$, corresponding to $n=2$. After an appropriate rescaling of variables this polynomial coincides with the one for the B-type KP (BKP) equation.[11]

Using the Pfaffian representation of the N-soliton solutions of the BKP equation,[11] we calculated exactly the partition function in the thermodynamic limit $N\to\infty$ for a uniform magnetic field and arbitrary M. For $M=1$ one has

$$-\beta f_I(H)=\frac{1}{2\pi}\int_0^{\pi}d\nu\,\ln 2\left|\frac{(q;q)_\infty^2}{(-q;q)_\infty^2}\cosh 4\beta H+\frac{\partial_\nu\theta_1(\nu,q^{1/2})}{\theta_2(\nu,q^{1/2})}\right|, \tag{17}$$

where ∂_ν means the derivative with respect to the variable ν and $\theta_2(\nu,q^{1/2})$ is another Jacobi θ function.[10] The dependence of the magnetization on H is

$$m(H)=\left(1-\frac{1}{\pi}\int_0^{\pi}d\nu\left(1+\frac{(q;q)_\infty^2\theta_2(\nu,q^{1/2})\cosh 4\beta H}{(-q;q)_\infty^2\partial_\nu\theta_1(\nu,q^{1/2})}\right)^{-1}\right)\tanh 4\beta H. \tag{18}$$

For $q\to 0$ one gets the simple answer $m(H)=\tanh 2\beta H$.

Substituting $\beta H=h/(q^{-1}-q)$ into (18) and plotting $m(h)$, we obtain the solid curves in Fig. 1 for $q=0.1$ (the lower curve) and $q=0.8$. From a comparison of the magnetization curves one can see that as the temperature is lowered, which corresponds both to the transition from $n=1$ to $n=2$ and to an increase of q, the function $m(h)$ becomes steeper. This may be interpreted as a trend towards formation of a staircase-like fractal function that should take place at zero temperature according to the arguments of Ref. 12. Formation of the plateaus for $m(h)$ at low temperatures can be easily checked analytically for the nearest-neighbor interaction Ising antiferromagnet.

Attempts to find integrable systems with $n>2$ have failed for Hirota polynomials of up to 20th degree. Probably one has to pass from the scalar Lax pairs to the matrix ones in order to imitate other values of the discrete temperature. The lattice of temperatures itself resembles a discrete variable unifying different hierarchies of integrable systems into one class.

A relation between the two-dimensional nearest neighbor interaction Ising model and the sinh-Gordon hierarchy was discussed in Ref. 13. In particular, the corresponding N-soliton solution τ function, $N\to\infty$, was shown to be the generating function of correlation functions. It should be noted that our identification of the one-dimensional Ising model partition function with τ-functions of some integrable equations is different from the constructions considered in Ref. 13 and earlier related works. However, it is expected that the self-similar potentials (or q-analogs of the Painlevé transcendents) are related to some correlation functions in the corresponding setting as well. A hint on this comes from the fact that the supersymmetric quantum mechanical representation of the factorization method is related to the Lax pair of the sinh-Gordon equation.

The authors are indebted to Yu. Berest, V. Inozemtsev, T. Shiota, and C. Tracy for stimulating discussions. This work is supported in part by NSERC (Canada), RFBR (Russia) Grant 97-01-01041 and by INTAS 96-700.

[a)]e-mail: loutseni@crm.umontreal.ca
[b)]e-mail: svp@thsun1.jinr.ru

---

[1] L. Infeld and T. E. Hull, Rev. Mod. Phys. **23**, 21 (1951).
[2] V. Spiridonov, in *Proceedings of the International Workshop on Harmonic Oscillators*, College Park, Maryland, USA, March 1992, NASA Conf. Publ. 3197, p. 93; Phys. Rev. A **52**, 1909 (1995); http//.lanl.gov/abs/quant-ph/9601030.
[3] S. Skorik and V. Spiridonov, Lett. Math. Phys. **28**, 59 (1993); Phys. Lett. A **190**, 90 (1994).
[4] M. J. Ablowitz and H. Segur, *Solitons and the Inverse Scattering Transform*, Philadelphia: SIAM, 1981.
[5] A. C. Newell, *Solitons in Mathematics and Physics*, Philadelphia: SIAM, 1985.
[6] R. J. Baxter, *Exactly Solved Models in Statistical Mechanics*, London: Academic Press, 1982.
[7] Ya. L. Geronimus, Izv. Acad. Nauk SSSR **4**, 215 (1940).
[8] M. M. Crum, Q. J. Math. **6**, 121 (1955).
[9] M. Kac, Phys. Fluids **2**, 8 (1959).
[10] I. S. Gradshteĭn and I. M. Ryzhik, *Tables of Integrals, Series and Products* [transl. of 4th Russian ed.], New York: Academic Press, 1965 [Russian original Moscow: Nauka, 1963].
[11] R. Hirota, J. Phys. Soc. Jpn. **58**, 2285 (1989).
[12] R. Bruinsma, P. Bak, and J. B. Torrance, Phys. Rev. B **27**, 456 (1983).
[13] O. Babelon and D. Bernard, Phys. Lett. B **288**, 113 (1992).

Published in English in the original Russian journal. Edited by Steve Torstveit.

Effects of high-*j* intruder states in the fine structure of superdeformed bands

I. M. Pavlichenkov
Kurchatov Institute Russian Science Center, 123182 Moscow, Russia

(Submitted 11 November 1997)
Pis'ma Zh. Éksp. Teor. Fiz. **66**, No. 12, 759–764 (25 December 1997)

All known cases of $\Delta I=4$ bifurcation in superdeformed bands are analyzed on the basis of the theory proposed by the author in a previous paper [I. M. Pavlichenkov, Phys. Rev. C **55**, 1275 (1997)]. It is shown that the high-j intruder single-particle states play a critical role in the phenomenon. The bands in which fine structure can be observed are predicted. © *1997 American Institute of Physics.*
[S0021-3640(97)00324-1]

PACS numbers: 21.10.−k, 21.60.Ev

1. An intriguing discovery in the physics of high-spin nuclear states was the observation of fine structure (or $\Delta I=4$ bifurcation) in a superdeformed (SD) rotational band of the ^{149}Gd nucleus.[1] This structure is observed experimentally as $\Delta I=2$ staggering of the energies of γ transitions in the band. Later, $\Delta I=2$ staggering was found in two other regions of SD nuclei, but the errors of all measurements were comparable to the magnitude of the effect. This defect has been eliminated in the latest experiments.[2,3] Especially interesting is the work in Ref. 3, where not only was the regular pattern of the staggering in ^{149}Gd confirmed, but two other SD bands with a similar structure were found in ^{148}Eu and ^{148}Gd nuclei. The extent, regularity, and similarity of the staggering in all three bands preclude the possibility of explaining the phenomenon by means of band crossing.[4] We note that the $\Delta I=2$ staggering in a band is noticeable only for spins greater than some critical value I_0. For Eu and Gd isotopes $I_0\sim 40$.

The fine structure of the bands is explained by the nonadiabatic nature of the rotation and is described by an effective Hamiltonian in the form a power series of projection operators that project the total angular momentum I_k of the system onto moving axes $k=1,2,3$. The symmetry of the system imposes certain restrictions on the terms of this series. For the C_4 axis the lowest-order nonaxial operator in the Hamiltonian is $I_+^4+I_-^4$ $(I_\pm=I_1\pm iI_2)$. In molecules of the type AB_4 it results in *cluster states* in rotational multiplets.[5] The splitting of the levels of a cluster is small, since it is determined by tunneling through classically inaccessible regions of phase space. Only the symmetric state A_1 of the group C_{4v} exists in a nucleus. The position of this state in a cluster depends on the quantum number I. This is how the $\Delta I=2$ staggering is explained in Refs. 6 and 7. The symmetry axis C_4 implies the existence of a Y_{44} deformation of the surface of a nucleus. However, calculations of the equilibrium shape of rotating SD nuclei have not confirmed this conjecture. For this reason, the explanation of the phenomenon on the basis of an analogy with molecular cluster states is acknowledged to be problematic.[8]

2. In Refs. 9–11, the present author proposed a different explanation of the fine structure of nuclear bands. According to this theory, the operator $I_+^4+I_-^4$ in the rotational Hamiltonian is due to the interaction of rotation with the single-particle motion of nucleons in a nucleus. The starting point is the Routhian

$$H'=H_0-\frac{1}{2}\sum_{\lambda=2,4}\chi_\lambda\sum_\mu\mathcal{Q}_{\lambda\mu}^*\mathcal{Q}_{\lambda\mu}-\omega_1 J_1-\omega_2 J_2, \tag{1}$$

where H_0 is a spherically symmetric single-particle Hamiltonian, χ_2 and χ_4 are quadrupole and hexadecapole interaction constants, and the last two terms, which depend on the angular velocities ω_k and angular momenta J_k, describe the rotation of a nucleus about an axis perpendicular to the symmetry axis 3. Such an orientation of the rotation axis makes it possible to obtain nonaxial terms in the rotational Hamiltonian and to study the limit of a purely collective rotation. In the Routhian (1) the pairing interaction is omitted; taking account of this interaction does not present any difficulties.

In the Hartree approximation the rotational energy of a nucleus depends on the nonaxial collective coordinates $\alpha_{\lambda\mu}=\mathrm{Tr}(q_{\lambda\mu}\rho)$, $\mu=\pm 2,\pm 4$, which are nonzero because the density matrix ρ is nonaxial as a result of the rotation. But rotation appreciably distorts the motion of nucleons only in states with a high single-particle angular momentum j. States with the highest value of j in each shell are distinguished by parity, and for them j is a good quantum number. Correspondingly, we write the nonaxial coordinate in the form

$$\alpha_{\lambda\mu}=Q_{\lambda\mu}+\widetilde{\alpha}_{\lambda\mu}, \tag{2}$$

where $Q_{\lambda\mu}$ is the multipole moment of the nucleons of intruder subshells. Completely filled subshells do not contribute to $Q_{\lambda\mu}$, since the operator $q_{\lambda\mu}$ has a zero trace. Therefore $Q_{\lambda\mu}$ equals the multipole moment of nucleons in partially filled intruder subshells and is a microscopic quantity, $Q_{\lambda\mu}\sim\alpha_{\lambda\mu}/A$. The macroscopic quantity $\widetilde{\alpha}_{\lambda\mu}$ equals the multipole moment of the nucleons in the remaining states. It can be represented in the form of a perturbation series

$$\widetilde{\alpha}_{\lambda\mu}\approx\mathrm{Tr}(q_{\lambda\mu}\rho^{(2)})+\mathrm{Tr}(q_{\lambda\mu}\rho^{(4)})+\ldots, \tag{3}$$

where $\rho^{(n)}$ is the nth order correction to the density matrix of the nucleus as a result of rotation. Equations (2) and (3) can be used to find the rotational energy of a nucleus in the form of a power series in the angular momentum projection operators.[11] This series is not an ordinary perturbation-theory series, because rotation in the states of the intruder subshells is taken into account by means of exact diagonalization.

To obtain the conditions for the existence of fine structure in a band it is sufficient to study the limit of purely collective rotation. The corresponding rotational Hamiltonian to fourth order will have the form

$$H_{\mathrm{eff}}=\mathcal{A}\mathbf{I}^2+\mathcal{B}\mathbf{I}^4+d(I_+^2+I_-^2)+c(I_+^4+I_-^4). \tag{4}$$

The axial terms of this Hamiltonian include the moment of inertia $\mathfrak{I}$ ($\mathcal{A}=1/2\mathfrak{I}$) and the next inertial parameter $\mathcal{B}$. Nonaxial terms with the parameters

$$d=-\frac{1}{4\mathfrak{I}^2}\sum_{\lambda=2,4}\chi_\lambda Q_{\lambda 2}\left[\alpha_{\lambda 2}^{(2)}+\frac{I(I+1)}{4\mathfrak{I}^2}\alpha_{\lambda 2}^{(4)}\right],\quad c=-\frac{\chi_4}{16\mathfrak{I}^4}Q_{44}\alpha_{44}^{(4)} \tag{5}$$

arise on account of the quadrupole and hexadecapole interactions of the partially filled intruder subshells with the rotational distortion of the self-consistent field of the nucleus. For this reason, the parameters (5) include the moments Q_{22}, Q_{42}, and Q_{44} and the angular-frequency independent quantities

$$\alpha_{\lambda\mu}^{(n)}=\omega_+^{-(n+\mu)/2}\omega_-^{-(n-\mu)/2}\mathrm{Tr}(q_{\lambda\mu}\rho^{(n)}), \tag{6}$$

where $\omega_\pm=\omega_1\pm i\omega_2$. The nonaxial terms start to play an appreciable role for spins $I\sim I_c=|d/4c|^{1/2}$. The Hamiltonian (4) is not invariant under the group C_{4v} nor, in consequence, under the substitution $c\to -c$. The latter transformation inverts the levels of rotational multiplets.

The solution of the Schrödinger equation with the Hamiltonian (4) in the quasiclassical approximation makes it possible to find the condition for the existence of fine structure in a band:[11]

$$c>0,\quad I_0<I<I_c,\quad I_0=\left[(2-\sqrt{2})\frac{|d|}{4c}\right]^{1/2}. \tag{7}$$

If $c<0$, the staggering shifts into the upper parts of the multiplets. The fine structure is explained, as in Refs. 6 and 7, by oscillations of the wave function in classically inaccessible regions. The distinction is that these regions are formed not by a Y_{44} deformation but rather by the interaction of the rotational and single-particle motions.

3. The macroscopic quantities (6) can be calculated for the anharmonic oscillator potential with frequencies ω_z along the symmetry axis of a nucleus and $\omega_\perp$ in a perpendicular plane. Such a potential makes it possible to obtain an expression for $\alpha_{\lambda\mu}^{(n)}$ in analytical form. For example, in the limit $\omega_\perp-\omega_z\gg\omega_\perp+\omega_z$ we have

$$\alpha_{44}^{(4)}=\sqrt{\frac{35}{32\pi}}\,\frac{9\hbar^2}{64M^2\omega_\perp^4\omega_z^2}\left(\frac{\omega_\perp+\omega_z}{\omega_\perp-\omega_z}\right)^4(3\Sigma_{zz}-12\Sigma_{\perp z}+3\Sigma_{\perp\perp}-\Sigma_{\Lambda\Lambda}), \tag{8}$$

where M is the nucleon mass and the quantities Σ_{ik} equal the sums of bilinear combinations of the oscillator quantum numbers $n_\perp$, n_z, and Λ over all completely filled states. It is easy to show that $\alpha_{44}^{(4)}<0$ for SD bands. Therefore the sign of the parameter c is determined by the sign of the moment Q_{44}.

The microscopic quantities $Q_{\lambda\mu}$ can be calculated for an intruder subshell as

$$Q_{\lambda\mu}(j)=\sum_{v,\alpha}\langle jv\alpha|q_{\lambda\mu}|jv\alpha\rangle n_{jv\alpha}, \tag{9}$$

where $v=1,2,\ldots,j+1/2$, $\alpha=\pm 1/2$ is the signature and $n_{jv\alpha}$ are the nucleon occupation numbers of the subshell. For SD nuclei with $A\sim 150$ the subshells $h_{11/2}$, $i_{13/2}$ for protons (π) and $i_{13/2}$, $j_{15/2}$ for neutrons (ν) are not completely filled. The figure shows the dependence of the moment $Q_{44}(15/2)$ on the number $\mathcal{N}$ of occupied states and the rotational frequency $\omega=(\omega_1^2+\omega_2^2)^{1/2}$. The functions $F_j(\mathcal{N})=Q_{44}/\langle nl|r^4|nl\rangle$ are approximately the same for all subshells indicated above, since in the limit of angular-

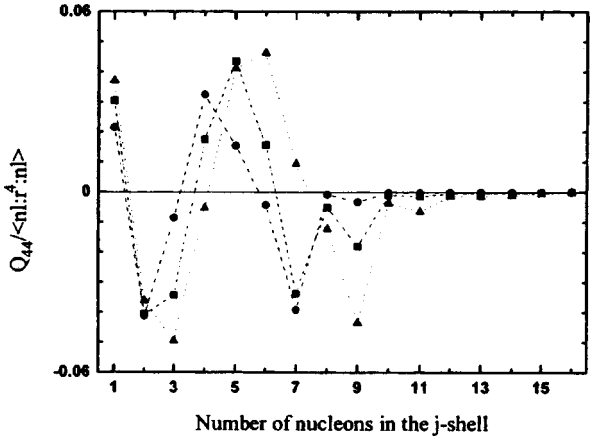

FIG. 1. Expectation value of the hexadecapole moment Q_{44} as a function of the number $\mathcal{N}$ of nucleons in the cranked single $j=15/2$ subshell for different rotational frequencies $\omega=0.4$ MeV (●), 0.6 MeV (□), 0.8 MeV (△) and the representative deformations $\beta_2=0.622$ and $\beta_4=0.041$.

momentum **j** alignment, which is close to the situation in our system at the rotational frequencies considered here, the average value of q_{44} is proportional to the Clebsch–Gordan coefficient $\langle jm,40|jm\rangle$, where m is the projection of **j** on the rotation axis 1. The matrix element $\langle jv\alpha|q_{44}|jv\alpha\rangle$ is always greater in symmetric (favored) states than in asymmetric (unfavored) states. The values of the parameters c and d for SD nuclei with $A\sim 150$ with (without) pairing give the following estimate of the critical spin: $I_0\sim 40(400)$.

4. We will use the condition $c>0$ for a comparison of the theory with experiment. For this, let us consider a more realistic model of the nucleus, with Z protons and N neutrons. Assuming that the mean square radius and the deformation are identical for neutrons and protons (this means that the ratio of the number of neutrons to the number of protons is constant inside the nucleus[12]), we obtain

$$c=-\frac{\chi_4}{16\mathfrak{I}^4}\left[\left(\frac{2Z}{A}\right)^{2/3}Q_{44}(\pi)+\left(\frac{2N}{A}\right)^{2/3}Q_{44}(\nu)\right]\left\{\left(\frac{2Z}{A}\right)^{2/3}\alpha_{44}^{(4)}(Z)+\left(\frac{2N}{A}\right)^{2/3}\alpha_{44}^{(4)}(N)\right\}, \tag{10}$$

where $Q_{44}(\tau)=\Sigma_j Q_{44}(\tau,j)$, $\tau=\pi,\nu$, and the summation over j extends over all incompletely filled intruder subshells. The high-j subshells make the predominant contribution. Nucleons in the levels of these subshells form the *dominant configuration* of the SD band. For nuclei with $A\sim 150$ this configuration is $\pi 6^m\nu 7^n$ with m protons and n neutrons in subshells with principal quantum numbers 6 and 7, respectively.

In the approximation of the configuration $\pi 6^m\nu 7^n$ the sign of the parameter c is determined by the sign of the quantity

$$\mathcal{F}(m,n)=15F_{13/2}(m)+19F_{15/2}(n), \tag{11}$$

TABLE I. Value of $\mathcal{F}(m,n)$ for the dominant configurations of some SD yrast bands with different rotational frequencies ω.

SD	Dominant	Deformation		$\mathcal{F}(m,n)$		
band	configuration	β_2	β_4	$\omega=0.4$ MeV	$\omega=0.6$ MeV	$\omega=0.4$ MeV
^{142}Eu(1)	$\pi 6^1 \nu 6^3$	0.49	0.04	0.327	0.071	−0.098
^{148}Gd(1)	$\pi 6^2 \nu 7^1$	0.55	0.035	−0.109	0.004	0.145
^{149}Gd(1)	$\pi 6^2 \nu 7^1$	0.60	0.032	−0.116	−0.018	0.113
^{150}Tb(1)	$\pi 6^3 \nu 7^1$	0.59	0.09	0.655	0.537	0.392
^{152}Dy(1)	$\pi 6^4 \nu 7^2$	0.61	0.022	−0.419	−0.257	−0.329
^{153}Dy(1)	$\pi 6^4 \nu 7^3$	0.59	0.12	0.259	0.074	−0.163
^{154}Dy(1)	$\pi 6^4 \nu 7^2$	0.57	0.03	−0.411	−0.263	−0.346

if the contributions of the neutrons and protons on the right-hand side do not compensate each other. For example, in the ^{151}Tb(1) band with the configuration $\pi 6^3 \nu 7^2$ the contributions of the neutrons and protons to $\mathcal{F}(3,2)$ are negative. There is no $\Delta I=2$ staggering, in agreement with experiment.[1] The absence of staggering in the ^{152}Dy(1) band[1] can also be explained by means of Eq. (11). In this case the dominant configuration of the band is $\pi 6^4 \nu 7^2$. Here the contributions of the neutrons and protons are of different sign, but there is no compensation (see Table I).

The dominant configuration $\pi 6^2 \nu 7^1$ is assigned to the series of SD bands in ^{148,149}Gd and ^{148}Eu nuclei. As one can see from Table I, the contributions of the neutrons and protons to the quantity $\mathcal{F}(2,1)$ compensate each other, and the simple criterion in applicable. Nonetheless, the results of Ref. 3 can be explained qualitatively by studying the configuration of the bands of ^{148}Gd[13] (we enumerate the SD bands of this nucleus according to Ref. 14) and ^{148}Eu relative to the configuration of the ^{149}Gd(1) band[15] and assuming, in accordance with experiment, that $c>0$ for the latter. Then the bands which are identical to it, ^{148}Eu(1) with the configuration $^{149}\mathrm{Gd}(1)\otimes(\pi[301]1/2,\alpha=-1/2)^{-1}$ and ^{148}Gd(4) with the configuration $^{149}\mathrm{Gd}(1)\otimes(\nu[411]1/2,\alpha=+1/2)^{-1}$, must have fine structure, since the moment $Q_{44}(\pi)(Q_{44}(\nu))$ changes very little when a proton (neutron) is removed from the $p_{1/2}(s_{1/2})$ subshell. On the contrary, when a neutron in a symmetric state is removed from the $g_{9/2}$ or $i_{13/2}$ subshell the moment $Q_{44}(\nu)$ decreases by a finite amount, which can change the sign of the parameter c. This explains the absence of fine structure in the bands ^{148}Gd(1) (the configuration $^{149}\mathrm{Gd}(1)\otimes(\nu[651]1/2,\alpha=+1/2)^{-1}$) and ^{148}Gd(5) ($^{149}\mathrm{Gd}(1)\otimes(\nu[642]5/2,\alpha=+1/2)^{-1}$. The absence of fine structure in the ^{148}Gd(6) band, which has the configuration $^{149}\mathrm{Gd}(1)\otimes(\nu[770]1/2,\alpha=-1/2)^{-1}$ at low rotational frequencies and the configuration $^{149}\mathrm{Gd}(1)\otimes(\nu[651]1/2)^{-2}\otimes(\nu[770]1/2,\alpha=1/2)$ at high rotational frequencies, follows from an approximation by the dominant configuration $\pi 6^2 \nu 7^0$ or $\pi 6^2 \nu 7^2$.

On this basis it follows that the most reliable predictions are those of the theory for SD nuclei having a dominant configuration for which the neutron and proton moments Q_{44} have the same sign. Let us give these configurations for the well-known yrast bands. The bifurcation can be observed in the bands $^{143}\mathrm{Eu}(\pi 6^1 \nu 6^4)$, $^{144}\mathrm{Eu}(\pi 6^1 \nu 7^1)$, $^{145}\mathrm{Tb}(\pi 6^1 \nu 6^4)$, and $^{151}\mathrm{Dy}(\pi 6^4 \nu 7^1)$ but it is absent in the bands $^{150}\mathrm{Gd}(\pi 6^2 \nu 7^2)$ and

^{152}Tb($\pi 6^3 \nu 7^3$). As one can see from Table I, the dominant-configuration approximation is applicable for the ^{150}Tb(1) and ^{152,154}Dy(1) bands and inapplicable for the ^{142}Eu(1) and ^{153}Dy(1) bands. An experimental check of these theoretical predictions would contribute to a deeper understanding of the phenomenon.

In summary, in this paper the reason for the $\Delta I = 2$ staggering of γ transitions of SD bands has been determined. It arises as a result of an interaction of the rotation with the partially filled intruder subshells. The nonadiabatic effects are described by a rotational Hamiltonian which is not invariant under the group C_{4v}; this limits the existence region of this staggering in respect to spin I and the nucleon occupation numbers of the single-particle states. This limitation has made it possible to check the theory for the example of eight SD bands in nuclei with $A \sim 150$. The situation in two other regions of SD nuclei is not so obvious, probably because the experimental data are unreliable.

I am grateful to G. de France for providing the experimental data for SD bands of the ^{148}Gd nucleus prior to publication. This work was performed with the support of the Russian Fund for Fundamental Research (Grant 96-02-16115).

[1] S. Flibotte, H. R. Andrews, G. C. Ball *et al.*, Phys. Rev. Lett. **71**, 4299 (1993).
[2] R. Krücken, G. Hackman, M. A. Deleplanque *et al.*, Phys. Rev. C **54**, R2109 (1996).
[3] D. S. Haslip, S. Flibotte, G de France *et al.*, Phys. Rev. Lett. **78**, 3447 (1997).
[4] W. Reviol, H.-Q. Jin, and L. L. Riedinger, Phys. Lett. B **371**, 19 (1996).
[5] W. G. Harter, Comput. Phys. Rep. **8**, 319 (1988).
[6] I. Hamamoto and B. Mottelson, Phys. Lett. B **333**, 294 (1994).
[7] A. O. Macchiavelli, P. Cederwall, R. N. Clark *et al.*, Phys. Rev. C **51**, R1 (1995).
[8] F. Dönau, S. Frauendorf, and J. Meng, Phys. Lett. B **387**, 667 (1996).
[9] I. M. Pavlichenkov and S. Flibotte, Phys. Rev. C **51**, R460 (1995).
[10] I. M. Pavlichenkov, JETP Lett. **64**, 252 (1996).
[11] I. M. Pavlichenkov, Phys. Rev. C **55**, 1275 (1997).
[12] M. Baranger and K. Kumar, Nucl. Phys. A **110**, 490 (1968).
[13] G. de France, D. Prévost, J. C. Lisle *et al.*, Phys. Lett., in press.
[14] G. de Angelis, R. Wyss, D. Bazzacco *et al.*, Phys. Rev. C **53**, 679 (1996).
[15] S. Flibotte, G. Hackman, I. Ragnarsson *et al.*, Nucl. Phys. A **584**, 373 (1995).

Translated by M. E. Alferieff

Solid deuterium source of ultracold neutrons based on a pulsed spallation source

A. P. Serebrov,[a] V. A. Mityukhlyaev, and A. A. Zakharov
B. P. Konstantinov St. Petersburg Institute of Nuclear Physics, Russian, Academy of Sciences, 188350 Gatchina, Russia

T. Bowles and G. Greene
Los Alamos National Laboratory, Los Alamos, New Mexico 87545 USA

J. Sromicki
Swiss Federal Institute of Technology, CH-8093 Zurich, Switzerland

(Submitted 28 October 1997)
Pis'ma Zh. Éksp. Teor. Fiz. **66**, No. 12, 765–770 (25 December 1997)

A new type of source of ultracold neutrons (UCNs) is proposed. The source operates on the basis of a pulsed spallation source. Solid deuterium makes it possible to obtain UCN density 10^4 neutrons/cm^3 as a result of high gain at low temperatures and the possibility of withstanding high pulsed heat loads as a result of the high specific heat of solid deuterium. © *1997 American Institute of Physics.*
[S0021-3640(97)00424-6]

PACS numbers: 29.25.Dz

INTRODUCTION

The possibility of obtaining UCN density 10^4 neutrons/cm^3 by using solid deuterium was discussed in Ref. 1 and studied experimentally in Refs. 2 and 3. In the present letter we are proposing a new type of UCN source based on a pulsed spallation source with a solid deuterium moderator.

In this method the high pulse neutron density of a spallation source is used and then the UCNs are confined in the large volume of a trap for a long period of time up to the next neutron pulse. The UCN density in such a source can exceed the pulsed neutron flux on average by a factor of 300, for example. The pulsed neutron flux density is limited by the specific heat of solid deuterium, and the average neutron density is limited by the thermal conductivity of solid deuterium.

SCHEME OF A UCN SOURCE BASED ON A PULSED ACCELERATOR

Let us examine the scheme of a UCN source show in Fig. 1. A 600 MeV proton beam with 1 mA per pulse strikes a lead (tungsten) target surrounded with water (5 cm), which cools the target and is used for preliminary thermalization of the neutron flux. Liquid-helium-cooled solid deuterium is the main neutron moderator and the source of UCNs. To decrease the heat load on the solid deuterium, a 3-cm thick bismuth shield can be placed in the light water of the spallation source. At the moment of the proton pulse the volume of the trap of the source is filled in a time of 2 s with UCNs up to a density

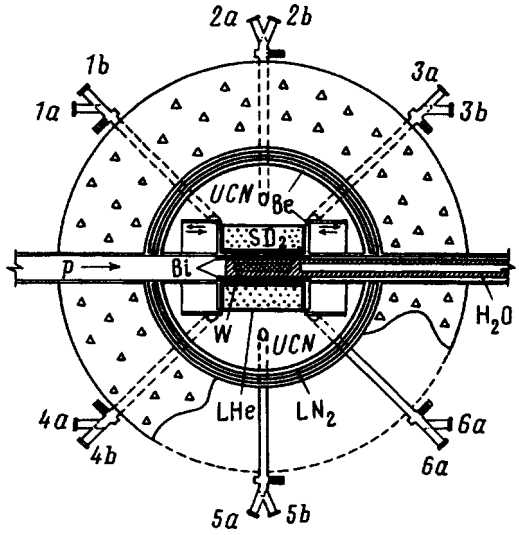

FIG. 1. Scheme of the UCN source.

almost equal to the UCN density in the source. Then, two cylindrical shields are closed up and cover the surface of the source. At this moment the proton current is switched off. The accumulated UCNs can be confined in the trap for a time close to the neutron lifetime. The trap walls are made of beryllium and they are at the temperature of liquid nitrogen. This gives UCN confinement in the trap for a time τ_{loss} determined only by the probability of losses at the walls of the trap, which is at a level of 10^4 s (Ref. 4), so that the storage time ($\tau_{st}^{-1}=\tau_n^{-1}+\tau_{\text{loss}}^{-1}$) is limited by the neutron lifetime (τ_n). During the interval between the neutron pulses (600 s) the UCN density in the trap decreases. Over this period of time the solid deuterium source cools to the temperature of liquid helium and is capable of accepting the next neutron pulse. Thus, the UCN density in the trap of the source is quasistationary with pulsed periodic pumping.

PARAMETERS OF THE UCN SOURCE

We shall present the basic parameters of the source that characterize a variant of a scheme which is not yet optimized. The average power or heat load on the source is 2 kW with an average current of 3.3 μA. The pulsed power is 0.6 MW with a current of 1 mA for 2 s. The interval between pulses is 600 s. The power released in the volume of the solid deuterium can be estimated using the data for a SINQ spallation source, in which 80–85% of the power is released in the main water-cooled target. Then it can be assumed that 15% of the total power will be released in the solid deuterium. We note that this estimate neglects the effect of the bismuth shield. Therefore the average load on the solid deuterium source equals 300 W. Correspondingly, the pulsed load is 300 times higher. The bismuth shield can decrease the heat release by approximately a factor of 3.

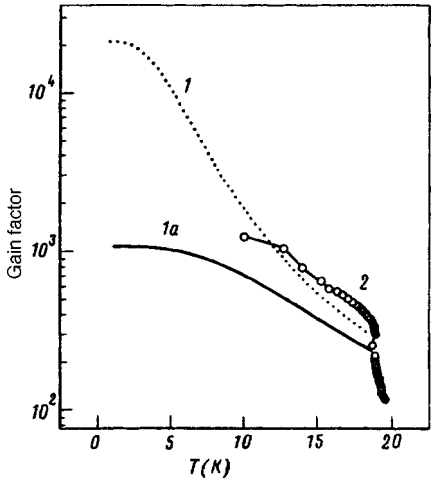

FIG. 2. Temperature gain of UCN yield for solid deuterium normalized to the UCN yield at room temperature: *1* — Computed curve for a large source with incoherent elastic scattering cross section of UCNs equal to zero or for a UCN source in the accumulation mode; *1a* — computed curve for a large source taking account of UCN scattering (2.2 b) and the hydrogen impurity (0.2%); *2* — experimental results obtained on a reactor with a source volume of 6 liters of solid deuterium containing 0.2% hydrogen. The large increase in the UC yield at 18.7 K is due to a transition from the liquid to the solid state.

TEMPERATURE GAIN FACTOR

Figure 2 displays the temperature variation of the gain for a solid deuterium source.[3] The curve *1* corresponds to a theoretical calculation for a half space filled with solid deuterium, i.e., for a source with a quite large volume ($V \geqslant 50$ liters). Curve *1a* represents a more accurate calculation in the same geometry but with allowance for the 0.2% hydrogen admixture and the incoherent elastic scattering of UCNs in the solid deuterium. An accelerator-based UCN source operates in an accumulation mode, while a reactor-based source operates in a flow-through mode. In the flow-through mode a jump in the UCN density is observed at the boundary of the solid deuterium as a result of incoherent elastic scattering of UCNs. For this reason, a high UCN density outside the source cannot be obtained with a reactor-based source (curve *1a* in Fig. 2). In the accumulation mode, the UCN density in the trap over the time of a pulse reaches the density inside the source (curve *1* in Fig. 2), and this density can be used in experiments. Curve *2* in Fig. 2 shows the results of a reactor experiment performed on a 6-liter solid deuterium source with 0.2% hydrogen added to the deuterium. For the experimental curve, at temperatures below 10 K the temperature dependence has still not been studied with adequate accuracy. Some experimental tests show that there is virtually no temperature dependence and the gain equals 1.2×10^3. In the calculations below we shall proceed from the experimental results, but we shall introduce a correction factor for the much higher degree of thermalization of the neutron flux in a large-volume source and a correction factor for deuterium purity.

The effective temperature of the neutron flux thermalized in a 6-liter volume was reconstructed from the experimental spectrum of neutrons emanating from the source.

The experimentally obtained spectrum is not Maxwellian but it can be decomposed into two spectra: 56% of the intensity with neutron temperature 180 K, and 44% of the intensity with neutron temperature 30 K.[2] However, the optimal neutron temperature equals 40 K.[1] The expected additional gain with respect to the experimental situation can be estimated as a factor of 2.1 when the temperature of the neutron spectrum reaches 40 K.

The dependence of the gain on the hydrogen impurity concentration in the deuterium was measured experimentally in Ref. 3, where mixtures of 0.2%, 0.7%, and 2% hydrogen in deuterium were used. Extrapolating the experimental data to a purity of 0.05–0.1% in terms of the H_2 impurity, one can expect an additional gain of 1.5. Then the combined correction factor for the experimental gain will equal to a factor of 3.1, and the expected gain for a large-volume source with a purity of 0.05–0.1% in terms of the hydrogen impurity will be 3.7×10^3.

SUBSTANTIATION OF THE SOURCE PARAMETERS

We shall present some estimates substantiating the parameters of the source. The neutron lifetime determines the maximum interval between pulses. Taking this interval to be 600 s and requiring that the exit time through one open neutron guide equal the neutron lifetime, we can calculate the characteristic volume of the UCN trap. In accordance with the gas-kinetic theory, the exit time of UCNs from a trap is given by $\tau=4V_t/S\bar{v}$, where V_t is the trap volume, S is the area of the exit window (cross section of the neutron guide), and $\bar{v}$ is the average velocity of UCNs in the trap. Assuming that the source volume is an order of magnitude smaller than the trap volume, we find that the radius of the trap must be 1.2 m.

We note that the limiting energy of reflection of UCNs from beryllium corresponds to a height of 2.5 m in terms of the gravitational energy of a neutron, so that a beryllium trap with a diameter greater than 2.5 m will not be completely filled. It is also important to understand that the maximum UCN density in a trap in a gravitational field is near the bottom of the trap, so that the neutron guides should be attached to the lower part of the trap.

A cold solid-deuterium moderator must have a sufficiently large volume to thermalize the neutron flux to a temperature of 40 K. This neutron temperature is optimal for obtaining maximum UCN yield.[1] The mass of solid deuterium must be sufficient to withstand the pulsed load by virtue of the specific heat. The surface area of the source must be large so that the trap will be rapidly filled with the UCN gas. As one can see, there are many factors requiring a substantial source volume. We shall attempt to choose the volume of the solid deuterium source on the basis of the requirement that the source temperature not exceed 10 K at the end of a pulse.

The heat release in the source is proportional to the filling time of the UCN trap. The trap filling time τ_f depends on the source surface area, i.e., the dimensions of the source. To simplify the estimates, we shall assume the source to be spherical with radius R_S. We choose the proton pulse duration to be $2\tau_f$. The heat release in the source ($Q=2\tau_f w_S$) determines the jump ΔT in the temperature of the solid deuterium at the time of the pulse according to the relation

$$Q = 2\tau_f w_S = C\ m\Delta T, \tag{1}$$

where w_s is the pulse power released in the solid deuterium, C is the specific heat of solid deuterium, and m is the mass of the solid deuterium.

For a preliminary estimate, we assume that 15% of the total power of the proton beam is released in the volume of the cold moderator and that, starting with volumes greater than 100–200 liters, this power depends very little on the volume of the moderator. Then from the relation (1), the gas-kinetic formula $\tau_f = 4V_T/S_S\bar{v}$, and the formula $V_T = (4\pi/3)(R_t^3 - R_S^3)$ we obtain

$$\Delta TC = \frac{2w_S}{\pi\bar{v}\rho}\,\frac{(R_t^3 - R_S^3)}{R_S^5}, \tag{2}$$

where R_t and V_t are, respectively, the radius and volume of the UCN trap, S_S is the surface area of the solid deuterium source, R_S is the source radius, and ρ is the density of solid deuterium.

Assuming $R_t^3 \gg R_S^3$, we obtain for the characteristic dimensions of the source

$$R_S = \left(\frac{2w_S}{\pi\bar{v}\rho}\,\frac{R_t^3}{\Delta TC}\right)^{1/5}. \tag{3}$$

As one can see from this analysis, the dependence of the source dimensions on the other parameters of the problem is very weak because of the exponent 1/5. Therefore it should be expected that even a rough analysis will give a quite definitive estimate. The product ΔTC in Eq. (3) must be interpreted as an integral of the specific heat between the initial and final temperature of the solid deuterium over the duration of the pulse. Taking the initial temperature to be 6 K and the final temperature to be 10 K, and using data for the specific heat, we obtain from Eq. (3) the value $R = 0.6$ m for the characteristic dimension of the source. The exponential filling time can be determined from the geometric parameters obtained for the source and is found to be 1.0 s. Hence the duration of the proton pulse for pumping a trap up to a UCN density equal to 86% of the maximum possible value will be 2.0 s.

We shall now estimate the average source temperature, using data on the thermal conductivity of solid deuterium. The thermal conductivity of solid deuterium depends strongly on the ortho- and para- composition of the deuterium and on the temperature. The ground state of deuterium at low temperature is orthodeuterium. However, the ortho- and para- compositions can depend on the level of the neutron and γ-ray radiation field. Experience in working with solid deuterium sources[2,3] has shown that at a level of irradiation by thermal neutrons of 8×10^{11} neutrons$\cdot$cm^{-2}s^{-1}, a fast neutron flux of 3×10^{10} neutrons$\cdot$cm^{-2}s^{-1}, and a heat release from γ rays of 1.5×10^{-2} W/g, 95% of the deuterium will be in the ortho- modification, and the irradiation of deuterium in the liquid phase accelerates the transition to orthodeuterium. The results of these experiments enable us to use the thermal conductivity of orthodeuterium in the calculations.

As a result of the sharp temperature dependence of the thermal conductivity and the substantial spatial variation of the heat release, an exact solution of this problem is nontrivial. We shall make here only a rough estimate using the following equation:

$$\overline{T_S} = T_{\mathrm{He}} + \frac{1}{2}\Delta T_{\max} = T_{\mathrm{He}} + \frac{\overline{W_S}\Delta R}{2\overline{\lambda} S_{\mathrm{He}}}, \tag{4}$$

where $\Delta T_{\max}$ is the maximum possible temperature difference, which arises when the heat release is entirely localized on the inner surface of the source near a warm target, ΔR is the radial thickness of the solid deuterium, S_{He} is the helium-cooled surface area, $\overline{\lambda}$ is the average thermal conductivity of solid deuterium, taken to be 8 W/K·m, and W_S is the average power of the heat load, equal to 300 W. Then we have for the average temperature of solid deuterium $\overline{T_s} = 7$ K.

UCN DENSITY IN THE SOURCE TRAP

Finally, we shall estimate the principal characteristic of a source — the UCN density in the trap. According to the estimate presented earlier, the gain for a solid deuterium source at temperature 7–10 K can be equal to 3×10^3. Then the coefficient relating the UCN density ($\rho_{\mathrm{UCN}}[\mathrm{cm}^{-3}]$) and the thermal-neutron flux ($\Phi_0[\mathrm{n/cm^2 s}]$) will have the form

$$\rho_{\mathrm{UCN}} = \frac{1}{2}\left(\frac{E_c}{T_R}\right)^2 \frac{G\Phi_0}{\overline{v}} = 2.4\times10^{-10}\cdot\Phi_0, \tag{5}$$

where E_c is the limiting energy of the trap, T_R is room temperature (300 K), and G is the temperature gain factor.

The average neutron flux for a solid deuterium moderator can be estimated using data on the distribution of the thermal-neutron flux in heavy water around a spallation source (SINQ design). The emergence depth of UCNs from solid deuterium at low temperatures is determined by the diffusion length $L_{\mathrm{D}} = \sqrt{L_S L_a/3}$, where $L_s = (n\sigma_S)^{-1}$ is the scattering length, n is the density of deuterium nuclei per cubic centimeter, $\sigma_S = 2.2$ b is the incoherent elastic scattering cross section, $L_a = (n\sigma_a)^{-1}$ is the UCN absorption length, and σ_a is the sum of the UCN trapping cross section (σ_c) and the UCN inelastic scattering cross section (σ_{up}). The computed value of the diffusion length is $\approx$15 cm at 6 K. Therefore the UCNs in the source trap are furnished by a 15-cm layer of solid deuterium. The average neutron flux in this layer can be estimated as 8×10^{13} neutrons·$\mathrm{cm}^{-2}\mathrm{s}^{-1}$ with a proton current of 1 mA. Then the UCN density in the source trap will be $\rho = 2.4\times10^4\Phi_0 = 2\times10^4$ neutrons/cm^3. Such a density will be 2 to 3 orders of magnitude higher than in present-day sources.[5,6]

CONCLUSIONS

In proposing a new type of UCN source based on a pulsed accelerator, we underscore that such a source is different from a reactor-based source. The advantage of a pulsed UCN source lies in the fact that a high UCN density is obtained at low temperatures of the solid deuterium as a result of the high pulse density of the neutron flux. The peak heat load at the moment of the pulse is taken up by the specific heat of deuterium and then removed by heat conduction on account of the quite high thermal conductivity of deuterium. The heat load on a stationary reactor-based source of UCNs is much higher than the average load on a pulsed UCN source.

It should be noted that the basic premises of the present design have already been checked experimentally.[2–4] This gives hope that the estimates presented here for the UCN density in a trap are quite realistic.

The design of the solid deuterium source of UCNs with high density in a trap can be implemented on accelerators in LANL (USA), PSI (Switzerland), Institute of Nuclear Research (Russia), KEK (Japan), and on a complex of the future European pulsed source.

The first experimental checks of the proposed design can be started on a small model, using heavy ice (D_2O) instead of solid deuterium.

We thank our colleagues at the St. Petersburg Institute of Nuclear Physics, Los Alamos National Laboratory, and PSI for helpful discussions.

[a)]e-mail: serebrov@lnpi.spb.su

---

[1] A. P. Serebrov, V. A. Mityukhlyaev, A. A. Zakharov *et al.*, JETP Lett. **59**, 757 (1994).
[2] A. P. Serebrov, V. A. Mityukhlyaev, A. A. Zakharov *et al.*, JETP Lett. **62**, 785 (1995).
[3] A. P. Serebrov, V. A. Mityukhlyaev, A. A. Zakharov *et al.*, Zh. Éksp. Teor. Fiz. [JETP], submitted for publication.
[4] V. P. Alfimenkov, V. E. Varlamov, A. V. Vasil'ev *et al.*, JETP Lett. **52**, 984 (1990).
[5] I. S. Altarev, N. V. Borovikova, A. P. Bulkin *et al.*, JETP Lett. **44**, 269 (1986).
[6] A. Steyrel, H. Nasel, F. K. Schreiber *et al.*, Phys. Lett. A **116**, 347 (1986).

Translated by M. E. Alferieff

Photoelectric instability in oxide glass

M. K. Balakirev,[a)] L. I. Vostrikova, and V. A. Smirnov
Institute of Semiconductor Physics, Siberian Branch of the Russian Academy of Sciences, 630090 Novosibirsk, Russia

(Submitted 28 October 1997)
Pis'ma Zh. Éksp. Teor. Fiz. **66**, No. 12, 771–776 (25 December 1997)

The spatially periodic modulation of optical anisotropy (MOA) induced in oxide glass by mutually coherent light beams with different frequencies (ω and 2ω) is unstable under illumination with monochromatic light with frequency ω. Disturbances with small amplitudes intensify and disturbances with large amplitudes relax. Irrespective of its initial degree, the MOA reaches the same steady-state level, which depends on the illumination intensity. Intensification of MOA is accompanied by the appearance of second-harmonic radiation whose intensity grows in time to a steady-state level. The instability of the anisotropy is due to degenerate three-wave mixing and to feedback arising as a result of the coherent photogalvanic effect. A hypothesis that takes into account the observed giant growth (by three orders of magnitude) of light absorption in the MOA region is proposed to explain the stabilization of the instability and the formation of stationary periodic refractive-index gratings. © *1997 American Institute of Physics.*
[S0021-3640(97)00524-0]

PACS numbers: 42.70.Ce, 42.65.Sf

It has been established in a number of recent works that the symmetry of an optically isotropic medium (glass) can be lowered by irradiation with monochromatic radiation. As a result, the state of the glass + light system is unstable. The change in symmetry is accompanied by a restructuring of the spectrum and spatial distribution of the light flux. This is manifested experimentally as the spontaneous appearance and amplification of the second harmonic under prolonged transmission of monochromatic light through an optical fiber[1,2] or as a self-maintained diffraction of light in bulk samples.[3] It is believed[4,5] that the coherent photogalvanic effect[6–9] (CPGE) — the appearance of a steady-state current in a medium illuminated by two mutually coherent sources with different frequencies (ω and 2ω) — is responsible for the instability. On the basis of this idea, the instability and growth of fluctuations of optical anisotropy in an isotropic medium under monochromatic illumination could be due to intensification of macroscopic fluctuations of the electrostatic field.

In the present letter we report the results of a direct observation of the instability of photoinduced modulation of the anisotropic refractive index in glass and investigate the properties of this instability.

The experiments were performed in oxide glass and consisted of the following. First, a reversible spatially periodic change Δn of the refractive index — a Δn grating[3,10] — was produced in glass by two mutually coherent beams at the fundamental and doubled

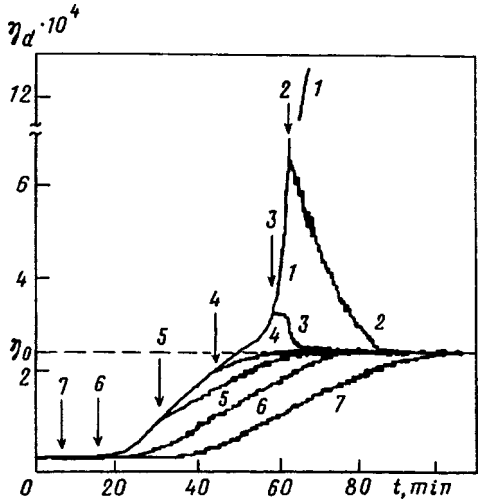

FIG. 1. Evolution of the diffraction efficiency of gratings with different initial amplitudes.

frequencies of a pulsed neodymium laser. The grating played the role of an initial disturbance at the next stage of the experiment. The amplitude of the initial disturbance was varied by varying the duration of illumination of the glass, and the angle between the beams was chosen so that the Δn grating would be oriented at the Brewster angle with respect to the beam at the fundamental frequency (main beam). After the initial disturbance was produced, the beam at the doubled frequency was covered and the dynamics of the diffraction efficiency of the main beam $\eta_d = I_d / I_1$ was investigated as a function of the amplitude of the initial disturbance and I_1 (I_d and I_1 are the peak powers of the diffracted and incident light). In this formulation, the main beam was the probe beam and simultaneously fulfilled the role of a ''pump.'' In another series of experiments, after the initial disturbance was written the dynamics of the second-harmonic radiation arising from the region of the grating under illumination by the main beam was investigated as a function of the intensity of the main beam and the amplitude of the initial disturbance.

1. A typical family of curves of the evolution of the diffraction efficiency for different initial disturbances is presented in Fig. 1. The arrows mark the moments when the writing of the gratings ceases and illumination of the gratings by radiation only at the fundamental frequency starts. Curve *1* characterizes the dependence of the diffraction efficiency of the initial disturbance on its writing time. One can see from the figure that disturbances with small amplitudes grow and disturbances with large amplitudes relax. However, irrespective of the initial value, the diffraction efficiency of the gratings reaches the same steady-state level $\eta_d = \eta_0$. Investigation of the dependence of η_0 on the illumination intensity showed that the steady-state level increases monotonically with I_1 and saturates at quite high values of I_1. On the whole, the observed dynamics of the gratings is formally similar to the evolution of disturbances in active nonlinear oscillatory systems with a stable limit cycle.

Thus there exists in the system a photoinstability of photoinduced refractive-index

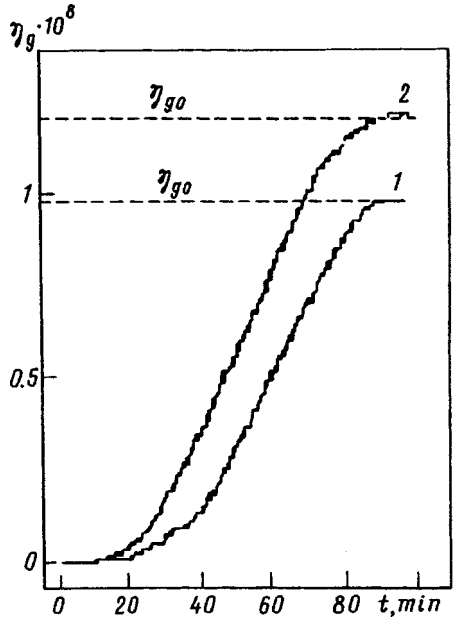

FIG. 2. Evolution of SHG efficiency with different illumination intensity: 1 — I_1, 2 — 1.4 I_1.

gratings whereby the system is brought to a stable steady state that depends on the intensity of the incident light.

2. Amplification of the gratings is accompanied by the appearance and growth of second-harmonic radiation from the region of the grating. The direction and polarization of this radiation are the same as in the case of the beam with the doubled frequency employed for producing the initial disturbance. The efficiency $\eta_g = I_2/I_1$ of second-harmonic generation (SHG) (I_2 is the peak power of the second harmonic produced) is observed to increase to a steady-state level η_{g0} (see Fig. 2, where the process is shown for two different intensities of the main beam). The level η_{g0} increases with I_1. Saturation of SHG and diffraction efficiencies is reached over the same period of time, i.e., a direct correlation is observed between $\eta_g(t)$ and $\eta_d(t)$.

If the diffraction efficiency of the initial disturbance is much greater than η_0, then the second-harmonic radiation at the initial stage of the relaxation of the grating is not detected to within the sensitivity of the apparatus. However, radiation does arise in the region $\eta_d \leqslant 1.2\eta_0$ and intensifies rapidly with decreasing amplitude of the grating, reaching a maximum at $\eta_d = \eta_0$. The SHG efficiency then equals the steady-state value η_{g0}. The correlation of the SHG efficiency with the relative diffraction efficiency is shown in Fig. 3. Thus, a direct relation is observed between the intensification of the gratings and the increment to the SHG efficiency.

We shall now discuss the results, proceeding from the fact that the change in the optical properties of glass is due to the appearance of an electric field **E(r)** in the glass as a result of the CPGE. The appearance of optical anisotropy in the simplest model is

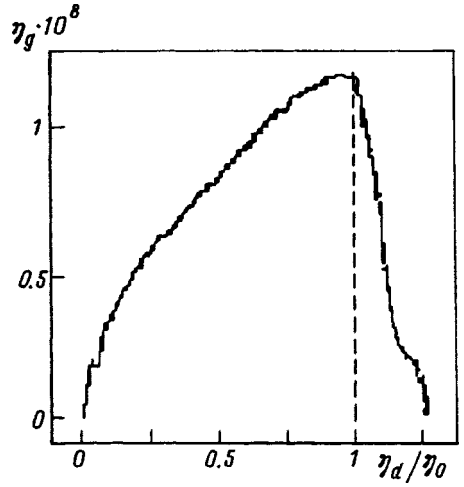

FIG. 3.

described as follows. The two-frequency light field $\mathbf{E}(\omega,2\omega)=\mathbf{E}(\omega)+\mathbf{E}(2\omega)$ with

$$\mathbf{E}(\omega)=\mathbf{e}_1E_1\exp\, i(\mathbf{k}_1\mathbf{r}-\omega t), \quad \mathbf{E}(2\omega)=\mathbf{e}_2E_2\exp\, i(\mathbf{k}_2\mathbf{r}-2\omega t) \tag{1}$$

produces in the glass a spatially periodic grating of the CPG current $\mathbf{J}(\mathbf{r})$:

$$\mathbf{J}(\mathbf{r})=(a_1\mathbf{e}_1(\mathbf{e}_1\mathbf{e}_2)+a_2\mathbf{e}_2)E_1^2E_2\exp\, i\mathbf{q}_E\mathbf{r}, \quad \mathbf{q}_E=(2\mathbf{k}_1-\mathbf{k}_2). \tag{2}$$

In Eqs. (1) and (2) $E_{1,2}$, $\mathbf{e}_{1,2}$, and $\mathbf{k}_{1,2}$ are the amplitudes, polarizations, and wave vectors of the harmonics and $a_{1,2}$ are the photogalvanic constants. Charge separation by the current $\mathbf{J}(\mathbf{r})$ results in the appearance and growth of an electrostatic field E:

$$\frac{dE}{dt}=\frac{4\pi}{\epsilon}(J-J_c), \tag{3}$$

where J_c is the conduction current and ϵ is the static permittivity. For small values of E, while the electrical conductivity σ does not depend on the field (but can depend on the intensity of the light), the conduction current is proportional to the field $J_c=\sigma(I_1,I_2)E$, and a periodic grating of the field with wave vector $\mathbf{q}_E$ accumulates in the sample: $E=(J/\sigma)(1-\exp(-t/\tau))$, $\tau=\epsilon/4\pi\sigma$. The field grating is accompanied by a grating of the effective second-order polarizability $\chi^{(2)}\sim\chi^{(3)}E$ with vector $\mathbf{q}_\chi=\mathbf{q}_E$ and a refractive-index grating $\Delta n\sim\chi^{(3)}E^2$ with vector $\mathbf{q}_n=2\mathbf{q}_E$, i.e., the glass transforms into an inhomogeneous optically uniaxial medium. In our experiment the gratings studied play the role of an initial disturbance and model fluctuations of the electrostatic field.

The appearance of an effective second-order polarizability in the disturbed medium produces conditions for the appearance of a CPG current under monochromatic illumination of the medium, since SHG becomes possible. As a result of this, small spatial fluctuations of the field can be intensified by monochromatic light and a mutual change in the optical properties of the medium and light flux should occur. The scenario of such an instability of system can be represented, using an idea of Ref. 4, as follows.

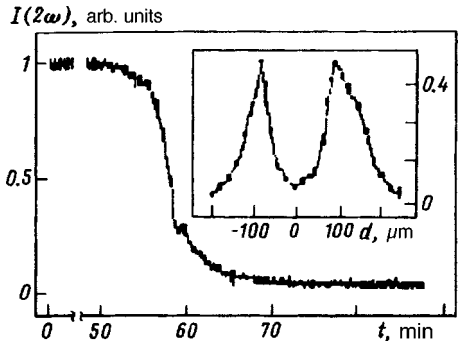

FIG. 4. Attenuation of the intensity of light at the doubled-frequency.

Let a weak fluctuation field $\mathbf{E}_f(\mathbf{r})$ exist in the medium. Monochromatic light $E(\omega)$ incident on the medium in the region where $E_f \neq 0$ generates a field $E_{2g}(2\omega, \mathbf{k}_{2g})$at the doubled frequency. The fields generated by this harmonic and by the incident light induce a CPG current $J_s \sim E_{2g}E_1^2$, which under certain conditions intensifies the initial charge separation, causing the field to increase in time. In other words, the CPGE engenders in the system a positive feedback which results in a light (more accurately, photoelectric) instability of the system. The Fourier components $E_f(\mathbf{q})\exp i(\mathbf{q}\cdot\mathbf{r})$ of the field which are spatially in phase with the current ($\mathbf{q}=2\mathbf{k}_1-\mathbf{k}_{2g}$) and are polarized so as to give maximum SHG efficiency should grow the most. For this reason, the development of instability should be accompanied by the formation of predominantly periodic anisotropic structures. In our experiment the conditions of maximum intensification were satisfied by choosing the polarization and angle of incidence of the light on the grating. In the process, a second harmonic with $\mathbf{q}_{2g}=2\mathbf{k}_1-\mathbf{g}_E$ is generated, and the spatial phase synchronism of this grating and of the initial grating of the field arises automatically.

It is important to underscore that the mechanisms studied should result in instability of anisotropy fluctuations not only of electrostatic origin. The only requirement is that they be accompanied by nonzero second-order polarizability. For this reason, the instability of optical anisotropy fluctuations studied above is quite universal and can be observed in a medium with any symmetry.

Comparing the experimental results with the model considered above shows that they qualitatively fit in the model, excluding the stabilization of the instability and the relaxation of the gratings.

Let us examine the possible mechanisms of stabilization, remaining within the phenomenological model (3). The CPG current J_s is determined by the relation (2), except that the external field $E(2\omega)$ in it is replaced by $E_{2g}(2\omega)$, which arises as a result of generation. Stabilization of instability appears with a change in sign of $J_s - J_c$. This is possible, if at some value of the field J_s increases with the field more slowly than J_c or decreases. Our experiments correspond to the latter case (see Sec. 2): As the amplitude of the grating increases (with $\eta_d/\eta_0 > 1$), the intensity of the generated harmonic decreases rapidly and, correspondingly, the current J_s should decrease.

The decrease in SHG efficiency is due to the rapid increase in the absorption of light

at this frequency as the amplitude of the grating increases above a steady-state level. Special experiments showed that as it passes through the grating, the doubled-frequency radiation can be attenuated on the beam axis by a factor of 30, irrespective of the polarization of the incident light. Figure 4 shows the time dependence of the intensity $I(2\omega)$ of the light with the doubled frequency after passing through the grating when the initial disturbance is written all the way to saturation. The typical intensity distribution over the diameter of the transmitted beam is shown in the inset. Since the transverse size of the grating is somewhat smaller than the beam diameter, the obtained distribution approximately reflects the dependence of the attenuation on the transverse distribution of the amplitude of the grating. If it is assumed, for a rough estimate, that the decay over the length of the grating is exponential, then the observed attenuation corresponds to absorption $\alpha \sim 7$ cm^{-1}. The change in absorption compared with an unperturbed medium is three orders of magnitude.

We note that an increase in light absorption has been observed[11] in optical fibers with prolonged passage of mutually coherent bichromatic light with frequencies ω and 2ω through them as well as with monochromatic illumination of germanium–aluminum silicate optical fibers doped with erbium.[12] At the present stage of the investigations, we do not completely understand the nature of the giant increase in absorption in the gratings, but it has been established experimentally that under our conditions it is not due to decay mechanisms (generation of subharmonics).

We also note that an increase in the current J_c, as a result of an increase in photoconductivity accompanying SHG, or an increase in conductivity with an increase of the field could make an additional contribution to stabilization of the instability. However, these mechanisms should not lead to a decrease of the SHG efficiency with increasing amplitude of the gratings. Therefore their contributions are not determining in our experiments, though they could be significant under other conditions (in other materials).

Of course, we do not claim that the scheme studied here gives an exhaustive description of the observed phenomena. It does not include diffusion and recombination of charge carriers, which damp the instability, and it neglects the nonlocal relation between the electrostatic field and E_{2g}. Such a relation should have an integral representation, describing the simultaneous growth of harmonics in space, and should be obtained in a self-consistent solution of the problem (see, for example, Refs. 4 and 5). However, we assume that these factors should not fundamentally change the interpretation of the experimental results.

We thank M. V. Énin for fruitful debates and a discussion of the results.

This work was supported by the Russian Fund for Fundamental Research (Grant 96-62-19353).

[a)]e-mail: balak@isp.nsc.ru

[1]U. Osterberg and W. Margulis, Opt. Lett. **11**, 516 (1986).
[2]B. Valk, E. M. Kim, and M. M. Salour, Appl. Phys. Lett. **51**, 722 (1987).
[3]M. K. Balakirev, L. I. Vostrikova, V. A. Smirnov, and M. V. Énin, JETP Lett. **63**, 176 (1996).
[4]M. I. Dyakonov and A. S. Furman, Comments Condens. Matter Phys. **16**, 19 (1992).

[5] E. M. Dianov, P. G. Kazanskiĭ, and D. Yu. Stepanov, Kvantovaya Élektron. (Moscow) **17**, 926 (1990) [Sov. J. Quantum Electron. **20**, 849 (1990)].
[6] N. B. Baranova and B. Ya. Zel'dovich, JETP Lett. **45**, 717 (1987).
[7] É. M. Baskin and M. V. Éntin, JETP Lett. **48**, 601 (1988).
[8] M. V. Éntin, Fiz. Tekh. Poluprovodn. **23**, 1066 (1989) [Sov. Phys. Semicond. **23**, 664 (1989)].
[9] V. B. Sulimov, Zh. Éksp. Teor. Fiz. **101**, 1749 (1992) [Sov. Phys. JETP **74**, 932 (1992)].
[10] M. K. Balakirev and V. A. Smirnov, JETP Lett. **61**, 544 (1995).
[11] M. C. Farries and M. E. Fermann, Electron. Lett. **24**, 294 (1989).
[12] J. Miguel Hickmann, E. A. Gouveia, A. S. Gouveia-Neto *et al.*, Opt. Lett. **19**, 1726 (1994).

Translated by M. E. Alferieff

Effects of two strong fields in resonant four-wave mixing

S. A. Babin, E. V. Podivilov, and D. A. Shapiro
Institute of Automation & Electrometry, Russian Academy of Sciences, 630090 Novosibirsk, Russia

(Submitted 8 September 1997; resubmitted 13 November 1997)
Pis'ma Zh. Éksp. Teor. Fiz. **66**, No. 12, 777–782 (25 December 1997)

An explicit solution is obtained for the four-wave mixing $\omega_4=\omega_1-\omega_2+\omega_3$ of two strong fields $\mathbf{E}_1,\mathbf{E}_3$ and two weak fields $\mathbf{E}_2,\mathbf{E}_4$ in a four-level system with large Doppler broadening. Resonance of the intensity dependence of the mixing coefficient is found around equal Rabi frequencies, $\mathbf{E}_1\cdot\mathbf{d}_1=\mathbf{E}_3\cdot\mathbf{d}_3$, where $\mathbf{d}_{1,3}$ are the dipole moments of the corresponding transitions. The effect is interpreted as a crossing of quasi-energy levels. Up to 6 peaks appear in the dependence of the conversion coefficient on the detuning of the probe field $\mathbf{E}_2$. The unexpected additional pair of peaks is a consequence of averaging over velocities. The results permit interpretation of the saturation behavior found in recent experiments on mixing in sodium vapor. © *1997 American Institute of Physics.* [S0021-3640(97)00624-5]

PACS numbers: 42.65.Hw

Four-level systems are promising objects for resonant optics and spectroscopy owing to the great variety of nonlinear effects. These include nonlinear interference, inversionless gain, resonance refraction, electromagnetically induced transparency, optically induced energy-level mixing and shifting, population redistribution, etc. (see Refs. 1 and 2 and citations therein). Recent experiments on continuous resonant four-wave frequency mixing of the Raman type with sodium molecules in a heat pipe[3,4] gave interesting behavior of the generated wave power as a function of the frequencies and intensities of the incident waves. In particular, the dependence of the output power on the intensity of the first strong field was found to saturate in an experiment on down-conversion,[3] while the dependence on the intensity of the third wave exhibited linear growth. The measurements were taken at large Doppler broadening, whereas the nonperturbational analytical theory was intended[5,6] for atoms at rest.

From the mathematical standpoint the development of a nonperturbative theory involves the solution of a set of 16 algebraic equations for the steady-state elements of the atomic density matrix for the four-level system. The problem is only to analyze the resulting awkward expression and to average this expression over a Maxwellian velocity distribution. In the present paper we study the particular case of two strong and two weak fields interacting with a four-level system having some symmetry. The fourth degree equation can be reduced to a biquadratic one, and then the integration can be done analytically (Fig. 1b).

Let us consider the conversion of two strong incident waves $\mathbf{E}_{1,3}$ resonantly interacting with opposite transitions gl,mn and the weak field $\mathbf{E}_2$ near the resonance with the

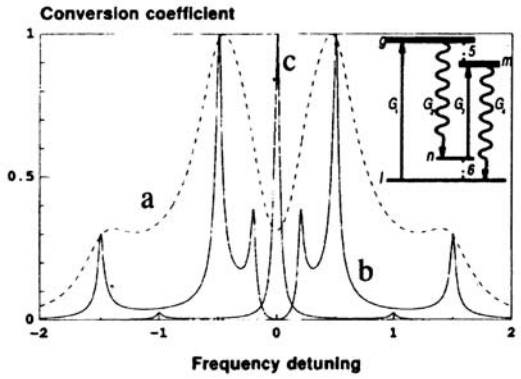

FIG. 1. Conversion coefficient $|\langle\beta_4\rangle|^2$ (arbitrary units) as a function of the detuning Ω of the second field at $|G_1|=1$, $|G_3|=0.5$, $k_1v_T=7.0$, $k_2v_T=6.9$, $\gamma=0.2$ (a), $\gamma=0.02$ (b), and $\gamma=0.02$ at $|G_1|=|G_3|=0.5$ (c) (all values are in ns^{-1}). The inset shows the level diagram of a four-level system interacting with two strong driving fields at opposite transitions (solid arrows) and with two weak fields (wavy arrows). The dotted lines show the forbidden transitions.

transition gn into the fourth output weak wave $\mathbf{E}_4$ (inset of Fig. 1). The electric field in the cell is

$$\mathbf{E}(\mathbf{r},t)=\sum_{\nu=1}^{4}\mathbf{E}_\nu\exp(i\omega_\nu t-i\mathbf{k}_\nu\cdot\mathbf{r}), \tag{1}$$

where $\mathbf{E}_\nu$ is the amplitude of the νth field, and $\omega_\nu,\mathbf{k}_\nu$ are the frequency and wave vector. The index ν numbers the transitions, $\nu=1,2,3,4$. The detunings $\Omega_1=\omega_1-\omega_{gl}$, $\Omega_2=\omega_2-\omega_{gn}$, $\Omega_3=\omega_3-\omega_{mn}$, $\Omega_4=\omega_4-\omega_{ml}$ are assumed to be small; $\omega_{ij}=(E_i-E_j)/\hbar$ are the transition frequencies between energy levels E_i and E_j. The indices $i,j=m,n,g,l$ denote the energy levels. The frequency and wave vector of fourth wave satisfy the phase-matching condition $\omega_4=\omega_1-\omega_2+\omega_3$, $\mathbf{k}_4=\mathbf{k}_1-\mathbf{k}_2+\mathbf{k}_3$.

The Maxwell equation for the output wave can be reduced to

$$\frac{d\mathbf{E}_4}{dx}=-\frac{2\pi i\omega_{ml}\mathbf{d}_{ml}}{c}\langle\rho_{ml}\rangle, \tag{2}$$

where x is the coordinate along $\mathbf{k}_4$, $\mathbf{d}_{ml}$ is the matrix element of the dipole moment operator $\hat{\mathbf{d}}$, c is the speed of light, ρ_{ml} is the coherence at the transition ml, and the angle brackets denote averaging over the velocity distribution. We are to calculate ρ_{ml} as a function of the input amplitudes $\mathbf{E}_{1,2,3}$, their wave vectors $\mathbf{k}_{1,2,3}$, and the frequency detunings $\Omega_{1,2,3}$.

With this goal we solve the equation for Wigner's atomic density matrix

$$\left(\frac{\partial}{\partial t}+\mathbf{v}\cdot\nabla+\gamma_{ij}\right)\rho_{ij}=q_j\delta_{ij}-i[\hat{V},\hat{\rho}]_{ij}, \tag{3}$$

where $\mathbf{v}$ is the atomic velocity, γ_{ij} are relaxation constants, $q_j = Q_j \exp(-\mathbf{v}^2/v_T^2)/v_T^3 \pi^{3/2}$ is the Maxwellian excitation function, and $\hat{V} = -\mathbf{E}(\mathbf{r},t)\cdot\hat{\mathbf{d}}/2\hbar$ is the interaction operator.

To the zeroth approximation we can neglect both the weak fields $\mathbf{E}_{2,4} \to 0$. The problem boils down to finding the populations $\rho_j \equiv \rho_{jj}$ and coherences $\rho_1 \equiv \rho_{gl}\exp(-i\Omega_1 t + i\mathbf{k}_1\cdot\mathbf{r})$, $\rho_3 \equiv \rho_{mn}\exp(-i\Omega_3 t + i\mathbf{k}_3\cdot\mathbf{r})$ of a pair of separated two-level systems. The solution for a two-level system in a strong field is well known (see Ref. 7).

Weak fields with amplitudes $G_2 = \mathbf{E}_2\cdot\mathbf{d}_{gn}/2\hbar$ and $G_4 = \mathbf{E}_4\cdot\mathbf{d}_{ml}/2\hbar$ give rise to cross-coherence between levels belonging to the opposite two-level systems at the allowed transitions, $\rho_2 \equiv \rho_{gn}\exp(-i\Omega_2 t + i\mathbf{k}_2\cdot\mathbf{r})$, $\rho_4 \equiv \rho_{ml}\exp(-i\Omega_4 t + i\mathbf{k}_4\cdot\mathbf{r})$, and at the forbidden transitions, $\rho_5 \equiv \rho_{gm}\exp(-i\Omega_5 t + i\mathbf{k}_5\cdot\mathbf{r})$, $\rho_6 \equiv \rho_{nl}\exp(-i\Omega_6 t + i\mathbf{k}_6\cdot\mathbf{r})$, where $\Omega_5 = \Omega_1 - \Omega_4$, $\Omega_6 = \Omega_1 - \Omega_2$, $\mathbf{k}_5 = \mathbf{k}_1 - \mathbf{k}_4$, $\mathbf{k}_6 = \mathbf{k}_1 - \mathbf{k}_2$. To first order one can neglect the influence of these fields on the populations ρ_j and coherences $\rho_{1,3}$. A set of 4 algebraic equations for the off-diagonal matrix elements appears:

$$
\begin{aligned}
&\Gamma_2\rho_2 - iG_1\rho_6^* + iG_3\rho_5 = -iG_2(\rho_g - \rho_n),\\
&\Gamma_4^*\rho_4^* + iG_3^*\rho_6^* - iG_1^*\rho_5 = iG_4^*(\rho_m - \rho_l),\\
&\Gamma_5\rho_5 - iG_1\rho_4^* + iG_3^*\rho_2 = iG_2\rho_3^* - iG_4^*\rho_1,\\
&\Gamma_6^*\rho_6^* + iG_3\rho_4^* - iG_1^*\rho_2 = -iG_2\rho_1^* + iG_4^*\rho_3.
\end{aligned}
\tag{4}
$$

Here $G_1 = \mathbf{E}_1\cdot\mathbf{d}_{gl}/2\hbar$ and $G_3 = \mathbf{E}_3\cdot\mathbf{d}_{mn}/2\hbar$ are the Rabi frequencies, $\Gamma_\nu = \gamma_\nu + i\Omega'_\nu$, $\gamma_1 \equiv \gamma_{gl}$, $\gamma_3 \equiv \gamma_{mn}$, $\gamma_2 \equiv \gamma_{gn}$, and $\gamma_4 \equiv \gamma_{ml}$ are the constants for relaxation of the coherence at the allowed transition, $\gamma_5 \equiv \gamma_{gm}$ and $\gamma_6 \equiv \gamma_{nl}$ are the constants for forbidden transitions, and $\Omega'_\nu = \Omega_\nu - \mathbf{k}_\nu\cdot\mathbf{v}$ is the Doppler-shifted detuning.

The solution of Eq. (4) for the off-diagonal element at transition ml can be written as

$$
\rho_4^* = -i\beta_4 G_1^* G_2 G_3^* - i\alpha_4 G_4^*. \tag{5}
$$

In the thin-medium approximation the generated field is small, $|G_4| \ll |G_2|$, so that one may neglect the absorption α_4 and find the coefficient β_4. We found the intensity of the output wave by integrating Eq. (2) from $x = 0$ to the cell length L:

$$
I_4(L) = \left|\frac{2\pi^2\omega_{ml}L}{c^2\hbar^3}\langle\beta_4\rangle(\mathbf{d}_{gl}\cdot\mathbf{e}_1)(\mathbf{d}_{gn}\cdot\mathbf{e}_2)(\mathbf{d}_{mn}\cdot\mathbf{e}_3)(\mathbf{d}_{ml}\cdot\mathbf{e}_4)\right|^2 I_1 I_2 I_3, \tag{6}
$$

where $\mathbf{e}_\nu$ is the polarization of the νth wave, and $I_\nu = c|E_\nu|^2/8\pi$ is its intensity. We find the coefficient β_4 by comparing Eq. (4) to a solution of the form (5):

$$
\begin{aligned}
\beta_4 = \frac{1}{D}\Bigg(&(\Gamma_5 + \Gamma_6^*)(\rho_g - \rho_n) - \frac{|G_1|^2 - |G_3|^2 - \Gamma_2\Gamma_5}{iG_1^*}\rho_1^*\\
&- \frac{|G_3|^2 - |G_1|^2 - \Gamma_2\Gamma_6^*}{iG_3^*}\rho_3^*\Bigg).
\end{aligned}
\tag{7}
$$

Here the elements $\rho_g, \rho_n, \rho_1, \rho_3$ are solutions for separated two-level systems. The determinant D of set (4) is a polynomial of fourth degree in the velocity. The averaging of the coefficient β_4 over velocity can be done by using the residue theorem in the Doppler limit $k_\nu v_T \gg |G_\nu|, |\Omega_\nu|, \gamma$.

To examine the intensity dependence of the coefficient β_4, let us consider the case of equal relaxation constants ($\gamma_{ij} = \gamma$), excitation of the lower level only, detunings of the strong field such that $\Omega_1/k_1 = \Omega_3/k_3 \ll v_T$, and equal wave numbers of the two weak fields. The condition $k_2 = k_4$ (and therefore $k_5 = k_6$) seems realistic for the down-conversion experiment of Ref. 3, where the difference of the wave numbers of the weak fields was about 10%. One can ignore the difference $k_2 - k_4$ provided that $|k_2 - k_4| \ll (k_2 k_4 k_5 k_6)^{1/4}$. In view of the phase-matching condition it is reasonable that the weak field detunings depend on a single parameter Ω: $\Omega_2 = k_2 \Omega_1/k_1 + \Omega$, $\Omega_4 = k_4 \Omega_1/k_1 - \Omega$. If all the wave vectors are parallel, then the expression for $\langle \beta_4 \rangle$ assumes a simple form:

$$\langle \beta_4 \rangle = \frac{N}{\sqrt{\pi} v_T} e^{-\Omega_1^2/k_1^2 v_T^2} \int_{-\infty}^{\infty} \frac{C(y)}{D(y)} \frac{dy}{\Gamma_{s1}^2 + k_1^2 y^2}, \tag{8}$$

$$C(y) = 4|G_1|^2 iz + (\gamma - ik_1 y)[|G_1|^2 - |G_3|^2 - (\gamma - i(k_2 y - \Omega)(\gamma - i(k_5 y - \Omega))].$$

Here $y = \mathbf{k}_2 \cdot \mathbf{v}/k_2 - \Omega_1/k_1$, $z = \Omega - i\gamma$, $\Gamma_{s1}^2 = \gamma^2 + 4|G_1|^2$ is the saturated width, and $N = Q_l/\gamma$ is the unperturbed population. The determinant $D(y)$ turns out to be a function of y^2:

$$D(y) = \kappa^4 y^4 - 2\kappa^2 y^2 \Delta_1 + \Delta_2^2, \tag{9}$$

$$\Delta_2^2 = [z^2 - (|G_1| - |G_3|)^2][z^2 - (|G_1| + |G_3|)^2],$$

$$\Delta_1 = (\mu^2/2 - 1)z^2 - |G_1|^2 + |G_3|^2, \quad \mu = \frac{k_1}{\kappa} = \left[\frac{k_2}{k_1}\left(1 - \frac{k_2}{k_1}\right)\right]^{-1/2} > 2.$$

The limiting case $\mu \to \infty$ corresponds to a quasi-degenerate four-level system $k_{5,6} \to 0$. The opposite limit $\mu \to 2$ means $k_3 \to 0$. The detuning dependence of $|\Delta_2|$ takes its minimum values at

$$\Omega = \pm |G_1| \pm |G_3|. \tag{10}$$

This is a consequence of the level splitting by the strong driving field. Note that at $|G_1| = |G_3|$ the two minima merge together. The reason is the equal Rabi splitting for each level.

The simple form of the determinant (9) allows calculating the mixing coefficient (8) explicitly,

$$\langle \beta_4 \rangle = \frac{\sqrt{\pi}}{\kappa v_T} \frac{N e^{-\Omega_1^2/k_1^2 v_T^2}}{\Gamma_{s1}^2 + \Gamma_{s1} R\mu + \Delta_2 \mu^2} \left[\frac{\gamma + iz\mu^2}{R} + \frac{4iz|G_1|^2 + \gamma(\mu^2 z^2/2 - \Delta_1)}{\Delta_2}\left(\frac{1}{R} + \frac{\mu}{\Gamma_{s1}}\right)\right], \tag{11}$$

where $R = \sqrt{2(\Delta_2 - \Delta_1)}$, $\Re R > 0$. The branch of the double-valued function Δ_2 should be chosen according to the following rules:

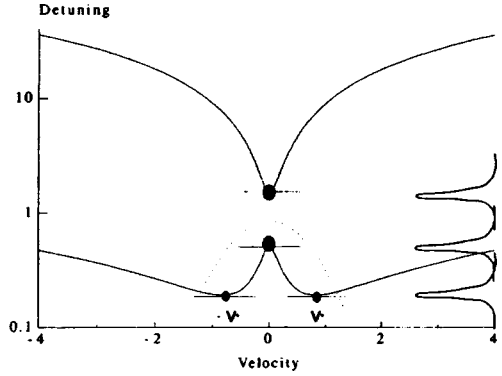

FIG. 2. Two positive solutions $\Omega^{(1,2)}(y)$ of the equation $D(y,\Omega)=0$ as a function of y/v_T. The other two zeros are symmetric: $\Omega^{(3)}=-\Omega^{(1)},\Omega^{(4)}=-\Omega^{(2)}$. The Maxwellian distribution is shown by the dotted curve.

$\Re\Delta_2<0$ at $P_+<|\Omega|$, $\Re\Delta_2\geqslant 0$ at $|\Omega|\leqslant P_-$, sign$(\Im\Delta_2)=$sign Ω at $P_-<|\Omega|\leqslant P_+$, where $P_\pm=||G_1|\pm|G_3||$.

The mixing coefficient $|\langle\beta_4\rangle|^2$ calculated from Eq. (11) is plotted in Fig. 1a as a function of the detuning Ω. The coefficient has 4 peaks at points given by (10) as for motionless particles. At equal distances between quasi-energy levels $|G_1|=|G_3|$ the two central peaks coalesce at the center $\Omega=0$ (Fig. 1c). Besides the zeros of Δ_2, zeros of $R(\Omega)$ may add two peaks near the center (Fig. 1b) arising from averaging over velocities. To interpret the two *additional* peaks let us plot the two positive zeros $\Omega^{(1,2)}(y)$ of D as a function of velocity y (Fig. 2). The two negative zeros are located symmetrically about the y axis. The *return points*,[a] where the derivative $\Omega^{(1,2)\prime}(y)$ equals zero, are places of minimum variation of the eigenfrequencies. They therefore give the main contribution to the integral over velocity. The integration over each neighborhood adds one sharp peak in the spectrum, as shown schematically at the right. The two upper return points denoted by the large black circles are located at zero velocity. Two additional return points, shown by the small black circles, appear at finite velocity and correspond to the additional peak. The return points can be found analytically from the conditions

$$\frac{dz}{dy}=0, \quad D(y,z)=0, \quad \frac{\partial D}{\partial y}+\frac{\partial D}{\partial z}\frac{dz}{dy}=0. \tag{12}$$

At $\gamma=0$ this gives four solutions (10) at $y=0$, namely, $z=\pm|G_1|\pm|G_3|$. At real $y=\pm\sqrt{\Delta_1}/\kappa$ there are two additional solutions:

$$z=\pm 2\sqrt{\frac{|G_1|^2}{\mu^2}-\frac{|G_3|^2}{\mu^2-4}}. \tag{13}$$

The coefficient Δ_1 becomes positive at $|G_1/G_3|\geqslant\mu^2/(\mu^2-4)=k_1^2/k_3^2$; otherwise the return point vanishes, and with it the additional peak.

The value $|\langle\beta_4\rangle|^2$ at exact resonance ($\Omega_\nu=0$, $\nu=1,\ldots,4$) is shown in Fig. 3 as a function of $|G_1|^2$. The sharp peak at $|G_1|=|G_3|$ confirms the qualitative interpretation of the effect as a crossing of quasi-energy levels. The inset in Fig. 3 illustrates the case

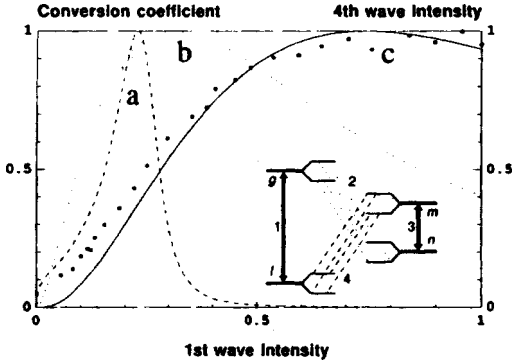

FIG. 3. Conversion coefficient $|\langle\beta_4\rangle|^2$ (in arbitrary units) versus $|G_1|^2$ at $|G_3|=0.5$, $\Omega=0$, $k_1v_T=7$, $k_2v_T=6.5$: $\gamma=0.06$ (a), $\gamma=0.6$ (b); intensity I_4 (arb. units) versus $|G_1|^2$ at $\gamma=0.6$ (c). The parameters for (b) and (c) correspond to experiment; all values are in ns^{-1}. The boxes denote the experimental points from Ref. 3. The inset illustrates the Rabi splitting of dressed states.

where the cross-transition from the upper sublevel of level g to the upper sublevel of level n has the same frequency as the transition between their lower sublevels. Concurrently, the same resonance is achieved for the transition m–l. In this case only 3 peaks remain in the spectrum (Fig. 1c), with a predominant maximum at the center. The crossing condition $|G_1|=|G_3|$ brings about the maximum conversion efficiency in the intensity dependence.

The splitting effect is evident from experimental results[3,4] on resonant four-wave mixing in Na_2. The main feature is saturation of the output power as a function of one of the strong fields. The experimental conditions of Ref. 3 generally satisfy the above model: (1) a down-conversion level scheme $\omega_4<\omega_1$ (see inset, Fig. 1) with $k_1v_T=7.0$ ns^{-1}, $k_2v_T=6.5$ ns^{-1}, $k_3v_T=5.2$ ns^{-1}, $k_4v_T=5.7$ ns^{-1}; (2) the interaction region is short enough (about 1 cm) that the model of thin media can be employed; (3) the estimated level parameters are $N_l\sim10^{12}\,\text{cm}^{-3}\gg N_n\sim10^{11}\,\text{cm}^{-3}\gg N_g, N_m$; $\gamma_m\simeq\gamma_g\sim0.2\,\text{ns}^{-1}$, $\gamma_n\simeq\gamma_l\sim0.02\,\text{ns}^{-1}$. A slightly noncollinear geometry (mixing angle $\theta\sim10^{-2}$) leads to an effective broadening $\Delta\omega\sim kv_T\cdot\theta\sim0.1\,\text{ns}^{-1}$. Another factor is the usual jitter of laser frequencies, especially for dimer and dye lasers, $\Delta\omega\sim0.2$–$0.4\,\text{ns}^{-1}$. Thus, the effective value $\gamma=0.3$–$0.6\,\text{ns}^{-1}$ seems reasonable; (4) the maximum field values estimated from the focusing geometry, $|G_1|^{\max}\sim1\,\text{ns}^{-1}$, $|G_2|^{\max}\sim0.2\,\text{ns}^{-1}$, and $|G_3|^{\max}\sim0.5\,\text{ns}^{-1}$, nearly correspond to the condition of two strong fields.

The resonance condition $|G_1|=|G_3|$ may result in peaks in both $\beta_4(I_1)$ and $\beta_4(I_3)$. If $|G_1|^{\max}>|G_3|^{\max}$, the peak is seen only in $\beta_4(I_1)$. The width of the peak is determined by the decay rate γ. Since in the experiment $\gamma\sim|G_3|^{\max}$, the peak is wide (Fig. 3b) and gives a smooth saturation curve $I_4(I_1)$ (Fig. 3c), in agreement with the experimental data (boxes in Fig. 3). At the same time, there is no saturation for $I_4(I_3)$ in both theory and experiment. Under the opposite experimental condition, $|G_1|^{\max}<|G_3|^{\max}$ (Ref. 4), the behavior of $I_4(I_1)$ and $I_4(I_3)$ changes.

Thus the model explains qualitatively the main features of the measured saturation curves. To observe the sharp resonances arising from Rabi splitting, stabilization of laser

frequencies seems to be important. To increase the efficiency of conversion into the fourth wave it is necessary to tune the laser frequencies to the corresponding peaks. The optimum at $\Omega_\nu = 0$ corresponds to equal Rabi frequencies $|G_1| = |G_3|$.

The authors are grateful to S. G. Rautian, A. M. Shalagin, and M. G. Stepanov for fruitful discussions and to B. Wellegehausen and A. A. Apolonsky for clarifying the details of their experiments. This work was partially supported by the RFBR, Grants 96-02-00069G and 96-15-96642, and Deutsche Forschungsgemeinschaft, Grant WE 872/18-1.

[a)]Or ''return frequencies,'' as they are called in the theory of three-level system with large Doppler width.[8]

[1] M. Scully, Phys. Rep. **219**, 191 (1992).
[2] O. Kocharovskaya, Phys. Rep. **219**, 175 (1992).
[3] S. Babin, U. Hinze, E. Tiemann, and B. Wellegehausen, Opt. Lett. **21**, 1186 (1996).
[4] A. Apolonsky *et al.*, Appl. Phys. B **64**, 435 (1997).
[5] A. K. Popov, Izv. Ross. Akad. Nauk, Ser. Fiz. **60**, 99 (1996).
[6] D. Coppeta, P. Kelley, P. Harshman, and T. Gustavson, Phys. Rev. A **53**, 925 (1996).
[7] S. G. Rautian, G. I. Smirnov, A. M. Shalagin, *Nonlinear Resonances in Atomic and Molecular Spectra* [in Russian] (Nauka, Novosibirsk, 1979).
[8] O. G. Bykova, V. V. Lebedeva, N. G. Bykova, and A. V. Petukhov, Opt. Spektrosk. **53**, 171 (1982) [Opt. Spectrosc. **53**, 101 (1982)].

Published in English in the original Russian journal. Edited by Steve Torstveit.

Precompression of matter during radiative energy transfer in a steady-state thermonuclear burn wave

S. Yu. Gus'kov and L. P. Feoktistov
P. N. Lebedev Physics Institute, Russian Academy of Sciences, 117924 Moscow, Russia

(Submitted 28 October 1997)
Pis'ma Zh. Éksp. Teor. Fiz. **66**, No. 12, 783–786 (25 December 1997)

It is shown that precompression of matter ahead of the thermonuclear burn wave front can occur in the central volume of a multilayer cylindrical system under conditions of radiative energy transfer outside the region of wave propagation. The degree of compression is sufficient for the development of a self-maintained wave of fusion reactions. [S0021-3640(97)00724-X]

PACS numbers: 28.52.Cx, 44.40.+a

1. From the standpoint of initial energy costs one of the most economical versions of a steady-state fusion reaction with unlimited intensification in terms of energy is a thermonuclear burn wave in a cylindrical system under conditions such that a portion of the energy released is converted into thermal radiation and this radiation is used for precompression of thermonuclear fuel ahead of the wave front.[1] The following such system is being studied: two infinitely long coaxial cylindrical shells of matter consisting of heavy elements, the inner shell containing the thermonuclear material and the gap between the shells being filled with matter consisting of light elements. The conversion of the released thermonuclear energy into thermal radiation occurs in the inner shell and radiative transfer occurs along the gap between the cylinders.

In the present letter, a theoretical groundwork is laid for the possibility of initiation and the conditions of propagation are determined for an ''external'' (with respect to the burn region) wave of radiative energy transfer which provides the precompression of thermonuclear matter that is required for the development of a stationary burn wave.

2. Without going into the specific method of initial ignition (this can be irradiation with a laser pulse or ion beam), we take as the conditions of propagation of a self-maintained wave of DT reactions the well-known conditions of development of a detonation wave[2] or a thermonuclear burn wave,[3] which require that the parameter ρr (product of the density of the matter by the radius of its cylindrical volume) and temperature exceed the values

$$\rho_c r_c = 0.3 - 0.4 \text{g/cm}^2, \quad T_c = 10 \text{ keV}. \tag{1}$$

Moreover, we shall assume that the propagation of the wave is characterized by a definite degree η of fuel burnup. Further, we shall assume, as is ordinarily done for pulsed inertial systems, that neutrons do not deposit energy in the system, whereas α particles are completely stopped in the burn region and the inner shell.

Thus the problem is formulated as follows. The system contains a source of energy with thermonuclear energy release intensity in terms of α particles that corresponds to the above-indicated ignition parameters (1). We are interested in the rate of heat transfer through the gap between the cylinders and the ratio of this rate and the velocity of a ''conventional'' burn wave that would propagate along an isolated cylindrical volume of DT matter with the prescribed parameters (1). Is it possible for the rate of heat transfer through the gap to exceed the velocity of a ''conventional'' burn wave under the additional requirement that the pressure in the gap will be sufficient for compression of DT matter so that the ignition condition (1) is satisfied?

In the approximation of a uniform temperature distribution over the cross section, the following equation of energy balance, established in the system after the burn wave front passes, holds:

$$T\sum_{j=1}^{3} A_j m_j + SW_r = \epsilon_a \eta \frac{\beta}{(1+\beta)} m_1, \tag{2}$$

where T is the temperature of the matter; A_j and m_j are, respectively, the specific heats and masses (per unit length) of parts of the cylindrical system (the indices 1, 2, and 3 refer to the DT material, the inner shell, and the gap between the shells, respectively); $m_1=\pi r_1^2\rho_1$, $m_2=\pi(r_2^2-r_1^2)\rho_2$, and $m_3=\pi(r_3^2-r_2^2)\rho_3$; r_1, r_2, and r_3 are, respectively, the radii of the inner and outer surfaces of the inner shell and the inner surface of the outer shell; β is the ratio of the thermal energy of the matter to the kinetic energy and can be estimated from the self-similar solution for isothermal expansion of matter[4] for a cylindrical geometry $\beta=1/3(\gamma-1)$, γ is the adiabatic exponent (ratio of specific heats); $W_r=4\sigma T^4/c$ is the energy density of the equilibrium radiation, $\sigma=1.03\times10^{24}$ ergs/cm$^2\cdot$s$\cdot$keV^4 is the Stefan–Boltzmann constant; c is the speed of light; $S=\pi r_3^2$; and, $\epsilon_\alpha=6.8\times10^{17}$ ergs/g is the calorific value of the DT matter in terms of α particles.

We shall now determine the region of characteristic parameters of the system, proceeding from the ignition conditions (1). The density and temperature of the DT material compressed by the inner shell under pressure in the gap are, neglecting the energy losses in the shell,

$$\rho_c \approx \rho_1\left(\frac{\gamma+1}{\gamma-1}\right)\left(\frac{m_2}{m_1}\right)^{1/(\gamma-1)}, \quad T_c \approx T\frac{A_3 m_3}{A_1 m_1}\frac{\beta}{(1+\beta)}. \tag{3}$$

The compression time of the inner cylinder $t_c \cong r_2/v_c$ (v_c is the average velocity of the shell material toward the center) is

$$t \approx r_2\left[\frac{(1+\beta)\rho_2}{(\gamma-1)(R^2-1)W_3}\left(1+\frac{m_3}{m_2}\right)\frac{\Delta}{r_2}\right]^{1/2}; \tag{4}$$

$\Delta=r_2-r_1$ is the thickness of the inner shell, $R=r_3/r_2$, $W_3=A_3T\rho_3$ is the internal energy of the matter in the gap between the shells. This approximation is valid for not very high ratios $m_2/m_1 \leqslant 10-20$. Assuming that the degree of burnup is 20% and, for definiteness, $m_2/m_1=10$, $\rho_1=0.2$ g/cm^3 (density of DT ice), $\rho_2=20$ g/cm^3, and $\rho_3=2$ g/cm^3, we obtain that according to Eq. (3) the parameter $\rho_c r_c=0.4$ g/cm^2 corresponds to masses $m_1\approx2\times10^{-2}$ g/cm and $m_2\approx2\times10^{-1}$ g/cm with the aspect ratio of the inner

shell $r_2/\Delta \approx 20$ and $r_2 \approx 0.18$ cm. As a result of the energy balance equation (2), the second ignition condition $T_c = 10$ keV is satisfied with $T = 2$ keV and $m_3/m_1 \approx 12.5$, which corresponds to $R \approx 1.5$. For higher values of the parameter R a higher ignition temperature is reached with a lower temperature in the gap: $T_c \approx 14$ keV and $T \approx 1.4$ keV for $R \approx 2$ and $T_c \approx 16$ keV and $T \approx 1$ keV for $R \approx 2.5$.

3. We now proceed directly to the problem of heat transfer along the gap between the shells. The transfer equation is

$$A_3 m_3 \frac{\partial T}{\partial t} = \frac{\partial}{\partial x}\left(\chi \frac{\partial W_r}{\partial x}\right) - \alpha W_r \frac{c}{4} \frac{2\pi(r_3 + r_2)}{\pi(r_3^2 - r_2^2)}, \tag{5}$$

where $\chi \equiv L_g c/3 = 2(r_3 - r_2)c/3$ is the thermal conductivity, which in the case of radiative transfer in the gap between the shells is determined by a geometric factor, since the geometric radiative transfer length L_g under these conditions is much smaller (by more than an order of magnitude) than the material transfer length; $\alpha(T,\rho) \equiv q_s/q_r$ is the ''albedo'' of the shell — the ratio of the energy flux transferred by the radiational thermal conductivity in the shell and converted into internal energy q_s of the vaporized material to the equilibrium radiation flux q_r.

Setting in Eq. (5) $\chi \sim V_\chi t$, we obtain the following simple estimate for the rate of heat transfer along the gap between the shells:

$$V_\chi = \left[\frac{2}{3}\frac{r_2}{t} c(R-1)\right]^{1/2} \left(\frac{W_r}{W_{s1} + W_{s2} + W_3}\right)^{1/2}, \tag{6}$$

where $W_{s1} + W_{s2} = (ct/2r_2(R-1))\,\alpha W_r$ is the specific internal energy of the vaporized parts of the shells. We note that the heat-transfer rate V_χ increases as the shell albedo decreases.

Let us examine in greater detail the process of vaporization of the shells and let us estimate the ''albedo.'' Radiative transfer in the shell material consisting of heavy elements is determined by the material path length, which can be represented as a power-law function of the temperature and density of the material $L_r = aT^n/\rho^m$. For definiteness, we hall assume that the shells are made of the same material. The radiation flux into each shell can be approximately determined as

$$q_s = \chi \frac{\partial W_r}{\partial x} \approx \left(\frac{4}{4+n}\right) \frac{L_r c}{3} \frac{W_r}{h}, \tag{7}$$

where h is the thickness of the layer of vaporized matter

$$h \approx q_s t / W_s, \tag{8}$$

$W_s = A_s T \rho_s$ is the internal energy of the vaporized shell material. Combining Eqs. (7) and (8), it is easy to obtain an expression for the albedo and the rate of increase of the thickness of the layer of vaporized shell material:

$$\alpha \approx \left[\frac{4}{3}\left(\frac{4}{4+n}\right)\frac{L_r}{ct}\frac{W_s}{W_r}\right]^{1/2}, \quad v_h \approx \frac{h}{t} = \left[\frac{1}{3}\left(\frac{4}{4+n}\right)\frac{W_r}{W_s}\right]^{1/2}. \tag{9}$$

The necessary condition for rapid radiative transfer is that the gap must not be filled with the vaporized heavy-element shell matter. This condition is satisfied if the rate of increase of the thickness of the layer of vaporized matter is less than the rate at which this material is removed into the volume of the shell by the shock wave:

$$v_h \leqslant v_s = \left[2\left(\frac{\gamma-1}{\gamma+1}\right)\left(\frac{W_s}{\rho_{s0}}\right)\right]^{1/2},$$

where ρ_{s0} is the initial density of the shell material ($\rho_{s0}=\rho_2$). The expression for v_h in Eq. (9) reduces this condition to

$$\frac{1}{3}\left(\frac{4}{4+n}\right)\frac{L_r}{ct} \leqslant \left(\frac{\gamma-1}{\gamma+1}\right)\frac{2W_s^2}{\rho_{s0}c^2 W_r}. \tag{10}$$

When the condition (10) is satisfied, a region of vaporized matter is formed at the boundaries of the shells. The pressure in this region equals the pressure of the matter in the gap $W_s = W_3$ (''Sakharization'' process). A wave of radiative heat conduction propagates into the shell along this vaporized matter.

Comparing Eqs. (9) and (10) shows that the minimum value of the albedo, which, as shown above, corresponds to the maximum rate of heat transfer along the gap, is reached when $v_h = v_s$ (equality in the condition (10)):

$$\alpha_{\min} = 2\left(\frac{\gamma-1}{\gamma+1}\frac{2W_3^3}{\rho_{s0}c^2 W_r^2}\right)^{1/2}. \tag{11}$$

The rate of heat transfer along the gap between the shells should exceed the velocity of the burn wave front at least during the compression of the inner shell by the pressure generated when heat wave heats up the material in the gap. Substituting expressions (11) and (4) into Eq. (6) we find that the maximum rate of heat transfer along the gap (with minimum albedo) over the compression time of the inner shell is

$$V_\chi = c\left(\frac{\gamma-1}{\gamma+1}\frac{2W_r^2}{\rho_{s0}c^2 W_3}\right)^{1/4}\left[\frac{\xi^2}{3(\xi+2)}\right]^{1/2}, \quad \xi = \left[\frac{2(\gamma+1)(R-1)^2(R^2-1)}{(1+\beta)(1+m_3/m_2)}\frac{r_2}{\Delta}\right]^{1/2}. \tag{12}$$

Finally, substituting expression (4) into Eq. (10), using the ''Sakharization'' condition $W_s = W_3$, and taking the constant and exponents in the expression for radiation path length, respectively, $a = 10^{-3}$, $n=3$, and $m=1$, we find that the condition that the radiative transfer channel not be filled during the compression of the internal cylinder requires

$$T \leqslant 1.12\left[\left(\frac{\gamma-1}{\gamma+1}\right)\frac{\rho_3^5 r_2^2 (R-1)^2}{\chi^2}\right]^{1/11}.$$

For the system parameters which were determined in Sec. 2 the condition that the gap between the shells not be filled leads to the requirement $T \leqslant 1.2$ keV. According to Eqs. (12), the rate of heat transfer along the gap is $V_\chi \approx 10^{-2}c = 3\times 10^8$ cm/s, which is approximately three times higher than the velocity of a ''conventional'' thermonuclear burn wave for the ignition conditions (1).

In summary, our theoretical analysis substantiates the possibility of a wave of radiative energy transfer propagating in a multilayer cylindrical system, permitting the propagation of a thermonuclear burn wave with precompression of the cold thermonuclear matter at the wave front.

This work was supported by Russian Fund for Fundamental Research Grant 97-02-16727.

[1] L. P. Feoktistov, Usp. Fiz. Nauk, in press.
[2] E. N. Avrorin, L. P. Feoktistov, and L. I. Shibarov, Fiz. Plazmy **6**, 965 (1980) [Sov. J. Plasma Phys. **6**, 527 (1980)].
[3] S. Yu. Gus'kov, O. N. Krokhin, and V. B. Rozanov, Nucl. Fusion **16**, 957 (1976).
[4] V. S. Imshennik, Dokl. Akad. Nauk SSSR **131**, 1287 (1959) [Sov. Phys. Dokl. **5**, 253 (1960)].

Translated by M. E. Alferieff

Observation of the plasma channel dynamics and Coulomb explosion in the interaction of a high-intensity laser pulse with a He gas jet

G. S. Sarkisov,[a)], V. Yu. Bychenkov, and V. T. Tikhonchuk
P. N. Lebedev Physics Institute, Russian Academy of Sciences, 117924 Moscow, Russia

A. Maksimchuk, S. Y. Chen, R. Wagner, G. Mourou, and D. Umstadter
Center for Ultrafast Optical Science, University of Michigan, Ann Arbor, MI 48109-2099, USA

(Submitted 11 November 1997)
Pis'ma Zh. Éksp. Teor. Fiz. **66**, No. 12, 787–792 (25 December 1997)

We report the first interferometric observations of the dynamics of electron–ion cavitation of relativistically self-focused intense 4 TW, 400 fs laser pulse in a He gas jet. The electron density in a channel 1 mm long and 30 μm in diameter drops by a factor of approximately 10 from the maximum value of $\sim 8\times 10^{19}$ cm^{-3}. A high radial velocity of the plasma expansion, $\sim 3.8\times 10^{8}$ cm/s, corresponding to an ion energy of about 300 keV, is observed. The total energy of fast ions is estimated to be 6% of the laser pulse energy. The high-velocity radial plasma expulsion is explained by a charge separation due to the strong ponderomotive force. This experiment demonstrates a new possibility for direct transmission of a significant portion of the energy of a laser pulse to ions. © *1997 American Institute of Physics.*
[S0021-3640(97)00824-4]

PACS numbers: 52.50.Jm, 52.20.Hv, 42.65.Jx

A number of proposed applications of ultrahigh-intensity, short laser pulses implies laser guiding for distances much longer than the Rayleigh length. Guiding of intense laser pulses in underdense plasmas due to the relativistic self-focusing was first reported in Ref. 1 and then studied in detail in Refs. 2–6. However, the dynamics of plasma channel at high laser intensities and phenomena associated with its expansion have not yet been addressed. This letter presents new experimental results on the dynamics of the plasma channel produced by an ultrahigh-intensity, short laser pulse and offers a theoretical interpretation for these results.

The experiment was performed using the 10 TW Ti:sapphire–Nd:glass laser system based on chirped-pulse amplification,[7] developed at the Center for Ultrafast Optical Science, University of Michigan. The laser operates at the wavelength $\lambda = 1.053$ μm and produces 3-J, 400-fs FWHM pulses with an intensity contrast of 10^5. The laser beam, 50 mm in diameter, was focused with an off-axis parabolic mirror ($f/3.3$, $f = 16.5$ cm) to a 10 μm spot with a vacuum intensity 6×10^{18} W/cm^2. Laser beam was focused in a high-back-pressure (7 MPa) He gas jet expanding through a nozzle 1 mm in diameter.

The optimal conditions for beam guiding correspond to focusing of the laser on the jet edge, with a He atom density $n_{\mathrm{He}} \simeq 3 \times 10^{19}$ cm^{-3}. The jet thickness was about 1 mm. A two-channel optical setup has been used for simultaneous recording of interferometric and shadow plasma images. The probe beam was split from the main beam, propagated through an adjustable optical delay, and was incident on a plasma in the direction perpendicular to the interaction beam. The plasma was imaged using a single spherical lens with angular aperture $\pm 7°$ on two cooled 12-bit CCD cameras. The spatial and temporal resolution was 10 μm and 400 fs, respectively. For the electron density measurements the air-wedge shearing interferometer[8] was used.

The plasma evolution was investigated in the time interval from -2 to $+55$ ps. As $t=0$ we take the time of arrival of the maximum laser intensity in the focal plane $z=0$. The first signs of gas ionization were observed at $t=-2$ ps. This indicates the laser intensity is above the He ionization threshold, $\sim 10^{15}$ W/cm^2, at that time.[9] We observed a fast gas ionization in the cone of laser convergence, which is 8.6°. It propagates along the laser axis approximately at the speed of light until it reaches the rear side of the jet. On the time of ionization (from -2 to $+3$ ps) the front part of interferogram is blurred because of the fringe motion during the exposure time. The first signatures of plasma channel formation (fringe bending on the laser axis) were observed at $t=0$ ps. The channel length increases with subluminal velocity up to 1000 μm.

The interferometric and shadow plasma images taken at $t=20$ ps are shown in Fig. 1 for a laser energy of 1.7 J (4.3 TW). The local opposite displacement of the interference fringes in a narrow axial region in the interferogram indicates a decrease of the phase shift in this region and hence a decrease of the electron density. This region is manifested in the shadow image by a bright narrow line, which is due to refraction of the probe beam on the high radial electron density gradient. The two-dimensional reconstruction of the electron density profile for $t=35$ ps (assuming the axial symmetry of a plasma) for the same laser conditions is presented in Fig. 2a. The maximum electron density is 7.6×10^{19} cm^{-3} at a radius of $\simeq 20$ μm and the depth of the plasma channel is up to 80–90%. The accuracy of measurement of the channel depth is limited by the Abel inversion procedure.

The dynamics of electron density profile near the focal plane ($z=100$ μm) is shown in Fig. 2b. The electron density gradient at the channel walls reaches the value of 5×10^{22} cm^{-4} at a time of 7 ps and remains practically the same out to 55 ps. The evolution of the lineal electron density (number of electrons per unit length $N_e = 2\pi \int r dr n_e(r)$) at $z=100$ μm and the evolution of the mean electron density in the same cross section are presented in Fig. 3a. After the initial phase of fast ionization (from -2 to 0 ps) the number of electrons remains constant (from 0 to 9 ps), and then ionization starts again. At the same time the average electron density starts to decrease. These features are in agreement with the temporal behavior of the plasma radius at $z=100$ μm (shown in Fig. 3b). It remains approximately the same from 0 to 9 ps then the plasma begins to expand radially with almost constant velocity. If we define the plasma edge as a region where the electron density equals 5×10^{18} cm^{-3} (17% ionization), then the expansion velocity equals 3.8×10^8 cm/s (curve *1* in Fig. 3b). The region of higher degree of ionization, 1.5×10^{19} cm^{-3} (50% ionization), expands at a lower velocity $\sim 2.5 \times 10^8$ cm/s (curve *2* in Fig. 3b).

We attribute the plasma expansion to ionization of the ambient gas by fast ions

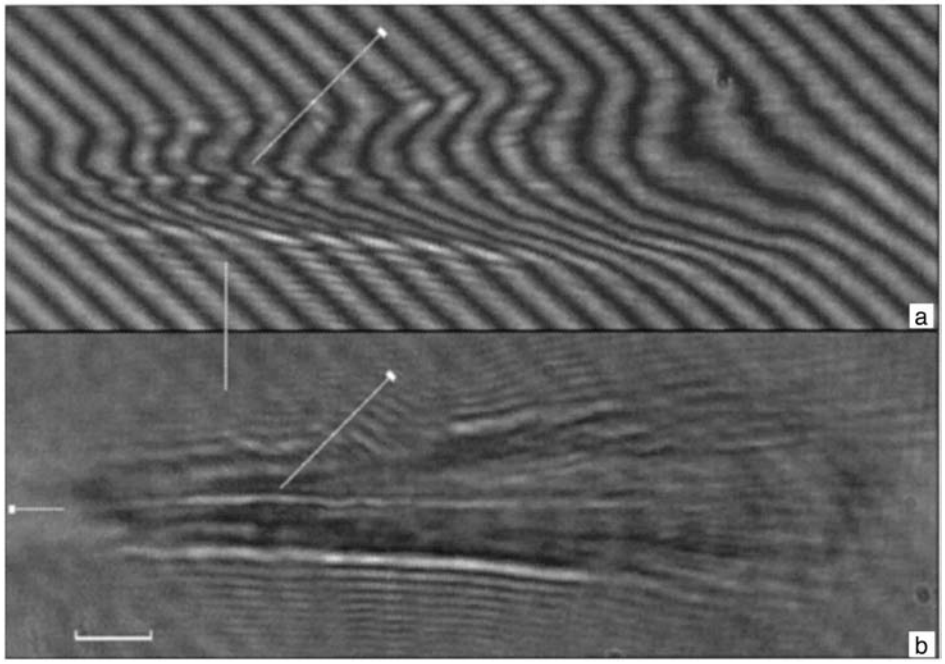

FIG. 1. Interferometric (a) and shadow (b) images of a plasma at time 20 ps after focusing 1.7 J, 4.3 TW laser pulse. The 100 μm spatial scale is shown in left corner. The vertical line in the shadow image marks the position of focal plane. Arrows indicate the plasma channel. The horizontal arrow indicates the direction of the interaction laser beam.

expelled from the channel. Then the expansion of plasma edge (with 17% ionization) can be related to the propagation of fast ions with an energy of about 300 keV, while the expansion of the main plasma volume (with 50% ionization) corresponds to 130 keV ions. This assumption of collisional ionization of the gas by fast ions also explains the ~ 10 ps delay time, which is the time needed for fast ions to penetrate through the laser-ionized plasma volume and reach the ambient gas. (The velocity of the plasma profile at a given density is lower than the actual ion velocity on account of the radial ion expansion and the decrease of the ion flux. However, we neglect this difference in present paper and, therefore, underestimate the ion energy.)

The channel diameter (Fig. 3b) also changes with time. Up to time $t=9$ ps we do not observe a significant variation of channel diameter $D\sim 10$–15 μm, which is at the limit of our spatial resolution. At $t>9$ ps the channel diameter increases to $25-35$ μm at a velocity of about 6×10^7 cm/s.

The initial laser beam channeling can be attributed to the effect of relativistic self-focusing of intense laser pulse.[1] The critical power for relativistic self-focusing $P_c=17n_c/n_e$ GW (where n_e is the electron density and n_c is the critical density) corresponds under our conditions to 280 GW, which is more than 10 times lower than the actual laser power. Therefore we speculate that a substantial part of the laser power is trapped in a narrow channel near the laser axis. The amount of trapped power depends on

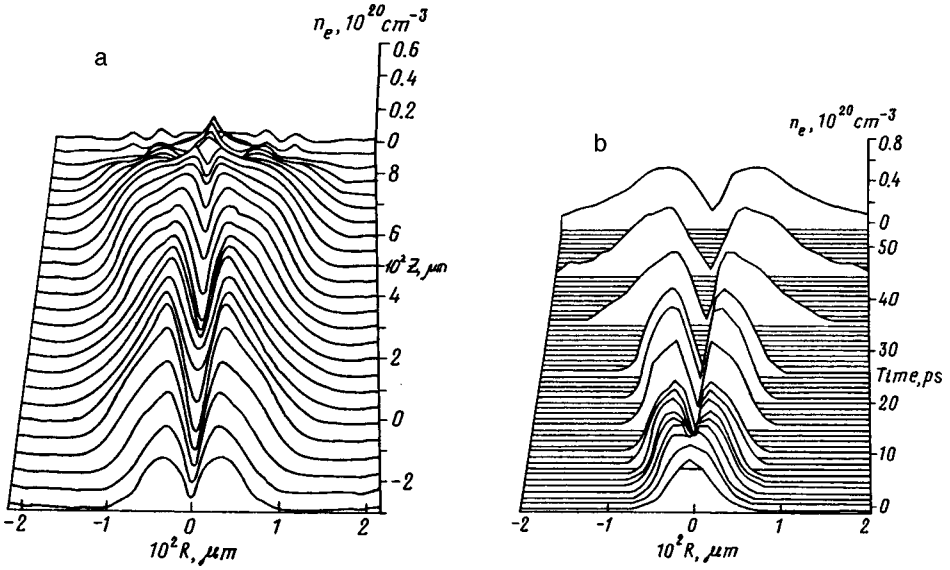

FIG. 2. Two-dimensional electron density distribution, $n_e(r,z)$, at time 30 ps (a), and the evolution of the radial electron density profile, $n_e(r,t)$, at the axial position $z=100$ μm from the focus (b).

the focusing conditions and it is about 50% in the present case. This estimate is deduced from the measurement of the radial energy distribution in the output plane of the laser channel. The actual diameter of the laser channel is probably smaller than the instrumental resolution and was not measured directly in the experiment. (Below we estimate the

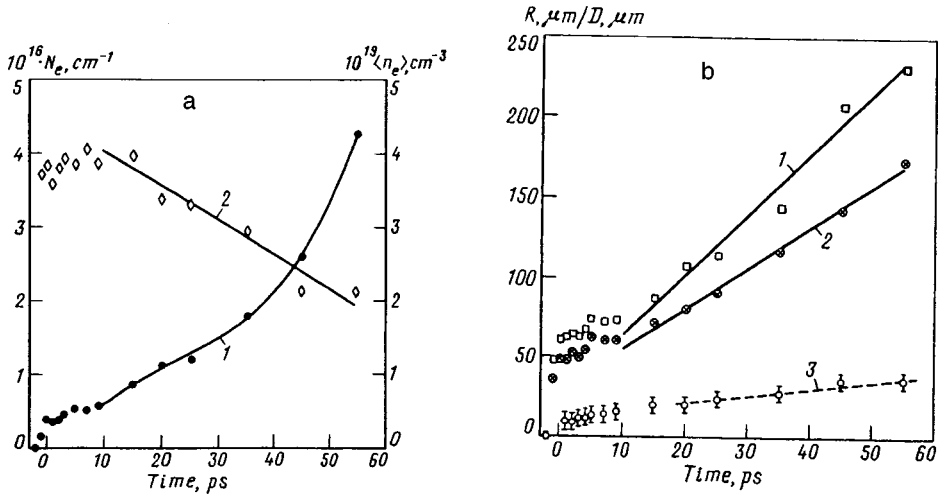

FIG. 3. a: Temporal evolution of the linear electron density, $N_e(t)$, (curve *1*) and the mean electron density (*2*) in the cross section located at $z=100$ μm from the focal plane. b: Temporal evolution of the plasma radius at $z=100$ μm for the $n_e=5\times10^{18}$ cm^{-3} (*1*) and 1.5×10^{19} cm^{-3} (*2*), and the temporal evolution of the plasma channel diameter (*3*).

channel radius as $r_0 \approx 3\mu$m by relating it to the fast ion energy.) The rest of laser power is not trapped and ionizes gas in the laser convergence cone. The measured initial fully ionized plasma radius in the focal plane is $r_p \simeq 40\ \mu$m.

The laser pulse exerts a radial ponderomotive force on electrons, expels them from the axis, and forms an electron channel. Its depth, $\delta n_e / n_e = \lambda_e^2 \nabla_r^2 \sqrt{1+a^2/2}$, is about 10% for a laser channel radius $r_0 \approx 3\mu$m and $a^2 \approx 5$. This formula follows from Poisson's equation and the balance between the electrostatic and ponderomotive potentials. Here $\lambda_e = c/\omega_p$ is the electron inertia length, ω_p is the electron plasma frequency, and $a = 0.85 \times 10^{-9} \lambda[\mu\text{m}] \sqrt{I[\text{W/cm}^2]}$ is the dimensionless laser field vector potential in a channel. The ions do not have time to move during the passage of the laser pulse and the electrons return to their original position when the pulse ends. However, the laser pulse supports the electron channel and because of that loses its energy for ion acceleration. Then the ions in the wakee of the laser pulse acquire a kinetic energy and begin to move in radial direction. This effect, known as ''Coulomb explosion,''[10] has been discussed as a mechanism of plasma channel formation.[4,5]

For a relatively short laser pulse, $\tau < r_0/u_i \sim 1$ ps, the velocity acquired an ion (with the mass M) from the laser pulse can be estimated as $u_i = (Z/M) mc^2 \nabla_r \int dt \sqrt{1+a^2/2}$. Then one finds the ion kinetic energy

$$\epsilon_i = \frac{Z^2}{2M} m^2 c^4 \left(\nabla_r \int dt \sqrt{1+\frac{a^2}{2}} \right)^2, \tag{1}$$

and the corresponding pulse energy loss per unit length, $d\mathcal{E}/dz \simeq -2\pi \int r dr n_i \epsilon_i$. According to the observations there is a characteristic maximum ion energy ~ 300 keV. Formula (1) also predicts the high-energy cutoff. For estimates we assume a Gaussian pulse shape in time and over the radius, $I = I_{\max} \exp(-t^2/\tau^2 - r^2/r_0^2)$, with $\tau \simeq 240$ fs. Then to accommodate the maximum ion energy of 300 keV with 50% laser energy trapping in the channel, the laser channel radius in Eq. (1) has to be $r_0 \simeq 3\mu$m, which determines the maximum laser intensity, $I_{\max} \sim 8.3 \times 10^{18}$ W/cm^2. These estimates of the channel radius and laser intensity qualitatively agree with the theory of relativistic self-focusing Refs. 1 and 11. The group of fast ~ 300 keV ions is responsible for the preionization of ambient gas (cf. Fig. 3b, curve *1*). Equation (1) predicts a rather wide energy spectrum of the ions with mean energy of ~ 130 keV. These ions are initially concentrated in a cylinder of radius $R \sim 5\ \mu$m and then begin to expand radially. These ions are responsible for the bulk of the ionization of the ambient gas (50%, cf. Fig. 3b, curve *2*). The characteristic energy deposited into these ions is $d\mathcal{E}/dz \sim$ 0.5 J/cm, which constitutes about 6% of the laser pulse energy trapped in a channel 1 mm in length.

There are also relatively low-energy ions (about 10 keV) expelled from a larger radius, $r_{\text{ch}} \approx 15\ \mu$m, which are responsible for the slow dynamics of the plasma channel. They are accelerated by the low-intensity wings of the untrapped part of the laser beam. According to Eq. (1), the intensity required for acceleration of these ions is below 10^{18} W/cm^2.

This regime of plasma channel formation due to the ion acceleration (''Coulomb explosion'' according to the terminology of Ref. 10) is completely different from the mechanism of plasma thermal heating and electron-impact ionization. In the latter case

plasma expands with the ion acoustic velocity.[2] The electron temperature T_e can be estimated as about 100 eV, according the measurements of Ref. 5 for conditions similar to the present experiment. Therefore the ion acoustic velocity $c_s=\sqrt{ZT_e/M}\sim 7\times 10^6$ cm/s in our experiment is less than one-tenth of the ion expansion velocity. We also disagree with the conclusion of Ref. 5 that the plasma expands at the ion acoustic velocity, since the conditions of that experiment are similar to ours.

Initially the accelerated ions propagate through a plasma ($R<r_p\sim 40$ μm) and cannot be seen with our diagnostic tools. After a delay time $t_d=r_p/u_i\sim 10$ ps they penetrate into the neutral gas ($r>r_p$) and begin to ionize it. Although the ionization consumes a negligible part of ion energy, it proceeds very efficiently because the fast ion velocity, $u_i\sim(2-4)\times 10^8$ cm/s, is comparable to the velocity of bound electrons in the helium atom. These conditions correspond to the maximum of the ionization cross-section $\sigma_i\sim 3\times 10^{-16}$ cm^2 (Ref. 13). It is about an order of magnitude larger than the cross section of He ionization due to electron collisions.

The electron density at the radius r behind the group of fast ions can be estimated as $n_e\approx n_{He}^2 r_0^2\sigma_i/r$. This corresponds to about 10% ionization at $r\sim 100$ μm. The degree of preionization decreases with r as the fast ion flux decreases. The 100 eV electrons that accompany fast ions can also contribute to the gas ionization at a level of a few percent. According the same formula, the main (130 keV) ions that penetrate into the preionized gas somewhat later produce three times higher ionization at the same distance. Thus one may expect about 50% ionization for $r\sim 100$ μm, in agreement with experimental results. The total number of the electrons behind the ion front increases linearly with time, while the average electron density is inversely proportional to t. All these qualitative relations as well as the number of the electrons agree with data shown in Fig. 3a.

In conclusion, the temporal evolution of the plasma channel created due to the relativistic self-focusing of a 4 TW, 400 fs laser pulse has been observed for the first time using the interferometric technique with high spatial and temporal resolution. By comparison of the experimental data with theoretical estimates we demonstrate that the channel evolution is dominated by the Coulomb explosion effect, with the subsequent penetration of high-energy ions into the ambient neutral gas. This experiment reveals a new efficient mechanism of direct deposition of the laser energy into the high-energy ions ($\sim$6% for our conditions), which can play a fundamental role in the absorption short, high-intensity laser pulses. We estimate the fast ion energy as $\sim$300 keV or 80 keV/nucleon, which is comparable to that observed in a solid-target experiment.[14]

The authors would like to acknowledge Dr. S. Pikuz for useful discussion. This work was supported by NSF PHY 972661, NSF STC PHY 8920108, DOE/LLNL subcontract B307953, and the Russian Fund for Fundamental Research (Grants 96-02-16707-a and 96-02-16165-a).

[a)]e-mail: sarkisov@sci.lebedev.ru

[1] A. B. Borisov, A. V. Borovskiy, V. V. Korobkin *et al.*, Phys. Rev. Lett. **68**, 2309 (1992).
[2] M. Dunne, T. Afshar-Rad, J. Edwards *et al.*, Phys. Rev. Lett. **72**, 1024 (1994).
[3] A. J. MacKinnon, M. Borgesi, A. Iwase *et al.*, Phys. Rev. Lett. **76**, 1473 (1996); M. Borghesi, A. J. MacKinnon, L. Barringer *et al.*, Phys. Rev. Lett. **78**, 879 (1997).

[4] D. Umstadter, S. Y. Chen, A. Maksimchuk *et al.*, Science **273**, 472 (1996).
[5] K. Krushelnik, A. Ting, C. I. Moore *et al.*, Phys. Rev. Lett. **78**, 4047 (1997).
[6] V. Malka, E. Wispelaere, F. Amiranoff, and S. Baton, Phys. Rev. Lett. **79**, 2979 (1997).
[7] P. Maine, D. Strickland, P. Bado *et al.*, IEEE J. Quantum Electron. **QE-24**, 398 (1988); M. D. Perry and G. Mourou, Science **264**, 917 (1994).
[8] G. S. Sarkisov, Instrum. Exp. Tech. **39**, 727 (1996).
[9] S. Augst, D. Strickland, D. D. Meyerhofer *et al.*, Phys. Rev. Lett. **63**, 2212 (1989).
[10] N. H. Burnett and G. D. Enright, IEEE J. Quantum Electron. **QE-26**, 1797 (1990).
[11] P. Sprangle, E. Esarey, J. Krall, G. Joyce, Phys. Rev. Lett. **69**, 2200 (1992); K. C. Tzeng, W. B. Mori, C. D. Decker, Phys. Rev. Lett. **76**, 332 (1996); P. Mora and T. M. Antonsen, Phys. Plasmas **4**, 217 (1997).
[12] T. E. Glover, T. D. Donnelly, E. A. Lipman *et al.*, Phys. Rev. Lett. **73**, 78 (1994); W. J. Blyth, S. G. Preston, A. A. Offenberger *et al.*, Phys. Rev. Lett. **74**, 554 (1995).
[13] R. K. Janev, L. P. Presnyakov, and V. P. Shevelko, in *Physics of Highly Charged Ions*, edited by G. Ecker, Springer-Verlag, 1985.
[14] A. Fews, P. A. Norreys, F. N. Beg *et al.*, Phys. Rev. Lett. **73**, 1801 (1994).

Published in English in the original Russian journal. Edited by Steve Torstveit.

Critical dynamics of spin systems in the four-loop approximation

V. V. Prudnikov,[a] A. V. Ivanov, and A. A. Fedorenko
Omsk State University, 644077 Omsk, Russia

(Submitted 29 October 1997)
Pis'ma Zh. Éksp. Teor. Fiz. **66**, No. 12, 793–798 (25 December 1997)

A field-theoretic description of the critical dynamics of spin systems is constructed. Using the Padé–Borel summation technique, the dynamic critical exponent for two- and three-dimensional systems is evaluated directly in the four-loop approximation. The results are compared with the values obtained for the dynamic exponent by Monte Carlo methods.
 [S0021-3640(97)00924-9]

PACS numbers: 03.70.+k, 75.40.Cx

Renormalization group methods are widely used to describe the anomalous properties of the thermodynamic characteristics of systems undergoing second-order phase transitions. Such methods make it possible to calculate the critical exponents characterizing the asymptotic behavior of the thermodynamic and correlation functions near the critical temperature. Of these methods the most promising is the field-theoretic approach.[1] It has two important advantages. First, it makes it possible to use the powerful and convenient mathematical arsenal developed in quantum field theory. This is especially important for calculating the high-order fluctuation corrections for second-order phase transitions on the basis of the perturbation theory. Second, it makes it possible to perform calculations directly for $d=2$, 3 in the form of an expansion in terms of the interaction vertex of magnetization fluctuations without using an ε expansion ($\varepsilon=4-d$, where d is the dimension of the system). Thus far calculations of the static critical exponents describing the equilibrium behavior of a system near a critical point have been performed on the basis of this approach for the $g\varphi^4$ model in the six-loop approximation.[2] The values so obtained for the exponents are considered to be most accurate. However, calculations with this degree of accuracy are not available for the nonequilibrium properties of systems undergoing second-order phase transitions. This is due, above all, to the fact that the volume of calculations grows rapidly even in the lowest orders of perturbation theory. The most accurate results have been obtained in Ref. 3, where the calculations were performed in the three-loop approximation.

In the present letter we construct a field-theoretic description of the nonequilibrium critical behavior of ferromagnets in the four-loop approximation. The model consists of a classical spin system that is thermodynamically equivalent to the $O(n)$ symmetric Ginzburg–Landau model with effective Hamiltonian

$$\mathcal{H}=\frac{1}{2}\int d^dx\left(r_0\varphi^2+(\nabla\varphi)^2+\frac{g_0}{12}\varphi^4\right), \tag{1}$$

where d is the dimension of the system, $\varphi(\mathbf{x},t)$ is a n-component order parameter (magnetization), $r_0 \sim T - T_{oc}$ (T_{oc} is the critical temperature determined by the mean-field theory), and $g_0 > 0$ is the interaction vertex of the magnetization fluctuations.

The dynamical behavior of a magnet in the relaxation regime near the critical point is described by a Langevin-type kinetic equation for the magnetization:

$$\frac{\partial \varphi}{\partial t} = -\lambda_0 \frac{\delta \mathcal{H}}{\delta \varphi} + \zeta + \lambda_0 h, \tag{2}$$

where λ_0 is a transport coefficient, $\zeta(\mathbf{x},t)$ is a random force, and $h(\mathbf{x},t)$ is the external magnetic field. It is known that its solution in the form of correlation functions can be obtained using a generating functional of the form

$$\Omega = \int D[\varphi] D[\psi] \exp\left(-\mathcal{H}_{\text{eff}}[\varphi, \psi] + \int \varphi h d^d dt \right), \tag{3}$$

where an auxiliary field ψ and the effective Hamiltonian

$$\mathcal{H}_{\text{eff}} = \int d^d x dt \left(\lambda_0^{-1} \varphi^2 + i\psi \left(\lambda_0^{-1} \frac{\partial \varphi}{\partial t} + \frac{\delta \mathcal{H}}{\delta \varphi} \right) \right) \tag{4}$$

have been introduced. The magnetization correlation function is then determined as

$$G(x,t) = \langle \varphi(0,0) \varphi(x,t) \rangle = \frac{1}{\Omega} \frac{\delta^2 \Omega}{\delta h(0,0) \delta h(x,t)}. \tag{5}$$

Instead of the correlation function it is more convenient to study its vertex part, which can be represented in the Feynman diagram formalism in the four-loop approximation as

$$\Gamma^{(2)}(k, \omega; r_0, g_0, \lambda_0) = r_0 + k^2 - \frac{i\omega}{\lambda_0} - \frac{n+2}{18}$$

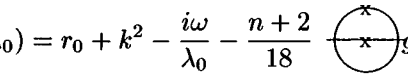

$$g_0^2$$

$$+ \frac{(n+2)(n+8)}{108} [$$

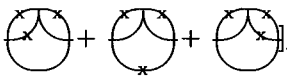

$$] g_0^3 - [\sum_{i=1}^{48} D_i^{(4)}] g_0^4.$$

The four-loop diagrams are presented in the figure. The Feynman diagrams contain a d-dimensional integration over momenta and are characterized near the critical point by an ultraviolet divergence with pole-type singularities at large momenta $\mathbf{k}$. These poles can be eliminated using a dimensional-regularization scheme in which renormalized quantities are introduced.[4] We define the renormalized order parameter as $\varphi = Z^{-1/2} \varphi_0$. Then the renormalized vertex functions will have the generalized form

$$\Gamma_R^{(m)}(k, \omega; r, g, \lambda, \mu) = Z^{m/2} \Gamma^{(m)}(k, \omega; r_0, g_0, \lambda_0) \tag{6}$$

with renormalized coupling constant g, temperature r, and transport coefficient λ

$$g_0 = \mu^{4-d} Z_g g, \quad r_0 = \mu^2 Z_r r, \quad \lambda_0^{-1} = \mu^2 Z_\lambda \lambda^{-1}, \tag{7}$$

where the scale parameter μ is introduced in order to make the quantities dimensionless. The factors Z are determined from the requirement that the renormalized vertex functions be regular, as reflected in the normalization conditions:

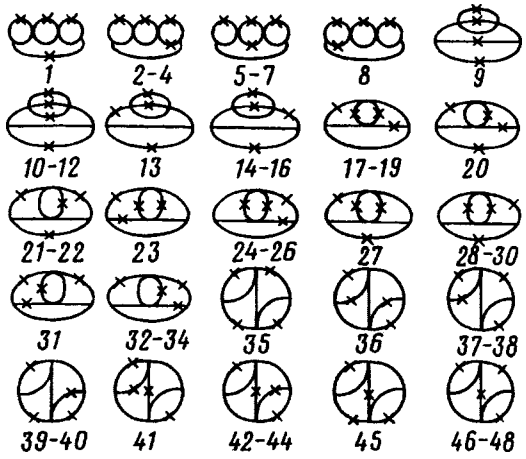

FIG. 1. Four-loop diagrams contributing to the vertex function. The solid lines represent the function $G_0(k,\omega)=(r_0+k^2-i\omega/\lambda_0)^{-1}$ and the crosses represent the function $C_0(k,\omega)=2\lambda^{-1}\times((r_0+k^2)^2+(\omega/\lambda_0)^2)^{-1}$.

$$Z\left.\frac{\partial\Gamma^{(2)}(k)}{\partial k^2}\right|_{k^2=0}=1,\quad Z^2\Gamma^{(4)}|_{k_i=0}=\mu^{4-d}g, \tag{8}$$

$$Z^2\Gamma^{(2,1)}|_{k_i,p_j=0}=1,\quad Z\left.\frac{\partial\Gamma^{(2)}(k,\omega)}{\partial(-i\omega)}\right|_{k^2,\omega=0}=\lambda^{-1}. \tag{9}$$

We carried out this regularization procedure for the vertex functions in the four-loop approximation. For this purpose we represent as follows the vertex functions appearing in the normalization conditions:

$$\Gamma^{(4)}|_{k_i=0}=g_0+A_1g_0^2+A_2g_0^3+A_3g_0^4, \tag{10}$$

$$\left.\frac{\partial\Gamma^{(2)}}{\partial k^2}\right|_{k^2=0}=1+B_1g_0^2+B_2g_0^3+B_3g_0^4, \tag{11}$$

$$\left.\frac{\partial\Gamma^{(2)}}{\partial(-i\omega)}\right|_{k=0,\omega=0}=1+C_1g_0^2+C_2g_0^3+C_3g_0^4, \tag{12}$$

where the coefficients are sums of the corresponding diagrams or their derivatives for zero external momenta and frequencies. The values of these coefficients for $n=1$ are presented in Table I. The diagrams in the figure which form the coefficient C_3 decompose into 48 $4d$-fold integrals, whose numerical values are given in Table II. We write the expansion of the quantities g_0, Z, and Z_λ in terms of the renormalized coupling constant g as

$$g_0=g+b_1g^2+b_2g^3+b_3g^4, \tag{13}$$

$$Z=1-z_1g^2-z_2g^3-z_3g^4, \tag{14}$$

TABLE I. Values of the coefficients in the expressions for the vertex functions.

Coefficient	$d=2$	$d=3$
A_1	−1.0	−1.0
A_2	1.3750699	1.2222222
A_3	−2.3054548	−1.7053479
B_1	0.0084916	0.0054869
B_2	−0.0116591	−0.0070112
B_3	0.0179966	0.0101430
C_1	0.0152547	0.0096865
C_2	−0.0213740	−0.0126257
C_3	0.0352450	0.0169420

$$Z_\lambda = 1 + d_1 g^2 + d_2 g^3 + d_3 g^4, \tag{15}$$

where the unknowns b_i, z_i, and d_i are expressed in terms of A_i, B_i, and C_i with the aid of the normalization conditions. The next step in the field-theoretic approach is to determine the scaling functions that determine the differential equation of the renormalization group:

$$\left[\mu\frac{\partial}{\partial\mu} + \beta\frac{\partial}{\partial g} - r\gamma_r\frac{\partial}{\partial r} + \lambda\gamma_\lambda\frac{\partial}{\partial\lambda} - \frac{m}{2}\gamma_\phi\right]\Gamma_R^{(m)} = 0. \tag{16}$$

To discuss the dynamical behavior we shall require only the functions $\beta(g)$ and $\gamma_\lambda(g)$:

$$\beta(g) = -(4-d)\left[\frac{\partial \ln Z_g g}{\partial g}\right]^{-1}, \quad \gamma_\lambda(g) = \beta(g)\frac{\partial \ln Z_\lambda}{\partial g}. \tag{17}$$

TABLE II. Values of the four-loop diagrams.

N	$d=2$	$d=3$	N	$d=2$	$d=3$	N	$d=2$	$d=3$
1	0.165307	0.104869	17	0.004131	0.001108	33	0.007463	0.002527
2	0.009670	0.004166	18	0.003307	0.000923	34	0.029449	0.014580
3	0.022921	0.008180	19	0.003343	0.000932	35	0.070254	0.039776
4	0.059714	0.029674	20	0.034609	0.019410	36	0.006421	0.002378
5	0.003943	0.003264	21	0.034135	0.019189	37	0.012723	0.004691
6	0.010076	0.015354	22	0.011294	0.004177	38	0.007370	0.003820
7	0.028777	0.014330	23	0.004644	0.001928	39	0.027311	0.011650
8	0.016314	0.011627	24	0.005891	0.000706	40	0.013297	0.005377
9	−0.006853	−0.002506	25	0.010167	0.003421	41	0.007464	0.003981
10	0.002744	0.000823	26	0.003535	0.000862	42	0.010303	0.003314
11	0.009238	0.003444	27	0.002471	0.000551	43	0.023519	0.009470
12	0.010685	0.003745	28	0.011209	0.003898	44	0.010905	0.003866
13	−0.012280	−0.004883	29	0.003405	0.001077	45	0.038420	0.023730
14	−0.012280	−0.004883	30	0.011007	0.003815	46	0.062921	0.033485
15	0.017180	0.007527	31	0.012666	0.007379	47	0.021633	0.007121
16	−0.014199	−0.005471	32	0.009667	0.004177	48	0.011691	0.004760

The explicit form of the first of these functions in the six-loop approximation was obtained in Ref. 2. The dynamic scaling function $\gamma_\lambda(g)$ in the four-loop approximation, taking account of Eqs. (7)–(15), assumes the form

$$\gamma_\lambda(g) = -(4-d)g[2(B_1-C_1)+(3B_2-3C_2-4A_1B_1+4A_1C_1)g+(4B_3-4C_3 -9A_1B_2+9A_1C_2+10A_1^2B_1-10A_1^2C_1-4A_2B_1+4A_2C_1-8B_1D_1+6B_1^2 -2C_1^2)g^2]. \quad (18)$$

Substituting the values of the coefficients from Table I, we obtain

$$\gamma_\lambda(g) = 0.027053g^2 - 0.004184g^3 + 0.022130g^4, \quad (19)$$

for $d=2$ and $n=1$ and

$$\gamma_\lambda(g) = 0.008399g^2 - 0.000045g^3 + 0.020423g^4, \quad (20)$$

for $d=3$ and $n=1$. The dynamic exponent z characterizing the critical retardation of the relaxation processes is determined as

$$z = 2 + \gamma(g^*), \quad \beta(g^*) = 0, \quad (21)$$

where the values of the fixed points in the four-loop approximation[2] are

$$g^*(d=2) = 1.8836, \quad g^*(d=3) = 1.4299. \quad (22)$$

The series obtained are asymptotically convergent. We used the Padé–Borel method to sum them.[2] Using [3/1] approximants, we obtained the following values of the exponent z:

$$z^{(4)}(d=2) = 2.093, \quad z^{(4)}(d=3) = 2.017$$

while in the preceding (three-loop) approximation its values were $z^{(3)}(d=2)=2.066$ and $z^{(3)}(d=3)=2.016$, respectively. The small change in the exponent z for three-dimensional systems suggests that the higher-order corrections will give only very small changes, falling outside the accuracy of the experiment. For two-dimensional systems, however, there are no grounds for such an assertion.

Let us now compare our results with those obtained in other works. Monte Carlo simulation of the three-dimensional Ising model gives the following values: $z=1.99\pm0.03$,[5] 2.10 ± 0.02,[6] 1.97 ± 0.08,[7] and 2.04 ± 0.01.[8] The field-theoretic approach in the two-loop approximation with interpolation of the $1+\varepsilon$ and $4-\varepsilon$ expansion results gives $z=2.02$.[9] Hence one can see that, with the exception being Ref. 6, our value of the dynamic exponent $z^{(4)}(d=3)=2.017$ is in good agreement with the results obtained in the works cited. We present the results of a computer simulation of the two-dimensional Ising model: $z=2.14\pm0.02$,[5] 2.13 ± 0.03,[10], 2.076 ± 0.005,[11] 2.24 ± 0.04,[12] 2.24 ± 0.07,[13] and 2.16 ± 0.04;[14] for the field-theoretic approach in the two-loop approximation with interpolation of the $1+\varepsilon$ and $4-\varepsilon$ expansion results $z=2.126$ (Ref. 9) and the high-temperature expansion gives $z=2.183\pm0.005$.[15] Hence, one can see that for the two-dimensional Ising model the values of the exponent z lie in a quite wide range $2.08\leqslant z\leqslant 2.24$ and our values are near the lower limit. However, our procedure for calculating the exponents is considered to be most accurate, so that the computed values

can serve, we hope, as standards for computer simulations of homogeneous systems and can be used for developing methods for simulating disordered systems.

This research was supported by the Russian Fund for Fundamental Research (Grant No. 97-02-16124).

[a)]e-mail: prudnikv@univer.omsk.su

[1] E. Brezin, J. C. Le Guillou, and J. Zinn-Justin, in *Phase Transitions and Critical Phenomena*, edited by C. Domb and M. S. Green, Academic Press, New York, 1976, Vol. 6, p. 125.
[2] G. A. Baker, B. G. Nickel, and D. I. Meiron, Phys. Rev. B **17**, 1365 (1978).
[3] V. V. Prudnikov and A. N. Vakilov, Zh. Éksp. Teor. Fiz. **101**, 1853 (1992) [Sov. Phys. JETP **74**, 990 (1992)].
[4] N. N. Bogoliubov and D. V. Shirkov, *Introduction to the Theory of Quantum Fields*, Wiley, New York, 1980, 3rd edition [Russian original, Nauka, Moscow, 1976].
[5] C. Kalle, J. Phys. A **17**, L-801 (1984).
[6] H-O. Heuer, J. Phys. A **25**, L-567 (1992).
[7] V. V. Prudnikov and A. N. Vakilov, Zh. Éksp. Teor. Fiz. **103**, 962 (1993) [JETP **76**, 469 (1993)].
[8] U. Gropengiessen, Physica A **213**, 308 (1995).
[9] R. Bausch, V. Dohm, H. K. Janssen, and R. K. P. Zia, Phys. Rev. Lett. **47**, 1837 (1981).
[10] J. K. Williams, J. Phys. A **18**, 49 (1985).
[11] M. Mori and Y. Tsuda, Phys. Rev. B **37**, 5444 (1988).
[12] P. H. Poole, N. Jan, and D. I. Meiron, J. Phys. A **23**, L-453 (1990).
[13] V. V. Prudnikov and O. N. Markov, J. Phys. A **28**, 1549 (1995).
[14] F. Wang, N. Hatane, and M. Suzuli, J. Phys. A **28**, 4543 (1995).
[15] B. Daman and I. D. Reger, Z. Phys. B **98**, 97 (1995).

Translated by M. E. Alferieff

Characteristic features of the sorption of light atoms on the surface of a single-layer carbon tubelene

I. V. Zaporotskova and A. O. Litinskiĭ
Volgograd State University, 400062 Volgograd, Russia

L. A. Chernozatonskiĭ[a)]
Institute of Biochemical Physics, Russian Academy of Sciences, 117334 Moscow, Russia

(Submitted 18 July 1997; resubmitted 10 November 1997)
Pis'ma Zh. Éksp. Teor. Fiz. **66**, No. 12, 799–804 (25 December 1997)

The mechanisms of sorption of H, O, C, and Cl atoms on the surface of a single-layer carbon tubelene are studied, and a comparison is made with the case of sorption of these atoms on graphite. Three versions of the position of the adatoms above the surface were studied. A cyclic-cluster model and an appropriately modified MNDO computational scheme are used. The optimal geometry of the sorption complexes and the sorption energies are obtained. The high hydrogen accumulation efficiency in a material consisting of single-layer carbon nanotubes is explained. © *1997 American Institute of Physics.*
[S0021-3640(97)01024-4]

PACS numbers: 68.45.Da, 81.05.Ys

A great deal of attention is now being devoted to experimental and theoretical investigations of recently discovered new forms of carbon — nanotubes (or tubelenes).[1–6] These tubes, ranging up to several microns in length and several nanometers in diameter, consist of one or several graphite layers, depending on the preparation conditions. Tubelene structures are classified using the symbols (n,m) proposed by Hamada *et al.*[4] An (n,m) tube, characterized by chiral symmetry, is obtained by twisting a graphite fragment so that the last hexagon from a row lies above the first hexagon with displacement $m\mathbf{A}_1+n\mathbf{A}_2$, where $\mathbf{A}_1$ and $\mathbf{A}_2$ are primitive translation vectors of the graphite fragment. The following names have been adopted for tubelenes exhibiting cylindrical symmetry: (n,n) tubelene — armchair-type, $(n,0)$ tubelene — zigzag-type. Theoretical investigations have shown that depending on the diameter and chirality tubes can possess both metallic, for example, (n,n) tubes, and semiconductor conductivity.[5,6] At present, a structure in which the elastic properties and conductivity of individual multilayer nanotubes[6,7] and bundles of single-layer tubes ~ 1 nm in diameter[8] has been prepared and investigated.

In the present letter we call attention to the fact that on account of their strongly curved surface tubelenes, just as fullerenes (which attach to themselves different atoms, radicals and functional groups, and on whose basis compounds with different physical chemical properties are obtained[6]), can be of great interest as a strong sorbent of atoms. The sorption properties of small-diameter nanotubes, comparable in size to C_{60} and C_{70}, are calculated. The characteristics of sorption of light atoms (adatoms) on the surface of

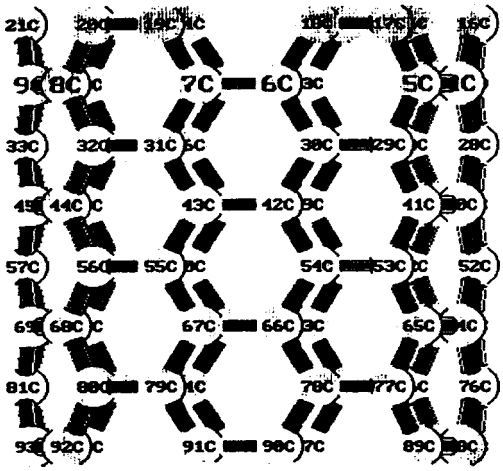

FIG. 1. Expanded unit cell of a (6, 6) nanotube.

single-layer (6, 6) carbon tubelene with a diameter of 8 Å are determined — a comparison with the case of sorption of the same adatoms on graphite showed that the sorption is highly efficient. A more detailed calculation is made of the sorption of hydrogen atoms on the surface of a nanotube in the ratio C_4/H, which suggested an explanation of the recently observed high efficiency of hydrogen accumulation in a carbon nanotube material.[9]

Previously, calculations of the electronic structure of nanotubes were performed using methods such as the *ab initio* method,[10] the local-density approximation,[11] cyclic cluster in Hückel-type computational schemes,[12] the extended Hückel method, and others.[5] In the present letter we present MNDO (modified neglect of diatomic overlap) calculations performed with a cyclic-cluster model[13] for the most often observed one-layer tube[8,9] — the armchair type. Cyclic boundary conditions in the direction of the nanotube axis were imposed on the molecular orbitals (MOs) of a cylindrical expanded unit cell (EUC), containing 96 atoms and consisting of four carbon armchair chains (Fig. 1). The matrix elements of the one-electron Hamiltonian (Fock operator — F) of the EUC in the MNDO approximation are[13]

$$F_{rq}^{AA}=\delta_{rq}U_{rr}+\sum_{r'q'}^{(A)}P_{r'q'}\left[\langle rq|r'q'\rangle-\frac{1}{2}\langle rr'|qq'\rangle\right]+\sum_{B(\neq A)}\left[\sum_{pt}^{(B)}P_{pt}\langle rq|pt\rangle-Z_B\langle rq|_{S_BS_B}\rangle\right], \tag{1}$$

$$F_{rt}^{AB}=\beta_{rt}^{0(AB)}S_{rt}^{AB}-\frac{1}{2}\sum_{r'}^{A}\cdot\sum_{t'}^{B}P_{r't'}\langle rr'|tt'\rangle, \tag{2}$$

where r, q, r', and q' are s-, p-, and d-type atomic orbitals localized on atom A; p, t, p', and t' are atomic orbitals on atom B; U_{rr} is the kinetic and potential energy of an

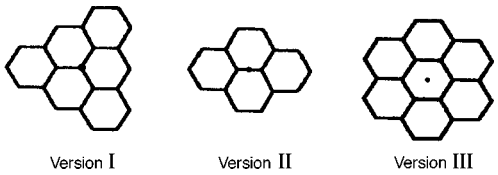

FIG. 2. Fragments of an expanded unit cell with an indication of the position of the sorbate atom.

electron in atom A; δ_{rq} is the Kronecker δ-function; P is the density matrix (matrix of bond orders); Z_B is the charge on a B atom; $\beta_{rt}^{0(AB)}$ is a resonance integral; S is the matrix of interatomic overlaps; $\langle rr'|qq'\rangle$ and $\langle rq|pt\rangle$ are one- and two-center electron repulsion integrals, respectively; and, s_B are s-type atomic orbitals of atom B.

The imposition of cyclic boundary conditions on the MOs of the EUC reduces to the fact that the two-center integrals of the type S_{rt}^{AB} and $\langle r_A q_A|p_B t_B\rangle$ in Eqs. (1) and (2) (we denote them as g(A, B)) can be calculated for each pair of atoms (A, B) within a prefixed interaction radius R_0, i.e., at distances $R_{AB}<R_0$. If for a given A $\in$ EUC and B $\in$ EUC the distance $R_{AB}>R_0$ and the translation vector of the EUC transfers an atom B $\in$ EUC into an atom B $\in$ EUC such that $R_{AB}\leqslant R_0$, then the function g(A, B′) is calculated as g(A, B).

In our case the dimensions of the expanded unit cell (along the tube axis L(EUC)=8.4 Å) made it possible to choose R_0 such that interactions up to the third sphere of neighbors inclusively are taken into account, which, in contrast to previously employed methods, makes it possible to make allowance for the nanotube curvature quite accurately.

Three versions of adsorption of atoms were studied: I) above a carbon atom, II) above the center of the C–C bond, and III) above the center of the hexagon (Fig. 2). The

TABLE I.

	r_{ad}, Å	E_s, eV	Q_A	r_{ad}, Å	E_s, eV	Q_A	r_{ad}, Å	E_s, eV	Q_A
		I			II			III	
				Sorption on the surface of a (6,6) nanotube					
H	2.1	4.7	0.67	1.5	4.0	0.62	1.6	4.5	0.76
O	2.0	4.9	−1.98	−	−	−	1.5	2.6	−1.99
C	1.8	9.4	1.31	−	−	−	1.5	5.1	1.3
Cl	1.5	6.9	−0.98	1.4	1.2	−0.98	−	−	−
				Sorption on the surface of a graphite layer					
H	1.4	2.56	0.27	1.3	−0.7	0.31	1.4	3.08	0.22
O	2.0	0.56	−1.99	1.5	2.02	−1.97	1.3	−5.0	−1.97
C	1.6	1.47	0.50	1.5	−1.2	0.36	1.6	−2.4	0.81
Cl	2.0	1.13	−0.99	2.2	1.32	−0.99	2.5	0.36	−0.99

C–C bond lengths in a tubelene were assumed to be 1.4 Å. The distances between the adatoms and the tubelene surface were optimized (see Table I). The quite large value of L shows that the interaction of adatoms from different EUCs can be neglected, i.e., it can be assumed that adsorption of a single atom is studied.

The calculation of the difference of the total energies of the electronic system of a noninteracting absorbent and the corresponding atom and their sorption complex (Table I) showed that the position I on the tubelene surface is energetically the most advantageous position for all adsorbed atoms. In the case of the sorption of H and C atoms electron density ($\Delta\rho_{ad}$) is transferred from the adatom to the surface in all cases and for O and Cl atoms electron density is transferred from the surface to the adatom, and in addition these atoms transform practically completely into the anions O^{2-} and Cl^{-}.

For comparison, we performed calculations of sorption of the same atoms on a graphite surface (in the one-layer approximation) in the same positions as in a nanotube (see Table I). This surface was modeled by a cyclic cluster with the composition C_{72} (6×6 unit cells), forming a uniformly expanded graphite cell whose MOs were required to satisfy cyclic boundary conditions. It was found that the most advantageous positions are: for H — above the center of a hexagon, for O and Cl — above the center of a bond, and for C — above a carbon atom on the surface. The computed sorption energies of the selected atoms on graphite agree well with existing experimental data: E_s(exp) (H) = 2.5 eV[14] and E_s(exp) (O) = 2.0–3.5 eV.[15]

The fact that the most advantageous version of sorption of the adatoms studied is above a carbon atom of tubelene can be explained by the fact that the sorption bond is stronger because it has a higher *s*-type fraction (appearance of ps^{δ} hybridization, where δ is small but nonzero).

The study of the character of the damping of a disturbance produced on the surface by the adatoms showed (see Table II) that the following. 1) The disturbance completely damps out at the boundaries of a cluster (on the carbon atoms — zero charges), confirming the conclusion that the sorption is singular. 2) In contrast to graphite, the degree of damping of a disturbance on a tubelene surface is direction dependent: It decays more slowly along the axis of the tube than along the circumference of the tube. 3) The disturbance introduced by adsorbed hydrogen decays more rapidly than a disturbance produced by O, C, and Cl atoms. Thus, in the case when a H atom is adsorbed in the position I, the disturbance extends to the first interaction sphere along the circumference and to the third sphere along the axis of the tubelene. For complexes with O, C, and Cl atoms in the same positions, the disturbance extends to the third and fourth spheres, respectively. 4) The greatest disturbance of the surface occurs in the cases when H and Cl are adsorbed above a bond (II) and O and C are adsorbed above an atom (I).

It was recently shown that hydrogen gas can condense up to high densities in a material consisting of bundles of single-walled carbon nanotubes.[9] However, a simple calculation[9] of the coverage by densely packed H_2 molecules inside a nanotube (with nearest-neighbor distance 3.51 Å and with molecules approaching the wall to 2.95 Å) gave for a characteristic (10, 10) tube the ratio C_{21}/H_3 or 0.012 of the weight of a carbon nanotube. This estimate is 2.5–5 times below the experimental data. As noted by the

TABLE II.

	Spheres of interaction		1	2	3	4	5
H	*a* (along axis)	I	0.10	0.05	0.01	0.0	0.0
		II	0.14	0.07	0.02	0.0	0.0
		III	0.11	0.06	0.01	0.0	0.0
	b (along circumference)	I	0.10	0.01	0.0	0.0	0.0
		II	0.14	0.03	0.0	0.0	0.0
		III	0.11	0.03	0.0	0.0	0.0
O	*a*	I	0.58	0.25	0.14	0.07	0.0
		III	0.28	0.21	0.15	0.05	0.0
	b	I	0.58	0.08	0.03	0.0	0.0
		III	0.28	0.07	0.02	0.0	0.0
C	*a*	I	0.40	0.21	0.04	0.02	0.0
		III	0.20	0.13	0.05	0.03	0.0
	b	I	0.40	0.10	0.01	0.0	0.0
		III	0.20	0.10	0.02	0.0	0.0
Cl	*a*	I	0.42	0.20	0.09	0.04	0.0
		II	0.48	0.21	0.11	0.06	0.0
	b	I	0.42	0.10	0.03	0.0	0.0
		II	0.48	0.12	0.03	0.0	0.0

authors,[9] a possible explanation is that hydrogen is adsorbed on the outer walls of the carbon nanotubes.

Using the method presented above, we calculated two versions (Fig. 3) of a carbon

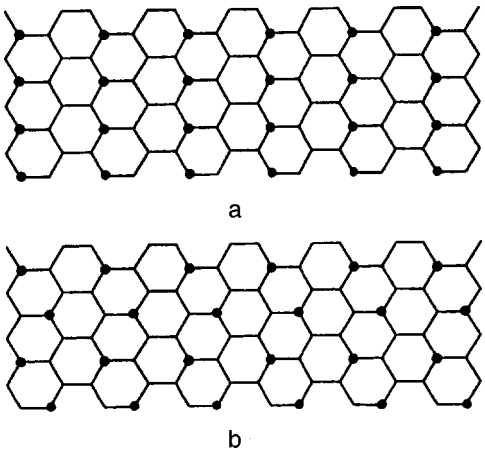

FIG. 3. Expanded unit cells of a (6, 6) carbon tube, unfolded in a plane, with an indication of the positions of the hydrogen atoms (filled circles) on the surface in two (a, b) computational versions.

tube with hydrogen atoms located above the carbon atoms (this position of sorption of one H atom is energetically advantageous, see Table I). It was found that from the energy standpoint it is even more advantageous for a group of hydrogen atoms to settle above opposite vertices of hexagons, Fig. 3b ($r_{ad}=1.2$ Å, $Q_H=0.11$, and $E_s=5.2$ eV), and not in chains, Fig. 3a ($r_{ad}=1.2$ Å, $Q_H=0.15$, and $E_s=4.5$ eV). Such hydrogenization can be represented qualitatively as follows. A H_2 molecule approaching close to a metallic nanotube is subjected to image forces, the interaction energy ($E_0\cong -4.5$ eV)[16] between hydrogen atoms in the molecule decreasing: $E'\cong E_0+e^2/d$,[17] e is the electron charge, and d is the distance from the metal surface. The coupling force of these atoms decreases substantially at $d\cong 1.5$ Å, and the atoms strive to occupy the most advantageous position above the carbon atoms at opposite vertices of the hexagon (Fig. 3b). Allowing for hydrogen sorption in the ratio C_4/H on the surface of the same (10, 10) tube characteristic for the material, we obtain reasonable agreement with experiment:[9] The total fraction of hydrogen atoms (on the surface and in the channel — C_{420}/H_{165}) is now 0.033 of the weight of such a material.

So, our calculations have shown that carbon tubes with nanometer diameter possess the 2 to 6 times greater sorption power for sorbing light atoms than graphite. This opens up new prospects for using such tubes as sorbents of atoms of other elements or molecules and for obtaining new materials and polymers by saturating the free bonds of the adatoms.

We thank E. G. Gal'pern and I. V. Stankevich for a discussion of this work and Yu. E. Lozovik for a helpful debate and a discussion of the possible mechanism of hydrogen adsorption on a metal nanotube. One of us (L. A. C.) is grateful to the Japanese Society for the Support of Science. This work was supported by the Russian Fund for Fundamental Research (Grant 96-02-18445-a).

[a)]e-mail: cherno@sky.chph.ras.ru

[1] S. Iijima, Nature **354**, 56 (1991).
[2] T. W. Ebbesen and P. M. Ajayan, Nature **358**, 220 (1992).
[3] Z. Ya. Kosakovskaya, L. A. Chernozatonskiĭ, and E. A. Fedorov, JETP Lett. **56**, 26 (1992).
[4] N. Hamada, S. Sawada, and A. Oshiyama, Phys. Rev. Lett. **68**, 1579 (1992).
[5] J. W. Mintmire and C. T. White, Carbon **33**, 893 (1995).
[6] M. S. Dresselhaus, G. Dresselhaus, and P. C. Eklund, *Science of Fullerenes and Carbon Nanotubes*, Academic Press, New York, 1996.
[7] M. M. J. Trecy, T. W. Ebbesen, and J. M. Gibson, Nature **381**, 678 (1996).
[8] J. Rao, V. Nokolaev, R. Smalley *et al.*, Science **275**, 645 (1997).
[9] A. C. Dillon, K. M. Jones, T. A. Bekkedahl *et al.*, Nature **386**, 377 (1997).
[10] Y. Jae-Yel and J. Bernhold, Phys. Rev. B **47**, 1708 (1993).
[11] Y. Miyamoto, A. Rubio, M. L. Cohen *et al.*, Phys. Rev. B **50**, 4976 (1994).
[12] I. V. Stankevich and L. A. Chernozatonskiĭ, JETP Lett. **63**, 621 (1996).
[13] A. O. Litinskiĭ, N. G. Lebedev, and I. V. Zaporotskova, Zh. Fiz. Khim. **69**, 215 (1995).
[14] J. P. Redmond and R. L. Walker, J. Phys. Chem. **64**, 1093 (1960).
[15] M. J. Marshall, Branston-Cook, Can. J. Research B **15**, 75 (1937).
[16] G. Herzberg, J. Mol. Spectrosc. **33**, 147 (1970).
[17] Yu. E. Lozovik and V. N. Nishanov, Fiz. Tverd. Tela (Leningrad) **18**, 3267 (1976) [Sov. Phys. Solid State **18**, 1905 (1976)].

Translated by M. E. Alferieff

Spectroscopic manifestations of the difference of the local symmetry of calamitic and discoidal nematics

E. M. Aver'yanov[a)]

L. V. Kirenskiĭ Institute of Physics, Siberian Branch of the Russian Academy of Sciences, 660036 Krasnoyarsk, Russia

(Submitted 13 November 1997)
Pis'ma Zh. Éksp. Teor. Fiz. **66**, No. 12, 805–810 (25 December 1997)

It is shown that the difference in the local symmetry of nematics consisting of rod-shaped and disk-shaped molecules is manifested as an observable qualitative difference in their spectroscopic characteristics. The well-known controversial experimental data are explained. [S0021-3640(97)01124-9]

PACS numbers: 61.30.Eb, 78.40.Dw

1. Calamitic (N) and discoidal (N_D) nematics, consisting of rod-shaped and disc-shaped molecules, respectively, have the same macroscopic symmetry but different local symmetry. A well-known consequence of the latter circumstance is that the sign of the reactive coefficient in the equations of hydrodynamics of these liquid crystals (LCs) is different.[1,2] Moreover, the difference of the local symmetry of N and N_D phases is manifested in the characteristics of the dipole–dipole intermolecular interactions and in the fact that the components of the Lorentz tensor L are in opposite relation for electric fields directed parallel ($\|$) and perpendicular ($\perp$) to the director **n**, i.e., $L_\| < L_\perp(N)$ and $L_\| > L_\perp(N_D)$ (Refs. 3 and 4). This creates a distinction wherein the N_D nematics can have a ferroelectric state[5,6] and also means that the local-field effects will have a different manifestation in the anisotropic spectroscopic properties of calamitic and and discoidal LCs. The latter aspect has thus far not been noted in the literature.

Recently, however, the substantial improvement in the accuracy of measurements of the positions ω_{mj} ($j=\|,\perp$) of the polarized IR absorption bands $K_j(\omega)$ of nematics N, smectics $A(S_a)$, and discotics $D_{h(0)}$ (Refs. 7 and 8) as well as the first polarization investigations of electronic absorption in the N_D and $D_{h(0)}$ phases[9,10] have shown that the dependences of the components ω_{mj} on the phase state of these LCs are characterized by large diversity and by anomalies whose origins are as yet unclear. In the present letter it is shown that the observed features of the variations of ω_{mj} reflect the different local symmetry of the corresponding LCs.

2. Let us consider a uniformly oriented nematic N or N_D with orientational order parameter of the molecules $S=\langle 3\cos^2\theta_{\mathbf{l}\cdot\mathbf{n}}-1\rangle/2$, where $\theta_{\mathbf{l}\cdot\mathbf{n}}$ is the angle between the molecular symmetry axis **l** and the director **n**. Let us separate in the spectrum of the molecule an isolated nondegenerate transition with frequency ω_1, renormalized by the static intermolecular interactions in the LCs. The transition dipole moment **d** makes an angle β with the axis **l**. Near ω_1 the components $\epsilon_j(\omega)$ of the permittivity tensor of the LC can be represented in the form[3]

$$\epsilon_j(\omega)=\epsilon_{bj}+\frac{\omega_p^2F_jf_{bj}^2}{\omega_j^2-\omega^2+i\Gamma\omega},\quad \omega_j^2=\omega_1^2-\omega_p^2F_jL_jd_{bj}, \tag{1}$$

where ϵ_{bj} are the components of the background permittivity for the given transition, ω_p is the plasma frequency, $F_j=FC_j/3$, F is the transition oscillator strength, $C_\parallel=1+2SS_\beta$, $C_\perp=1-SS_\beta$, $S_\beta=(3\cos^2\beta-1)/2$, and $f_{bj}=1+L_j(\epsilon_{bj}-1)$ are the background components of the local-field tensor. The absorption coefficient $K_j(\omega)$ is given by the expression

$$K_j(\omega)=\frac{\sqrt{2}\omega}{c}[[(\epsilon_j')^2+(\epsilon_j'')^2]^{1/2}-\epsilon_j']^{1/2}, \tag{2}$$

where the real (ϵ_j') and imaginary (ϵ_j'') parts of the components $\epsilon_j(\omega)$, taking account of the inequalities $\omega_1\gg(\omega_1-\omega_j)$, $\omega_1\gg\Gamma$, can be put into the form

$$\epsilon_j'=\epsilon_{bj}-x\epsilon_j'',\quad \epsilon_j''=4a_j\epsilon_{bj}/(1+x^2). \tag{3}$$

Here $x=2(\omega-\omega_j)/\Gamma$ and $\alpha_j=(\omega_p^2F_jf_{bj}^2)/(4\Gamma\omega_j\epsilon_{bj})$. The position of the maximum ω_{mj} of the band $K_j(\omega)$ is determined by the solution of the equation

$$x^3-3a_jx^2-x+a_j=0. \tag{4}$$

For very strong absorption bands with $a_j\gg1$ it follows hence that $x_j\approx1/\sqrt{3}$ and

$$\omega_{mj}^{(S)}\approx\omega_j+\frac{\Gamma}{2\sqrt{3}}=\omega_1-\frac{\omega_p^2F_jL_jf_{bj}}{2\omega_1}+\frac{\Gamma}{2\sqrt{3}}. \tag{5}$$

For $a_j\leqslant1/4$ or $(\omega_1-\omega_j)\leqslant(0.2-0.4)\Gamma$, which is typical for IR and UV absorption bands of LCs, we obtain from Eq. (4), taking account of the Eq. (1),

$$\omega_{mj}^{(W)}=\omega_j+\frac{\omega_p^2F_jf_{bj}^2}{8\omega_j\epsilon_{bj}}=\omega_1-\frac{\omega_p^2f_{bj}L_jF_j}{2\omega_1}\left(1-\frac{f_{bj}}{4L_j\epsilon_{bj}}\right). \tag{6}$$

To analyze the shifts of the frequencies ω_{mj} at the transitions $I-N(N_D)-S_A(D_h)$we introduce the parameter

$$\delta_j=(\omega_{mj}-\omega_{mi})/(\omega_1-\omega_i), \tag{7}$$

for which the expressions

$$\delta_j^{(S)}=1-3C_jL_jf_{bj}/f_{bi},\quad \delta_j^{(W)}=\frac{3\epsilon_{bi}-2}{4\epsilon_{bi}}-\frac{3C_jL_jf_{bj}}{f_{bi}}\left(1-\frac{f_{bj}}{4L_j\epsilon_{bj}}\right) \tag{8}$$

follow from Eqs. (1), (5), and (6). The surfaces $\delta_{\parallel,\perp}(S,\beta)$ have a line of intersection $\delta_j(S=0)=0$. For $S=1$, we have $\delta_\parallel^{(S)}(\beta=90°)=\delta_\perp^{(S)}(\beta=0)=1$, $\delta_\parallel^{(W)}(\beta=90°)=\delta_\perp^{(W)}\times(\beta=0)=(3\epsilon_{bi}-2)/4\epsilon_{bi}$, which also fix the surfaces $\delta_{\parallel,\perp}(S,\beta)$ at one end. A change in the anisotropy of the tensors ϵ_b, L, and f_b accompanying a change in the temperature, phase state, or type of LC is manifested as a deformation of the surfaces $\delta_{\parallel,\perp}(S,\beta)$ and a displacement of their free ends $\delta_\parallel(S=1,\beta=0)$ and $\delta_\perp(S=1,\beta=90°)$.

3. Let us now consider the experimental consequences of the relations (8). For LCs with small birefringence $\Delta n=n_\parallel-n_\perp$ we have $L_j\approx1/3$, $f_{bj}\approx f_{bi}$ (Ref. 3) and from Eq.

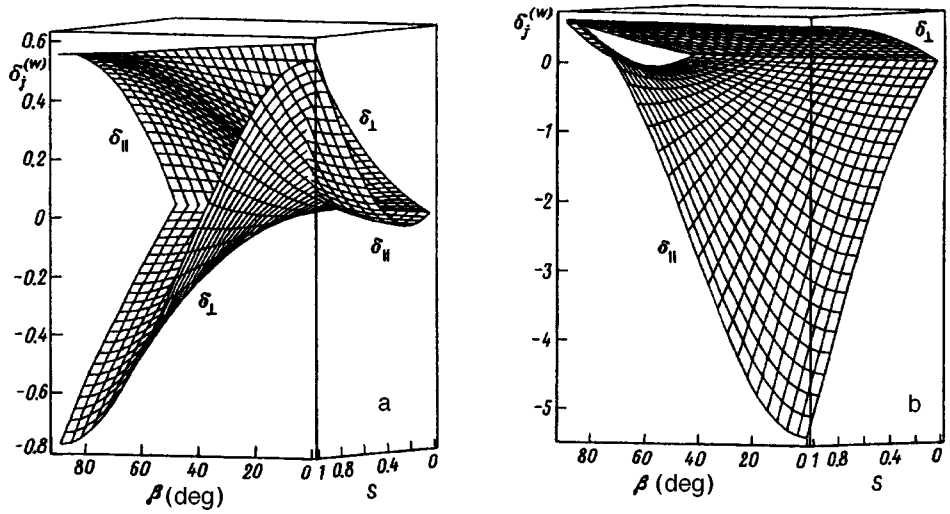

FIG. 1. $\delta^{(W)}(S,\beta)$ for calamitic (a) and discoidal (b) LCs calculated according to Eq. (8) with the parameters τ_0 and ϵ_{bij} presented in the text.

(8) we obtain $\delta_j^{(S)}=1-C_j$ and $\delta_j^{(W)}=\delta_j^{(S)}(3\epsilon_{bi}-2)/4\epsilon_{bi}$. For $\beta<\beta_M=54.7°$ ($\beta>\beta_M$) we have the inequalities $\delta_\parallel<0$, $\delta_\perp>0$ ($\delta_\parallel>0$, $\delta_\perp<0$) and the surfaces $\delta_{\parallel,\perp}(S,\beta)$ intersect along the straight line $\beta=\beta_M$. The splitting $\Delta\omega=\omega_{m\perp}-\omega_{m\parallel}$ is proportional to the oscillator strength F of the transition and depends strongly on the angle β of the orientation of the transition moment. For $\beta<\beta_M$ ($\beta>\beta_M$) we have $\Delta\omega>0$, $K_\parallel(\omega_{m\parallel})>K_\perp(\omega_{m\perp})$ ($\Delta\omega<0$, $K_\parallel<K_\perp$), in agreement with the data of Ref. 11 for the IR absorption band corresponding to vibration of the $C\equiv N$ bond in nematic and smectic S_B phases of the LC 4CCH. For fixed β we have $\Delta\omega\sim S$, which corresponds to $\Delta\omega$ increasing at a $N-S_B$ transition for the 4CCH band under discussion.[11]

To compare the consequences of the relations (8) with the data of Refs. 7–10, let us set $\Delta\epsilon_b=\epsilon_{b\parallel}-\epsilon_{b\perp}\equiv\Delta\epsilon_{b0}S$ and $L_j=1/3+b_jS$, where $b_\parallel=2\tau_0$ and $b_\perp=-\tau_0$.[3] For calamitic (discoidal) LCs we take $\tau_0=-0.12(0.24)$, $\Delta\epsilon_{b0}=0.73(-1.10)$, and $\epsilon_{bi}=\overline{\epsilon_b}=(\epsilon_{b\parallel}+2\epsilon_{b\perp})/3=2.53(2.60)$. These parameters are close to the experimental values for calamitic LCs[3] and also for a discoidal nematic[4] isomorphic to the objects investigated in Ref. 9.

The dependences $\delta_j^{(W)}(S,\beta)$ presented in Figs. 1a and b show a qualitatively different character of the effect of the anisotropy of the tensors L, ϵ_b, and f_b on the functions $\delta_j(S,\beta)$ for the two types of LCs under study, the anisotropy of the tensor L being the main factor. Compared with the case of isotropic tensors L, ϵ_b, and f_b, in calamitic (discoidal) LCs an increase of $|\tau_0|$ results in a displacement of the free ends of the surfaces $\delta_j(S,\beta)$ in opposite directions: upward (downward) — for $\delta_\parallel(S=1,\beta=0)$ and downward (upward) — for $\delta_\perp(S=1,\beta=90°)$. This is accompanied by a displacement of the line of intersection of the surfaces $\delta_\parallel(S,\beta)$ and $\delta_\perp(S,\beta)$, which for calamitic (discoidal) LCs corresponds to the values $\beta=\beta_0<\beta_M$ ($\beta_0>\beta_M$). Anisotropy of the tensor L in the calamitic (discoidal) LCs intensifies the splitting $\Delta\omega$ of the bands $K_j(\omega)$ for

transitions with $\beta=90°$ ($\beta=0$), induces a change of the sign of $\Delta\omega$ for values of β in the interval $\beta_0<\beta<\beta_M$ ($\beta_0>\beta>\beta_M$), and decreases $\Delta\omega$ for $\beta=0$ ($\beta=90°$). The latter explains the small difference $\omega_{m\parallel}\approx\omega_{m\perp}$ for IR absorption bands with $\beta\geqslant 0$ in calamitic nematic phases of pectinate polymers[7] and low-molecular compounds[12] with large birefringence and anisotropy of the tensor L.[3]

It is evident from Fig. 1a that for small β and $S=0.3-0.4$, close to the typical values of S near the temperature T_{NI} of the $I-N$ transition, the average value $\overline{\omega}_{mj}$ is virtually identical to ω_{mi}. This explains the small change in $\overline{\omega}_{mj}$ for bands with $\beta\geqslant 0$ at a $I-N$ transition and in a narrow interval of the nematic phase with low values of S.[7] The observed growth of $\overline{\omega}_{mj}$ for isolated IR absorption bands with $\beta\geqslant 0$ in the nematic and smectic A phases with decreasing temperature[7] corresponds to the data in Fig. 1a and is explained by an increase of S and anisotropy of the tensor L. In addition, the more rapid growth of $\delta_j^{(W)}$ for high values of S correlates with an appreciable change in $\overline{\omega}_{mj}$ at a $N-S_A$ transition and into the smectic phase.[7] A quantitative estimate of the shifts $\overline{\omega}_{mj}-\omega_{mi}$ at $I-N-S_A$ transitions can be obtained taking account of the fact that for the isotropic phase of a LC with $\epsilon_{bi}=2$ it follows from Eq. (6) that $\omega_1-\omega_{mi}^{(W)}=(\omega_1-\omega_i)/2$. For typical values $\nu_1-\nu_{mi}^{(W)}\approx 5\ \mathrm{cm}^{-1}$ for the IR absorption bands we obtain from Eq. (7) and the data in Fig. 1a with $S=0.6-0.8$ and $\beta=0$ $\overline{\nu}_{mj}-\nu_{mi}\approx 2-3\ \mathrm{cm}^{-1}$, in agreement with experiment.[7]

For absorption bands with $\beta\approx\beta_M$ and $K_\parallel\approx K_\perp$ in uniaxial LCs there is no contribution from static interband interactions to the observed splitting $\Delta\omega$ (Ref. 13) and $\Delta\omega$ is determined completely by the anisotropy of the tensors L, ϵ_b, and f_b. The observed relation $\omega_{m\parallel}>\omega_{m\perp}$ for the IR absorption bands with $K_\parallel\approx K_\perp$ in calamitic nematics[12] corresponds to the data of Fig. 1a.

As one can see from Fig. 1b, for discoidal LCs with $\tau_0=0.24$ the surfaces $\delta_\parallel^{(W)}\times(S,\beta)$ and $\delta_\perp^{(W)}(S,\beta)$ are divided by a gap and the relation $\omega_{m\perp}>\omega_{mi}$ holds irrespective of the values of S and β. This explains the increase in $\omega_{m\perp}$ for isolated IR absorption bands with different values of β at a $I-D_{h0}$ transition.[8] Electronic transitions polarized in the plane of the aromatic core of discoidal molecules are characterized by the value $\beta=90°$. In the N_D phase with $S=0.3-0.6$ (Ref. 4) from Fig. 1b it follows that for such bands $|\delta_\parallel^{(W)}|\leqslant\delta_\perp^{(W)}$ with nonmonotonic variation of $\delta_\parallel^{(W)}$. For this reason, at a $I-N_D$ transition a very small displacement of the maximum ω_m of an unpolarized absorption band near T_{NI} and a weak increase in ω_m far from T_{NI} can be expected. The latter has been observed in Ref. 9. The maximum ω_m of the weak electronic band undergoes, at the same time, a low-frequency shift on account of the fact that the static interactions make the determining contribution.[13]

In the discotic D_{h0} with $S\approx 0.9$ the static intermolecular interactions decrease ω_{mj} for electronic absorption bands and have virtually no effect on $\Delta\omega$.[13] The dependence of ω_{mi} in solution on the type of solvent can serve as a measure of the effect of these interactions on $\omega_{\perp n}$. As one can see from Fig. 1b, for electronic bands with $\beta=90°$ the relations $\omega_{m\perp}\geqslant\omega_{m\parallel}>\omega_{mi}$ are expected in the D_{h0} phase. This explains the increase in $\omega_{m\perp}$ for intense electronic absorption bands in a number of objects accompanying a transition from solution to the D_{h0} phase.[10,14] In addition, a larger increase in $\omega_{m\perp}$ is

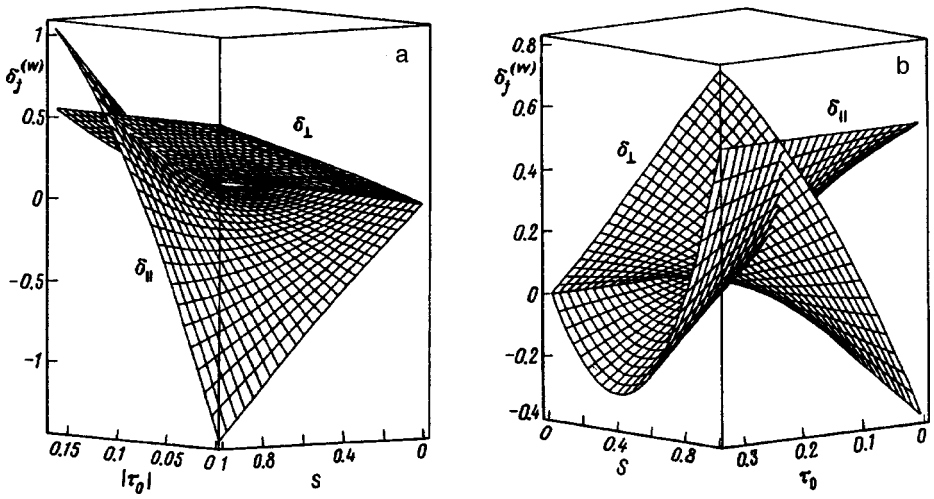

FIG. 2. $\delta^{(W)}(S,\tau_0)$ for calamitic (a) and discoidal (b) LCs calculated according to Eq. (8) with $\beta=0$ (a) and 90° (b) and the parameters ϵ_{bij} presented in the text.

observed in LCs[14] where the static intermolecular interactions have only a weak effect on the positions of ω_{mi} and $\omega_{m\perp}$.

For the weak electronic bands of the same objects, the small increase in $\omega_{m\perp}$ due to the resonance intermolecular interactions are compensated by a decrease in $\omega_{m\perp}$ on account of static interactions. As a result, for objects where the influence of static interactions on the position of ω_{mi} in solution is strong[10] and weak[14] $\omega_{m\perp}$ is observed to decrease[10] and remain constant[14] at a transition from solution into the D_{h0} phase. Thus the data[10,14] in the D_{h0} phase confirm that $\omega_{m\perp}$ increases as a result of resonance intermolecular interactions. If the static interactions made a determining contribution, then $\omega_{m\perp}$ would have decreased with increasing S for bands of any intensity with $\beta>\beta_M$.[13]

For β=const the surfaces $\delta_j(S,\tau_0)$ characterize the displacement of the polarized absorption bands with a change in temperature in the LCs with different anisotropy of the tensor L. Figure 2 displays the functions $\delta_j^{(W)}(S,\tau_0)$ for calamitic and discoidal LCs for values of β corresponding to the strongest manifestation of the anisotropy τ_0 of the tensor L in the possible ranges $(-1/6)\leqslant\tau_0(N)\leqslant 0$[3] and $0\leqslant\tau_0(N_D)\leqslant 1/3$,[4] taking account of the nonlocality of the molecular polarizability. Comparing Figs. 1 and 2 gives an idea of the behavior of the functions $\delta_j^{(W)}(S,\tau_0)$ for intermediate values $0<\beta<90°$.

4. In summary, the difference of the local symmetry between the calamitic and discoidal LCs is manifested as a qualitative difference between their observed spectroscopic features. In addition, the latter are determined mainly by the anisotropy of the tensor L. This distinguishes qualitatively the corrections to the position of the polarized absorption bands for local-field anisotropy from the analogous corrections to the intensities of these bands, which depend on the anisotropy of the tensor f_b.[3] It is significant that for LCs with a large anisotropy of the tensor L the tensor f_b can be isotropic.[3] The controversial experimental data on the dependence of ω_{mj} on the type of LC, the tem-

perature, the polarization of the bands, and the orientation of the transition moments[7–12,14] can be explained in a unified approach. The qualitatively different character of the functions $\delta_j(S)$ in Fig. 2 for calamitic ($\beta=0$) and discoidal ($\beta=90°$) LCs with large and small anisotropy of the tensor L makes it possible to judge the magnitude of this anisotropy without determining the components L_j experimentally. This presents new possibilities in searching for discoidal nematics satisfying the requirements[5,6] for a ferroelectric state to arise in them.

This work was supported by the Russian Fund for Fundamental Research through the Grant 97-03-33719 and the State Science and Technology Program ''Fundamental spectroscopy'' through Grant 2.3. I am grateful to Dr. D. Markovitsi for sending me reprints of Refs. 9 and 10.

[a)]e-mail: aver@iph.krasnoyarsk.su

[1] G. E. Volovik, JETP Lett. **31**, 273 (1980).
[2] E. I. Kats and V. V. Lebedev, *Dynamics of Liquid Crystals* [in Russian], Nauka, Moscow, 1988.
[3] E. M. Aver'yanov and M. A. Osipov, Usp. Fiz. Nauk **160**(5), 89 (1990); **160**(10), 206 (1990) [Sov. Phys. Usp. **33**, 365, 880 (1990)].
[4] E. M. Aver'yanov, Zh. Éksp. Teor. Fiz. **110,** 1820 (1996) [JETP **83**, 1000 (1996)].
[5] P. Palffy-Muhoray, V. A. Lee, and R. G. Petschek, Phys. Rev. Lett. **60**, 2303 (1988).
[6] C. Ayton and G. N. Patey, Phys. Rev. Lett. **76**, 239 (1996).
[7] J. K. Vij, A. Kocot, G. Kruk *et al.*, Mol. Cryst. Liq. Cryst. **237,** 337 (1993).
[8] G. Kruk, A. Kocot, R. Wrzalik *et al.*, Liq. Cryst. **14**, 807 (1993).
[9] S. Marguet, D. Markovitsi, D. Goldmann *et al.*, J. Chem. Soc. Faraday Trans. **93**, 147 (1997).
[10] P. Uznanski, S. Marguet, D. Markovitsi *et al.*, Mol. Cryst. Liq. Cryst. **293**, 123 (1997).
[11] B. O. Mirvold and P. Klaeboe, Spectrochim. Acta **42a**, 1035 (1986).
[12] N. Kirov and P. Simova, *Vibrational Spectroscopy of Liquid Crystals*, Publ. Bulg. Acad. Sci., Sofia, 1984.
[13] E. M. Aver'yanov, Opt. Spektrosk. **63,** 790 (1987) [Opt. Spectrosc. **63**, 469 (1987)].
[14] D. Markovitsi, A. Germain, P. Millie *et al.*, J. Phys. Chem. **99**, 1005 (1995).

Translated by M. E. Alferieff

Excitation of plasma oscillations during the motion of Josephson vortices in layered superconductors

S. N. Artemenko[a)] and S. V. Remizov
Institute of Radio Engineering and Electronics, Russian Academy of Sciences, 103907 Moscow, Russia

(Submitted 13 November 1997)
Pis'ma Zh. Éksp. Teor. Fiz. **66**, No. 12, 811–816 (25 December 1997)

The electric and magnetic fields arising during uniform motion of a vortex lattice in a magnetic field oriented parallel to the conducting layers are calculated in an exactly solvable model. For low temperatures and high velocities of the lattice, features due to the excitation of plasma oscillations of the superconducting electrons appear in the current–voltage characteristic. Peaks associated with plasmon excitation and the Cherenkov effect are present in the radiation spectrum.
 [S0021-3640(97)01224-3]

PACS numbers: 74.80.Dm, 74.50.+r, 74.25.Fy

Experimental[1,2] and theoretical[3–6] investigations performed in the last few years have shown that plasma oscillations of superconducting electrons at frequencies in the hundreds of megahertz to terahertz range exist in layered superconductors. The existence of a weakly damped characteristic mode results in resonance features in the forced oscillations when the frequency and wave vector of the driving force are close to those of the characteristic mode. Specifically, for sufficiently rapid motion of a lattice of Josephson vortices produced by a magnetic field oriented parallel to the layers, the frequencies of variation of the electromagnetic field fall within the same frequency range as the plasma oscillations. Under the influence of a transport current flowing in a direction perpendicular to the layers the velocity imparted to these vortices can be very high, since the modulus of the order parameter in them is disturbed very little. For this reason, for sufficiently high voltages on the superconductor it is possible that the conditions of resonance and generation of plasma oscillations are satisfied, which in turn should influence the form of the current–voltage characteristic (IVC). We present below a solution of the problem of the motion of a Josephson vortex lattice in an infinite crystal in not very strong magnetic fields, in which the nonlinear cores of the vortices do not overlap. We assume that the characteristic frequencies of the problem are low compared with the amplitude Δ of the order parameter.

The presence of vortices changes the characteristic oscillations, imparting to the spectrum an acoustic form.[7,8] However, the response of a superconductor to the motion of a vortex lattice under the action of a transport current is not associated with the oscillations of the vortices. For this reason, forced oscillations are determined by the characteristic modes with a plasma edge.

For high velocities the shape of the vortices changes. This makes it much more difficult to calculate the dynamics of the vortices, since the standard approach employing

the perturbation theory in the velocity becomes inapplicable. For a strict solution of the problem, it is necessary to solve Maxwell's equations into which expressions for the current and charge density are substituted. Having in mind high-temperature superconductors, we shall assume that the order parameter has the form characteristic for d pairing. The expressions for the charge and current densities are nonlinear functions of the phase difference of the order parameter between neighboring layers and in the general case have a quite complicated form.[9] Besides the dependence on the time derivatives of the superconducting momentum $\mathbf{P}_n=(1/2)i\mathbf{q}\chi_n-(1/c)\mathbf{A}_n$ and the phase difference, the quasiparticle current density also depends on the gradient of the gauge-invariant scalar potential $\mu_n=(1/2)(\partial\chi_n/\partial t)+\Phi_n$, where $\mathbf{A}_n$ is the vector potential, Φ_n is the electric potential, and χ_n is the phase of the order parameter in the nth layer. (We assume $\hbar=1$, $e=1$.) In the general case the potential μ_n is found from the solution of Poisson's equation, but in the problem of vortices at low temperatures $T\ll\Delta$, which we shall study, the imbalance of the populations of the quasiparticle branches and the potential μ_n due to this imbalance can be neglected if $(r_0/d)^2\ll 1$, where r_0 is the Thomas–Fermi screening radius and d is the period of the crystal in a direction perpendicular to the layers. The linear-response expression can be used for current along the layers, since in the problem of Josephson vortices the characteristic scale of the currents is determined by the critical current j_c in a direction perpendicular to the layers, and this current is small compared with the critical current in the direction of the layers. The expression for the current density in the nth layer, written in the Fourier representation, is

$$\mathbf{j}_n=\frac{c^2}{4\pi\lambda^2}\mathbf{P}_n-i\omega\sigma_{\parallel}(\omega)\mathbf{P}_n.$$

The first term here describes the superconducting current and the second term describes the quasiparticle current; $-i\omega$ and $i\mathbf{q}$ correspond to the time derivative and gradient in the direction of the layers. The frequency dependence of the conductivity $\sigma_{\parallel}(\omega)$ depends on the symmetry of the order parameter and is determined by the momentum scattering time. We shall employ for it the expression from Ref. 10.

The superconducting current density between the layers n and $n+1$ is determined by the expression

$$j_{\perp n}^{(s)}(\varphi_n)=j_c\ \sin\ \varphi_n,$$

where φ_n is the gradient-invariant phase difference. We shall switch to the exactly solvable model, replacing the sine by a saw-tooth function

$$j_{\perp n}^{(s)}(\varphi_n)=j_c\ \text{arcsin sin}\ \varphi_n, \tag{1}$$

as was done in Ref. 11. This substitution was also used in solving the problem of the motion of Josephson vortices in an approximation linear in the velocity.[12] In accordance with Eq. (1), we employ a linear dependence of the quasiparticle current on the phase difference:

$$j_{\perp n}^{(qp)}=-i\omega\sigma_{\perp}(\omega)\varphi_n/(2d).$$

We substitute the expression for the current densities into Maxwell's equation

$$\nabla \times \mathbf{H} = \frac{4\pi}{c}\mathbf{j} + \frac{1}{c}\frac{\partial \mathbf{D}}{\partial t}, \tag{2}$$

after replacing the derivatives with respect to the coordinate in the direction z perpendicular to the layers by a finite difference and expressing the magnetic field in the y direction in terms of φ_n and $\mathbf{P}_n$:

$$H_y = \frac{c}{2d}\frac{\partial \varphi_n}{\partial x} - \frac{c}{d}(P_{n+1} - P_n),$$

where x is the coordinate in the direction of motion of the vortices.

In the displacement current, we allow only the component along the z axis, since because of the strong anisotropy the plasma frequency in a direction parallel to the layers, $\Omega_p = c/\lambda$, is much higher than the characteristic frequencies of the problem, which are close to the plasma frequency in the direction perpendicular to the layers, $\omega_p = c_z/\lambda_c$, where $c_z = c/\sqrt{\epsilon}$, ϵ is the dielectric constant along the z axis, and λ and $\lambda_c = c/\sqrt{8\pi d j_c}$ are the screening lengths of the magnetic field for screening by currents flowing along and across the layers, respectively. As a result, we obtain the equations

$$j_{\perp n}^{(s)}(\varphi_n) - \frac{c^2}{8\pi d}\frac{\partial^2 \varphi_n}{\partial x^2} + 2\lambda_c^2 \frac{\partial}{\partial x}(P_{n+1} - P_n) = -\frac{\lambda_c^2}{c^2}\frac{\partial}{\partial t}\left(\frac{4\pi\sigma_\perp}{\epsilon} + \frac{\partial}{\partial t}\right)\varphi_n, \tag{3}$$

$$\frac{c^2}{2d^2}\frac{\partial}{\partial x}(\varphi_n - \varphi_{n-1}) + \Omega_p^2 P_n - \frac{c^2}{d^2}(P_{n+1} + P_{n-1} - 2P_n) = -\frac{\partial}{\partial t}\left(4\pi\sigma_\parallel + \frac{\partial}{\partial t}\right)P_n. \tag{4}$$

Solving these equations, we find the electric and magnetic fields as functions of the coordinates and time.

The model phase dependence of the current (1) makes it possible to find the exact solution of Eqs. (3) and (4) by means of the Fourier transformation. Strictly speaking, it is necessary to take into account the curvature of the flux lines during the motion. However, we shall confine our attention below to the case when the displacement of the center of a vortex $x_0(y)$ along the x axis at distances $y \approx \lambda_c$ is small. A calculation of the deformation based on the balance equation for the forces exerted on a vortex by the transport current and the currents produced by the vortices themselves in fields $H \gg H_{c1}$ shows that the deformation can be neglected if

$$\frac{x_0(\lambda_c)}{\lambda_c} \approx \frac{\lambda}{\pi d\ \ln(\lambda/d)}\frac{j_{tr}H_{c1}}{j_c H} \ll 1. \tag{5}$$

We shall assume that H is much larger than H_{c1} and the condition (5) holds.

As a result, we obtain for a triangular lattice moving with velocity u

$$(\tilde{\omega}_p^2 - \omega^2 + i\omega\omega_r)\varphi - 2c^2 qKP/\epsilon = \Pi\,\delta(q - \omega/u), \tag{6}$$

$$-(c^2 qK/2d^2)\varphi + (\tilde{\Omega}_p^2 - \omega^2 + i\omega\Omega_r)P = 0. \tag{7}$$

Here $K=2\sin k/2$, $|k|<\pi$ is the wave number obtained as a result of performing a discrete Fourier transformation with respect to the layer number, $\tilde{\omega}_p^2=\omega_p^2(1+\lambda_c^2q^2)$, $\tilde{\Omega}_p^2=\Omega_p^2(1+\lambda^2K^2/d^2)$, $\omega_r=4\pi\sigma_\perp\epsilon$, $\Omega_r=4\pi\sigma_\parallel$, and finally

$$\Pi=4\pi^2(\omega_p^2/i\omega)\sum_{l,m}\exp[-i(l+m/2)qX-imkZ/d].$$

The solution of Eqs. (6) and (7) for the phase difference has the form

$$\varphi=\Pi(1+\lambda^2K^2/d^2)\,\delta(q-\omega/u)/D, \tag{8}$$

where D is the determinant of the system (6), (7). The zeros of D determine the spectrum of the characteristic oscillations – plasmons. At sufficiently high frequencies and low temperatures, for which the dielectric relaxation frequencies Re ω_r and Im Ω_r are small,

$$D=[(\omega_p^2-\omega^2)(1+\lambda^2K^2/d^2)+\omega_p^2\lambda_c^2q^2-i\omega[\omega_r(1+\lambda^2K^2/d^2)+\Omega_r(\omega_p^2-\omega^2+\omega_p^2\lambda_c^2q^2)/\Omega_p^2].$$

We shall illustrate the change in the character of the solution as a function of the frequency for the example of the components of the electric field $E_z=-i(\omega/2d)\varphi$. The slowly varying (along z) part of the field E_z produced by a single vortex at frequency $\omega=qu$ $(q=2\pi/X)$ has the form

$$E_z=\frac{\pi u\omega_p^2\exp(-z/\Lambda)}{2d\sqrt{(\omega_p^2-\omega^2-i\omega\omega_r)(\omega_p^2-\omega^2+\omega_p^2\lambda_c^2q^2-i\omega\omega_r)}},$$

$$\Lambda=\lambda\sqrt{\frac{\omega_p^2-\omega^2-i\omega\omega_r}{\omega_p^2-\omega^2+\omega_p^2\lambda_c^2q^2-i\omega\omega_r}}. \tag{9}$$

The total field is described by the sum of fields produced by all vortices. One can see that at low frequencies the decay length of the field is of the order of λ, and when the frequency exceeds the plasma frequency the real part of the argument of the exponential in Eq. (9) becomes small, i.e., in the region of plasma oscillations the decay length of the field increases rapidly and is determined by the damping of the plasmons.

To find a relation between the transport current j_{tr} and the velocity u of the vortex lattice, we premultiply Eq. (3) by $(c^2/\lambda_c^2)\partial\varphi_n/\partial x$ and Eq. (4) by $4\partial P_n/\partial x$, and then add these equations, integrate over x, and sum over all n. As a result, the terms on the left-hand side of the equality obtained form a combination which is a total derivative with respect to x, the integral of which reduces to $-2d^2\Sigma_nH_y^2|_{-\infty}^{+\infty}$. This expression determines the force acting on the lattice. It is proportional to the half-sum of the magnetic fields on different sides of the sample, i.e., the external magnetic field, and the difference of the magnetic fields, which by means of Eq. (2) can be expressed in terms of the transport current. We write the right-hand side of the equation with the aid of the Fourier transformation, substituting into it the solution of Eqs. (6) and (7). The result is

$$16\pi^2 d j_{tr} = \int dq\,dk\,u\,\omega_p^4 [\epsilon\omega_r (1+\lambda^2 K^2/d^2)^2$$

$$+\Omega_r \lambda^4 K^2 q^2/d^2)]/|D|^2 \sum_{l,m} e^{i(l+m/2)X+imkZ/d}. \tag{10}$$

Substituting into Eq. (10) the solution (6) and (7), we find the dependence on j_{tr} of the velocity of the vortices and hence of the average electric field $\overline{E} = 2\pi n_L u$ (where n_L is the density of vortices).

In the limit of low velocities of the lattice, $u \ll (d/\lambda)c$, the effect of the velocity u on the shape of the vortices can be neglected. In this case the IVC is described by Ohm's law with resistivity

$$\rho = \frac{1}{\sigma_\perp + \sigma_\parallel (\lambda/\lambda_c)^2} \frac{2 n_L d \lambda_J}{\pi}, \tag{11}$$

where $\lambda_J = d\lambda_c/\lambda$. The last factor in Eq. (11) describes the fraction of the superconductor volume occupied by the nonlinear region of the vortex. We can see an analogy with the Bardeen–Steven law, in which the area ξ^2 of the vortex core is replaced by the area $d\lambda_J$ of the nonlinear region of the Josephson vortex.

An analytical expression for the dependence of u on j_{tr} can also be obtained for the case of frequencies of the order of the plasma frequency and small damping of the plasmons:

$$j_{tr} = j_c \frac{\sinh b}{\cosh b - \cos a}, \quad a = \frac{X c_z}{\lambda_c u}, \quad b = \frac{\omega_r(\omega_p)}{2\omega_p} a.$$

The last factor in this formula describes oscillations which appear in the IVC as a result of the interference of plasmons emitted by different vortices. In the limit of high velocities, the IVC goes over to Ohm's law with a resistivity $\rho = 2\pi\sqrt{n_L d \lambda_j}/\sigma(\omega_p)$. The form of the IVC in the region of the plasma oscillations is sensitive to the magnitude and anisotropy of the quasiparticle conductivity. An increase in the conductivity results in stronger damping of the plasmons and suppression of the characteristic features. The regime of very weak damping is easily achievable with isotropic pairing, when the order parameter has no nodes and the quasiparticle density at low temperatures becomes exponentially small. In the case of d pairing the damping is greater and the peaks in the IVC are smaller. Figure 1 shows the function $j_{tr}(u)$, found numerically under the assumption that the real part of the quasiparticle conductivity is described by the equations from Ref. 10 and falls off as $1/\omega^2$ at frequencies greater than the reciprocal of the momentum relaxation time. We note that the condition (5) for neglecting the deformation of the vortices is difficult to satisfy at high currents in regions near the maxima, so that finding the shape of the IVC near the tops of the peaks requires a more accurate calculation that takes into account the curvature of the flux lines during the motion.

Therefore, regions of negative differential conductivity, where a uniform flow of the lattice of Josephson vortices is unstable, appear on the IVC in the region of plasma oscillations. These sections alternate with regions of stability. Uniform motion is stable at high voltages.

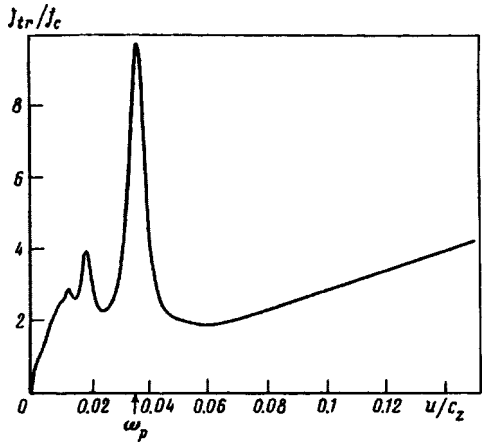

FIG. 1. Typical curve of the transport current versus the velocity of vortices in a field $H=20H_{c1}$.

The excitation of plasma oscillations is associated with the generation of electromagnetic radiation. Let us find the radiation energy flux along the x axis at frequency $\omega_N=2\pi uN/X$, where N is the number of the harmonic. For this, we calculate the Poynting vector, using expressions for the electric and magnetic fields that can be easily found with the aid of Eq. (8):

$$S=\int_{-\pi}^{\pi}\frac{uc^2\omega_p^4(1+\lambda^2k^2/d^2)}{16\lambda ZdX^2|D(\omega=\omega_N)|^2}\sum_m e^{imZk/d}dk.$$

It is obvious that the energy flux grows rapidly at resonance frequencies at which $|D|$ is small. For a triangular lattice the odd harmonics of the radiation contain peaks near the plasma frequency and the even harmonics also contain peaks at velocities close to the velocity of light c_z in the medium, which plays the role of the Swihart velocity in a tunnel junction. The latter peaks correspond to Cherenkov radiation. Figure 2 shows the function $S(u)$ for the first harmonic, where the energy flux is expressed in the units $S_0=\hbar^2c^2\omega_p/(16e^2\lambda^2\lambda_c)$. For values $\epsilon=25$, $\lambda=0.2$ μm, and $\lambda_c=60$ μm, characteristic for BSCCO, and $S_0\sim 10$ W/cm^2. The form of the curve and the sizes of the peaks depend strongly on the magnitude and anisotropy of the conductivity. The lattice velocities corresponding to the peaks in the radiation are not necessarily correlated with the peaks in the IVC, so that it is possible to observe radiation peaks at frequencies of the order of plasma frequencies at voltages in the regions of stable uniform motion of the vortex lattice.

The peak in the energy flux with $u>c_z$ is much higher than the peaks near the plasma frequency. It is described approximately by the expression

$$S=\frac{S_0h^2}{4\pi^2\{[1+hN^2(1-u^2/c_z^2)]^2+hN^2\omega_r^2(u=c_z)\}},$$

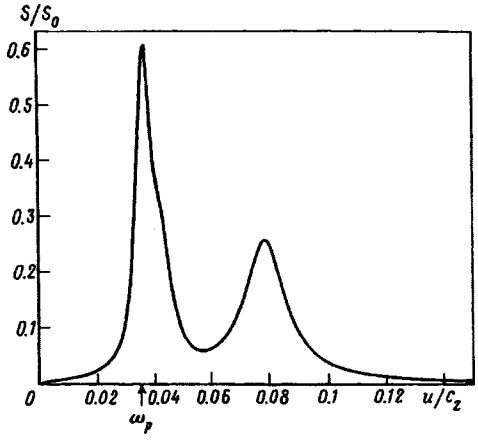

FIG. 2. Typical curve of the radiation energy flux at the frequency of the first harmonic versus the velocity of the vortices, $H=20H_{c1}$.

where $h=4\pi^2\lambda\lambda_c n_L$. We note that the frequencies corresponding to a lattice moving with velocity close to c_z fall into the frequency range below the amplitude of the order parameter only in sufficiently weak magnetic fields, where the lattice period X is comparable to λ_c. As the field increases, the frequency will reach Δ, which will lead to stronger damping as a result of pair breaking.

We also note that the effects which we have studied above refer to higher frequencies and voltages than those at which the experimental investigations of Josephson vortices are usually conducted, as, for example, in the recent work Ref. 13 where non-Josephson radiation was observed during motion of vortices in BSCCO. Since we are studying a uniform motion of a vortex lattice in an infinite crystal, such radiation does not occur in our formulation of the problem.

This work was supported by Grant 96053 from the Russian Program ''Superconductivity.''

[a)]e-mail: Art@mail.cplire.ru

---

[1]K. Tamasaku, Y. Nakomura, and S. Ushida, Phys. Rev. Lett. **69**, 1455 (1992).
[2]O. K. C. Tsui, N. P. Ong, Y. Matsuda *et al.*, Phys. Rev. Lett. **73**, 724 (1994).
[3]T. Mishonov, Phys. Rev. B **44**, 12033 (1991).
[4]S. N. Artemenko and A. G. Kobel'kov, JETP Lett. **58**, 445 (1993).
[5]M. Tachiki, T. Koyama, and S. Takahashy, Phys. Rev. B **50**, 7065 (1994).
[6]L. N. Bulaevskii, M. Zamora, D. Baeriswyl *et al.*, Phys. Rev. B **50**, 12831 (1994).
[7]A. F. Volkov, Phys. Lett. A **138**, 213 (1989).
[8]E. B. Sonin, Phys. Rev. Lett. **79**, 3732 (1997).
[9]S. N. Artemenko and A. G. Kobel'kov, Phys. Rev. Lett. **78**, 3551 (1997).
[10]S. N. Artemenko and A. G. Kobel'kov, JETP Lett. **65**, 331 (1997); Phys. Rev. B **55**, 9094 (1997).
[11]S. Aubry and P. J. Le Daeron, Physica D **7**, 240 (1983).
[12]A. F. Volkov, Physica C **183**, 177 (1991).
[13]G. Hechtfischer, R. Kleiner, A. V. Ustinov *et al.*, Phys. Rev. Lett. **79**, 1365 (1997).

Translated by M. E. Alferieff

Interaction of optical phonons with anisotropic imperfections

L. A. Falkovsky

Landau Institute of Theoretical Physics, Russian Academy of Sciences, 117334 Moscow, Russia; Groupe d'Etudes des Semiconducteurs, UM2-CNRS, 34095 Montpellier, France

(Submitted 13 November 1997)
Pis'ma Zh. Éksp. Teor. Fiz. **66**, No. 12, 817–822 (25 December 1997)

Inelastic (Raman) light scattering by phonons interacting with anisotropic imperfections is investigated. Three different kind of disorder-induced defects (point, linear and planar) have been considered. The optical phonon width and line shape are found to depend importantly on the dimension of the imperfections. There is a close correspondence between the scale of the imperfection and the phonon line shape observed in the Raman scattering experiments. The dependence of the phonon frequency shift and width on the defect concentrations is calculated, and the critical concentrations at which the optical phonon can no longer be observed are determined. © *1997 American Institute of Physics.* [S0021-3640(97)01324-8]

PACS numbers: 78.30.Ly, 61.72.−y, 63.20.Dj

1. Many problems encountered in disorder systems have well-known theoretical explanations. In particular, the dynamics of impurities in crystals has been described in Refs. 1 and 2, where both the density of states and frequency of local vibrations were specially considered. The influence of impurities on the vibrational Raman scattering has been examined in Refs. 3 and 4, but so far there has been no relevant interpretation of the optical phonon interaction with anisotropic imperfections. This is done in the present work. Let us emphasize the peculiarities of this phenomenon.

First, the different type of imperfections (e.g., impurities, vacancies, dislocations, crystallite boundaries) have different spatial structure. Dislocations are an example of line defects. In the case of ion implantation, the defects are certainly more elongated in the direction normal to the surface than in the tangential direction. Finally, the boundaries of crystallites or pores are plane defects. In this work, we focus on the interaction of optical phonons with three main kind of disorder-induced defects: *(i)* point defects, *(ii)* line defects, and *(iii)* a random set of plane defects. Both the optical phonon width and line shape are found to depend importantly on the dimension of the imperfections.

Second, because the optical phonons are usually observed in inelastic (Raman) light scattering, the momentum transfer k (which is of the order of the incident light momentum $\omega^{(i)}/c$) is much smaller than the cutoff value $k^{(w)}=\sqrt{\omega_0\Gamma}/s$ determined by the phonon width $\Gamma\simeq 5\ \mathrm{cm}^{-1}\simeq 10^{12}\ \mathrm{s}^{-1}$, the frequency $\omega_0\simeq 5\times 10^2\ \mathrm{cm}^{-1}\simeq 10^{14}\ \mathrm{s}^{-1}$ and the dispersion parameter $s\simeq 10^6$ cm/s which is of the order of the sound velocity. Therefore, the condition $k\ll k^{(w)}$ holds and we have to calculate the width in the vicinity of an

extremum of the branch, taking into account self-consistently the phonon width and shift which result from the interaction of phonons with the disorder. The size $1/k^{(w)}$ is moderately large in the atomic scale $a=\pi s/\omega_0$: $1/k^{(w)}a=\sqrt{\omega_0/\Gamma}/\pi$ and this is the existence of this large (on the microscopic scale) parameter $1/k^{(w)}$ that provides justification for the present theory.

Third, since the optical phonons are bosons, they can be excited or emitted singly in the process of interaction with light. Then the Raman cross section of the first order is determined by the phonon Green function averaged over the distribution of the imperfections. Therefore, a simple theory can be advanced using Dyson's equation with a squared phonon–imperfection potential as transition probability. A similar technique has been recently applied to the problem of strain relaxation near semiconductors heterointerfaces,[5] except that averaging over the distribution of imperfections can be performed now in an explicit form. We obtain the phonon shift and width (i.e., the phonon self-energy) in the case of the various imperfection geometry. The phonon line shape i.e., the frequency dependence of the inelastic light scattering cross section (which is proportional to the imaginary part of the averaged Green function) becomes asymmetric and conditioned by the parameter $r_0k^{(w)}=\pi r_0/a\sqrt{\omega_0/\Gamma}\simeq 0.1r_0/a$ for the set of values listed before, where r_0 is the domain size where phonons can be scattered by the imperfection. Before closing this series of introductory remarks, it may be be useful to notice that this asymmetry has no connection to the well known Fano resonance in conducting systems. Indeed, the Fano resonance results from a contribution of the electron loop in the photon–phonon vertex while, in our case, the asymmetric phonon line shape originates from the phonon density of final states when one considers the scattering of phonons by the imperfections.

2. The inelastic light scattering cross section is determined by the Green function of optical phonons $D_{ij}(\mathbf{r},\mathbf{r}',\omega)$ which obey the equation

$$(H-i\omega\Gamma^{(\mathrm{int})}+V(\mathbf{r})-\omega^2)D(\mathbf{r},\mathbf{r}',\omega)=\delta(\mathbf{r}-\mathbf{r}'),$$

where the matrix $H_{ij}=\omega_0^2\delta_{ij}+\mu_{ijlm}\partial^2/\partial x_l\partial x_m$ represents the long-wave expansion of the dynamical matrix near a extremum of the branch. The damping parameter $\Gamma^{(\mathrm{int})}$ describes the intrinsic phonon width caused by the phonon–phonon and electron–optical phonon interactions,[6] and the matrix

$$V_{ij}(\mathbf{r})=\sum_n v_{ij}(\mathbf{r}-\mathbf{r}_n) \tag{1}$$

is the interaction with imperfections located at points $\mathbf{r}_n$. In the case of a substitutional defect of mass m_v instead of m, the interaction may be simply estimated as $v_{ij}(\mathbf{r}-\mathbf{r}_n)=\delta_{ij}\delta(\mathbf{r}-\mathbf{r}_n)\omega_0^2a^3(m-m_v)/M$, where M and a^3 are the mass and volume of the lattice cell. For a line defect, $(\mathbf{r}-\mathbf{r}_n)$ is a two-dimensional vector. It becomes one-dimensional for a plane defect. The phonon degeneracy has been taken into account by using the subscript i. For instance, in a cubic crystal, there are three optical phonons at the Γ point with a threefold degenerate frequency $(i=1,2,3)$. The long-range Coulomb forces split this degeneracy in such a way that the LO phonon has a higher frequency than the twofold degenerate TO phonon.

The Green function has to be averaged over defects distributed randomly. Using the diagram technique and summing diagrams with the averages $\langle V_{ij}\rangle$ and $\langle \delta V_{ij}(\mathbf{r})\,\delta V_{lm}(\mathbf{r}_1)\rangle = W_{ijlm}(\mathbf{r}-\mathbf{r}')$, where $\delta V = V - \langle V\rangle$, we obtain the Dyson equation for the averaged Green function. Near the branch maximum, we seek its solution

$$D_{jj}^{-1}(\mathbf{k},\omega) = \omega_j^2(\mathbf{k},\omega) - s_j^2 k^2 - i\omega\Gamma_j(\mathbf{k},\omega) - \omega^2 \tag{2}$$

and arrive at a system of coupled integral equations

$$\omega_j^2(\mathbf{k},\omega) - \omega_j^2 - i\omega(\Gamma_j(\mathbf{k},\omega) - \Gamma_j^{(\mathrm{int})}) - \langle V_{jj}\rangle$$
$$= -\sum_m \int \frac{d^3k_1}{(2\pi)^3} \frac{W_{jmmj}(\mathbf{k}_1-\mathbf{k})}{\omega_m^2(\mathbf{k}_1,\omega) - s^2k_1^2 - i\omega\Gamma_m(\mathbf{k}_1,\omega) - \omega^2}, \tag{3}$$

where the unknown functions are $\Gamma_j(\mathbf{k},\omega)$ and $\omega_j(\mathbf{k},\omega)$.

The conditions of validity for Dyson's equation (3) should be outlined here. The line shape on the wings ($|\omega-\omega_0| > \Gamma$) can be obtained using the perturbation theory (the Born approximation) when $\omega_m^2(\mathbf{k}_1,\omega) - i\omega\Gamma_m(\mathbf{k}_1,\omega)$ is substituted in the right-hand side (i.e., in the phonon self-energy) for its unperturbed value $\omega_0^2 - i\omega\Gamma_m^{(\mathrm{int})}$. At the center of the line, the diagrams with intersections of the correlator lines make a contribution of the order of the leading diagram, and a more sophisticated theory is needed.

The correlation function $W_{jmmj}(\mathbf{k}_1-\mathbf{k})$ has the meaning of a transition probability $(j,\mathbf{k}) \to (m,\mathbf{k}_1)$. In order to find the averages $\langle V\rangle$ and $\langle \delta V(\mathbf{r})\,\delta V(\mathbf{r}')\rangle$, let us write the Fourier transform in Eq. (1) for the point defects

$$V_{ij}(\mathbf{r}) = \sum_n \int \frac{d^3q}{(2\pi)^3} v_{ij}(\mathbf{q}) e^{i\mathbf{q}(\mathbf{r}-\mathbf{r}_n)}. \tag{4}$$

Averaging, i.e., performing an integration over all positions of the defects in a large (on the microscopic scale) volume V_0 we get immediately $\langle V_{ij}(\mathbf{r})\rangle = n_v v_{ij}(\mathbf{q}=0)$, where n_v is the volume concentration of defects.

The contributions to the two-point correlation function come from the terms which, in the product of two sums (4), involve the same defect:

$$\langle \delta V_{im}(\mathbf{r})\,\delta V_{lj}(\mathbf{r}')\rangle = n_v \int \frac{d^3q}{(2\pi)^3} v_{im}(\mathbf{q}) v_{lj}(\mathbf{q}) e^{i\mathbf{q}(\mathbf{r}-\mathbf{r}')}. \tag{5}$$

Equation (5) gives the Fourier transform $W_{imlj}(\mathbf{q})$ of the potential–potential correlation function for point defects. For line defects we obtain $W_{imlj}(\mathbf{q}) = 2\pi n_s \delta(q_z) \times v_{im}(\mathbf{q}_\perp) v_{lj}(\mathbf{q}_\perp)$, where $\mathbf{q}_\perp$ is the two-dimensional vector in the plane perpendicular to the set of line imperfections and n_s is their concentration per unit area. A similar expression (with a two-dimensional δ function) can be found for plane imperfections with concentration $n_{/\!/}$ per unit length.

3. For simplicity, let us consider only the case of a phonon singlet. We will discuss the interband phonon transitions in the conclusion. In this case the subscripts in D_{ij} and V_{ij} take only one value ($j=1$) and we will omit them. The poles of the phonon Green function give the phonon dispersion law. In the absence of imperfections, using (2) and

(3) we get near the maximum of the branch $\omega^2(\mathbf{k})=\omega_0^2-s^2k^2-i\omega_0\Gamma^{(\mathrm{int})}$, where the parameter s depends on the $\mathbf{k}$-direction. This is not essential in what follows.

One point should be noticed. When applied to Raman scattering, the momentum $\mathbf{k}$ and frequency ω in Eqs. (3) have the meaning of the momentum and frequency transfers from the light. Then the values $k_1\leqslant k^{(w)}=\sqrt{\omega_0\Gamma}/s$ are important in the denominator of Eq. (3) if one is interested in a neighborhood $|\omega_0-\omega|\simeq\Gamma$ of the phonon frequency ω_0. The size $1/k^{(w)}$ is large on the atomic scale $a=\pi s/\omega_0$: $1/k^{(w)}=a\sqrt{\omega_0/\Gamma}/\pi\simeq 10a$. On the other hand, the phonon momentum transfer $(\mathbf{k}_1-\mathbf{k})$ in the interaction with an imperfection is determined by the domain size r_0 in which the imperfection relaxes. The two values $k^{(w)}$ and $1/r_0$ may be of the same magnitude, but they are much larger than the small momentum transfer $k\simeq\omega^{(i)}/c$ from the incident light. Then $\mathbf{k}$ can be omitted in the integrand, i.e., the unknown functions $\omega_1(\mathbf{k},\omega)$ and $\Gamma(\mathbf{k},\omega)$ can be regarded as $\mathbf{k}$-independent. But these functions depend essentially on ω because of the square root singularity of the phonon density of states at the extremum of branches. This dependence is responsible for the non-Lorentzian shape of the phonon mode (of course, the asymmetric broadening and line shift are much more pronounced for the short-range disorder $r_0k^{(w)}\leqslant 1$). Finally, if we put (for the correlation function only) the Fourier component $v(q)=v(q=0)$ in the region $q<r_0^{-1}$ and equal to zero elsewhere, all the integrals can be done analytically, and one obtains a system of coupled algebraic equations for $\Gamma(\omega)$ and $\omega_1(\omega)$.

Let us now present the results. We will denote the phonon self-energy, i.e., the right-hand side of Eq. (3), by $\Sigma(\omega)$. Then our main equation will take the form

$$\omega_1^2(\omega)-\omega_0^2-i\omega(\Gamma(\omega)-\Gamma^{(\mathrm{int})})-\langle V\rangle=\Sigma(\omega). \tag{6}$$

We see that the linear term $\langle V\rangle$ gives only *uniform* shift for the squared phonon frequency $\omega_1^{(\mathrm{un})2}=\omega_0^2+\langle V\rangle$ which is always linear in the concentration of defects, but can have an arbitrary sign. The additional *inhomogeneous* shift and broadening result from the bilinear (with respect to the imperfection potential) term Σ. To find them, we have to solve Eq. (6).

i. Point imperfections. The imaginary and real parts of (6) with

$$\Sigma(\omega)=A\left(2b-(a_1-ia_2)\left(\frac{1}{2}\log\frac{x_1^2+1}{x_2^2+1}+i\ \arctan x_1+i\ \arctan x_2\right)\right) \tag{7}$$

give a system of two coupled equations for the unknown functions $\omega_1(\omega)$ and $\Gamma(\omega)$, where $x_1=(b+a_1)/a_2$, $x_2=(b-a_1)/a_2$, $a_1=(\omega_1^2(\omega)-\omega^2+\Omega^2(\omega))^{1/2}$, $a_2=(-\omega_1^2(\omega)+\omega^2+\Omega^2(\omega))^{1/2}\mathrm{sign}(\omega)$, $\Omega^4(\omega)=(\omega_1^2(\omega)-\omega^2)^2+\omega^2\Gamma^2(\omega)$, $b=\sqrt{2}s/r_0$, and $A=n_v v^2(q=0)/4\sqrt{2}\pi^2 s^3$.

Let us write $v(q=0)=gr_0^3\omega_0^2$ for estimates (where $g\simeq 1$ if the force constants change around imperfections). Then the linear term $\langle V\rangle$ in (6) gives $gn_v r_0^3\omega_0^2/2$, and the second-order term in (7) gives $A=g^2n_v r_0^3\omega_0(r_0\omega_0/s)^3/4\sqrt{2}\pi^2$. For the above-mentioned example of a substitutional defect, the Fourier component $v(q)=\omega_0^2a^3(m-m_v)/M$, and we need to cut off the real part of integral (3) at $1/a$ instead of $1/r_0$.

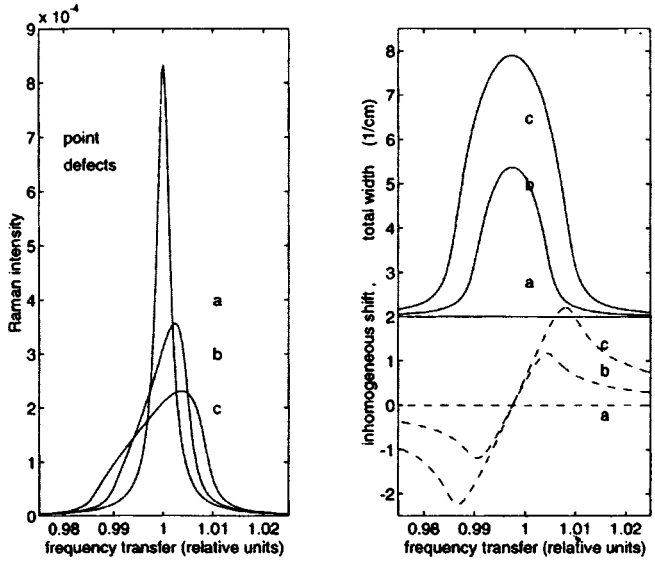

FIG. 1. Theoretical Raman intensity (imaginary part of the phonon Green function, the left panel), phonon width (top of the right panel) and shift (dotted lines) plotted as function of the frequency transfer in the case of point defects with a potential of the small radius $r_0=3.5a$ in atomic units a. The intrinsic phonon width is taken 2 cm^{-1}, but three different values of the dimensionless interaction constant $A_d=A/\omega_0$ have been used in Eq. (7) and the corresponding total widths Γ (cm^{-1}) obtained at the line centers: (a) perfect crystal, $A_d=0$, $\Gamma=2$ (b) $A_d=0.075$, $\Gamma=4.84$, (c) $A_d=0.187$, $\Gamma=7.40$.

The numerical solution to the coupled system (6)–(7) as a function of the frequency transfer, together with the Raman cross section which is proportional to Im $D(\omega)$, is shown in Fig. 1 for several values of the interaction constant A and $r_0=3.5a$. One find clearly that the line shape is asymmetric. The resonance curve drops more slowly on the low-frequency side of the peak and, as we have said, this comes about simply because the density of phonon states increases below the maximum. The center of the line (renormalized phonon frequency) is determined by the equation $\omega_1(\omega)=\omega$ (see Eq. (2) with $k=0$). Using Eqs. (6) and (7) at the center of the line, one can easily find the phonon width Γ and the defect-induced shift $(\omega_1-\omega_0)$.

ii. Line imperfections. In this case,

$$\Sigma(\omega)=B\left(\frac{1}{2}\log\frac{(s^2/r_0^2+\omega^2-\omega_1^2(\omega))^2+\omega^2\Gamma^2(\omega)}{(\omega^2-\omega_1^2(\omega))^2+\omega^2\Gamma^2(\omega)}-i\arctan\frac{\omega_1^2(\omega)-\omega^2}{\omega\Gamma(\omega)}\right.$$
$$\left.-i\arctan\frac{s^2/r_0^2-\omega_1^2(\omega)+\omega^2}{\omega\Gamma(\omega)}\right), \tag{8}$$

where $B=n_s v^2(q_\perp=0)/4\pi s^2$ and $v(q_\perp=0)=gr_0^2\omega_0^2$.

The resonance line appears wider than it was in case (*i*) because of the more important frequency dependence of the line shift.

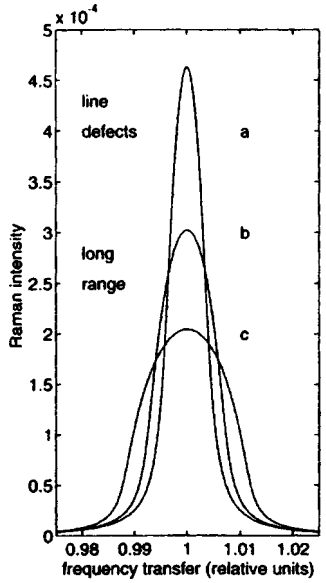

FIG. 2. Same as Fig. 1 but for line defects of large radius $r_0=20a$ for three values of the interaction constant B_d: (a) $B_d=0.063$, $\Gamma=3.58$, (b) $B_d=0.21$, $\Gamma=5.5$, (c) $B_d=0.55$, $\Gamma=8.1$.

iii. Plane imperfections. We obtain

$$\Sigma(\omega)=C\left(\frac{1}{2}\log\frac{x_1^2+1}{x_2^2+1}+\arctan x_1+i\ \arctan x_2\right)\Big/\ (-a_1+ia_2), \tag{9}$$

where the notation is the same as in (7); $C=n_{/}v^2(q_z=0)/\sqrt{2}\pi s$, the one-dimensional Fourier component $v(q_z=0)=g\omega_0^2 r_0$, and $n_{/}$ is the lineal concentration of scattering planes (density per unit length). In other words $(n_{/}a)^{-1}$ is the average crystallite or pore size measured in atomic units.

It is interesting to remark that one obtains the same frequency dependence of the Raman cross section in the limiting case of the very large potential radius $r_0k^{(w)}\gg 1$ for all dimensions. This case describes simply the small-angle scattering of phonons by imperfections and, as a consequence, the phonon cannot ''see'' really the geometry of the imperfections. As an example, we show the case of the line defects in Fig. 2 for long-range disorder. Although our final results have been written for a single phonon mode, the basic Dyson equation (3) may be applied to a degenerate phonon. In this case, the phonon scattering by the anisotropic imperfections implies both damping and splitting of the degenerate phonon mode.

4. In Fig. 3 the inhomogeneous shift (the homogeneous shift is not included) and width are shown as functions of the defect concentration for different dimensions of the imperfections. They would be linear functions if the standard perturbation theory were used. For imperfections on an atomic scale $r_0\sim a$, one can obtain from Eqs. (7)–(9) the

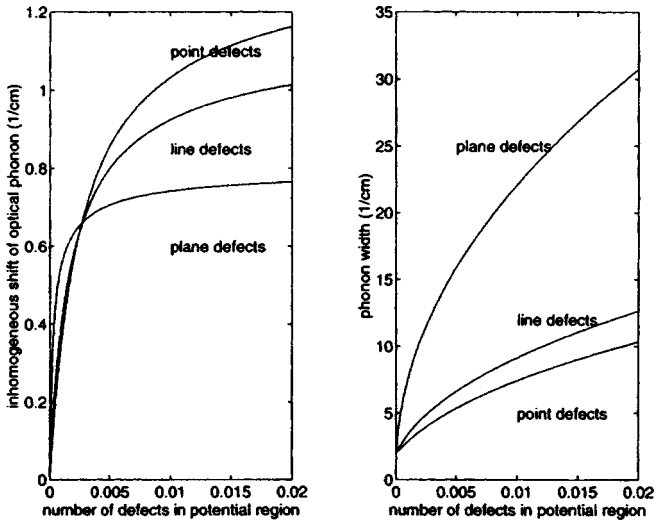

FIG. 3. Dependence of the inhomogeneous phonon shift and width (at the line centers) on the imperfection concentration for three kinds of defects. The potential radius $r_0=3.5a$ and the phonon–imperfection coupling $g=0.5$ are taken for all cases. The concentrations are given by the dimensionless variables $n_v r_0^3$, $n_s r_0^2$, $n_{/} r_0$ for the point, line, and plane imperfections, respectively. The solid curves are the solutions of equations (6)–(9).

rough estimates $\Gamma-\Gamma^{(\mathrm{int})}=g^2 n_v a^3(\omega_0\Gamma)^{1/2}$ for the point defects, $\Gamma-\Gamma^{(\mathrm{int})}=g^2 n_s a^2\omega_0$ for the line defects, and $\Gamma-\Gamma^{(\mathrm{int})}=g^2 n_{/} a\,\omega_0(\omega_0/\Gamma)^{1/2}$ for the plane defects, where $g\simeq 1$ is a dimensionless coupling of phonons with the imperfections.

The fact that the optical phonons are not visible in the Raman scattering if $\Gamma/\omega_0>.01$ (roughly) gives that defines the critical concentrations of the point and line defects as $n_v a^3 g^2\simeq(\Gamma/\omega_0)^{1/2}\simeq .1$ and $n_s a^2 g^2\simeq\Gamma/\omega_0\simeq .01$, respectively, and the critical crystallite size $(n_{/} g^2)^{-1}\sim a(\omega/\Gamma)^{3/2}\simeq 10^3 a$ above which the Raman lines are no longer observed.

Our results also show that there is a definite correspondence between the imperfection scale r_0 and the phonon line shape observed in the Raman scattering. The crossover value r_0^{-1} for the potential radius is determined by the phonon width $k^{(w)}=\sqrt{\Gamma\omega_0}/s$. In the case of the short-range imperfection potential $k^{(w)}r_0\leqslant 1$, the phonon line shape is asymmetric due to the influence of the phonon density of state (see Fig. 1). For the imperfections of large radius $k^{(w)}r_0>1$, the influence of phonon–defect scattering results in a symmetric but non-Lorentzian line shape (see Fig. 2).

This paper was motivated by discussions with J. Camassel of his experiments on interfaces and ion implantation. It is my pleasure to thank him for comments and ideas. I am also grateful to V. Fateev for discussions and comments. This work was supported in the framework of INTAS program 0101–CT93–0023 and also by Russian Fund for Fundamental Research (Grant No 97-02-16044).

[1] D. W. Taylor, in *Dynamical Properties of Solids*, edited by G. K. Horton and A. A. Maradudin (North–Holland, 1975), Vol. 2, pp. 285–384.
[2] A. S. Barker and A. J. Sievers, Rev. Mod. Phys. **47** Suppl. 2, S1 (1975).
[3] M. V. Klein, in *Dynamical Properties of Solids*, edited by G. K. Horton and A. A. Maradudin (North-Holland, Amsterdam, 1990), Vol. 6, pp. 65–127.
[4] M. Cardona and I. P. Ipatova, in *Elementary Excitations in Solids*, edited by J. L. Birman, C. Sebenne, and R. F. Wallis (Elsevier Science Publishers B. V., 1992), Chapter 13, pp. 264–266.
[5] L. A. Falkovsky, J. M. Bluet, and J. Camassel, Phys. Rev. B **55**, R14697 (1997).
[6] L. A. Falkovsky and E. G. Mishchenko, Phys. Rev. B **51**, 7239 (1995).

Published in English in the original Russian journal. Edited by Steve Torstveit.

Thermal conductivity of the spin-Peierls compound $CuGeO_3$

A. M. Vasil'ev, M. I. Kaganov, and V. V. Pryadun[a)]
Department of Physics, M. V. Lomonosov Moscow State University, 119899 Moscow, Russia

G. Dhalenne and A. Revcolevschi
Laboratoire de Chimie des Solides, Universite Paris-Sud, 91405 Orsay Cedex, France

(Submitted 17 July 1997; resubmitted 18 November 1997)
Pis'ma Zh. Éksp. Teor. Fiz. **66,** No. 12, 823–826 (25 December 1997)

The thermal conductivity of the pure and zinc-doped spin-Peierls compound $CuGeO_3$ is investigated for the first time. Characteristic features reflecting the changes in the phonon spectrum of the crystals are observed in the $k(T)$ curves at a transition into the dimerized state in $CuGeO_3$ at $T_{sp}=14.2$ K and in $Cu_{0.98}Zn_{0.02}GeO_3$ at $T_{sp}=10.6$ K. Near the spin-Peierls transition temperature T_{sp} the thermal conductivity of $Cu_{0.98}Zn_{0.02}GeO_3$ ($k=3$ W/m·K) is much less than the thermal conductivity of $CuGeO_3$ ($k=21.5$ W/m·K). © *1997 American Institute of Physics.* [S0021-3640(97)01424-2]

PACS numbers: 72.20.−i, 72.80.Sk, 75.80.+q

Copper germanate $CuGeO_3$ is currently one of the most popular objects of investigation in solid-state physics. This is due to the discovery of a spin-Peierls transition in this inorganic compound.[1] Previously, a structural transition due to magnetoelastic interaction in quasi-one-dimensional chains of half-integer spins had been observed only in some organometallic compounds.[2–4] In the orthorhombic structure of $CuGeO_3$ the magnetic-moment carriers with spin $S=1/2$ are Cu^{2+} ions, forming chains of copper–oxygen octahedra along the c axis. Along the a and b axes these chains are separated from one another by nonmagnetic chains of germanium–oxygen tetrahedra. The antiferromagnetic exchange interaction in a chain is estimated to be $J_c=120$ K, and the hierarchy of exchange integrals along the principal crystallographic axes is $J_a=0.1\cdot J_b=0.01\cdot J_c$ (Ref. 5). At $T_{sp}=14.3$ K the periods of the crystal lattice along the a and c axes double, and the Cu^{2+} ions are shifted in pairs toward one another. The dimers formed do not possess a magnetic moment, and the paramagnetic susceptibility of $CuGeO_3$ rapidly decreases with temperature in all crystallographic directions. In the absence of a constant magnetic field, the spin-Peierls transition is a second-order phase transition, accompanied by sharp anomalies of the specific heat[6] and elastic moduli.[7] The introduction of a small quantity of impurities which break the magnetic chains results in a rapid decrease of the spin-Peierls transition temperature. This effect has been investigated in greatest detail for the system $Cu_{1-x}Zn_xGeO_3$ (Ref. 8).

In contrast to the thermodynamic properties, the kinetic characteristics of $CuGeO_3$ have been little studied. It is shown only in Ref. 7 that the damping (like the velocity) of

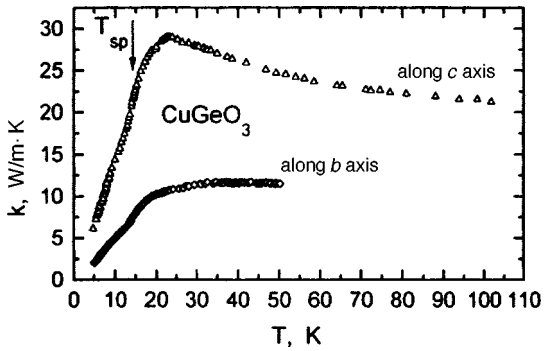

FIG. 1. Temperature dependences of the thermal conductivity of $CuGeO_3$ along the crystallographic directions b and c.

sound exhibits an anomaly near the spin-Peierls transition. In the present letter we report the results of an investigation of the thermal conductivity of copper germanate. The thermal conductivity k of $CuGeO_3$ and $Cu_{0.98}Zn_{0.02}GeO_3$ single crystals grown from melt by the floating-zone method was measured by the stationary heat flux method.[9] The dimensions of the $CuGeO_3$ sample in the a, b, and c directions were equal to 0.24, 0.86, and 4 mm and the dimensions of the $Cu_{0.98}Zn_{0.02}GeO_3$ sample were equal to 0.05, 0.8, and 3 mm. The thermal conductivity measurements were performed along the crystallographic directions b and c in the temperature interval 5–100 K.

The temperature dependences of the thermal conductivity in pure $CuGeO_3$ are shown in Fig.1. Dependences of this type are characteristic for dielectrics, where heat is transferred by phonons. As the temperature decreases, the thermal conductivity along the c axis at first increases with increasing carrier mean free path, reaches its maximum value $k=29$ W/m·K at $T=23.3$ K, and then decreases as a result of the decrease in the number of phonons. The thermal conductivity along the b axis does not exhibit a distinct phonon maximum, and its absolute magnitude is much smaller. From Fig. 2, where measurements of the thermal conductivity along the dimerization axis c in pure and doped samples at

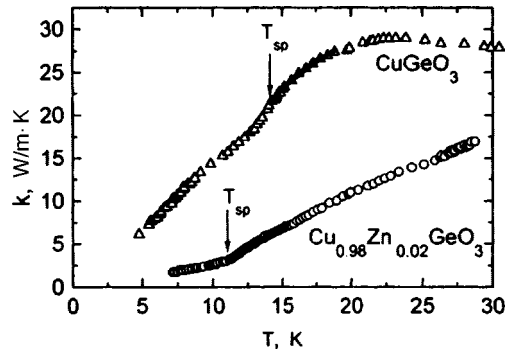

FIG. 2. Temperature dependences of the thermal conductivity of $CuGeO_3$ and $Cu_{0.98}Zn_{0.02}GeO_3$ near the spin-Peierls transition along the c axis. The lines are drawn according to the relation $k\sim(T-T_{sp})^{\alpha}$.

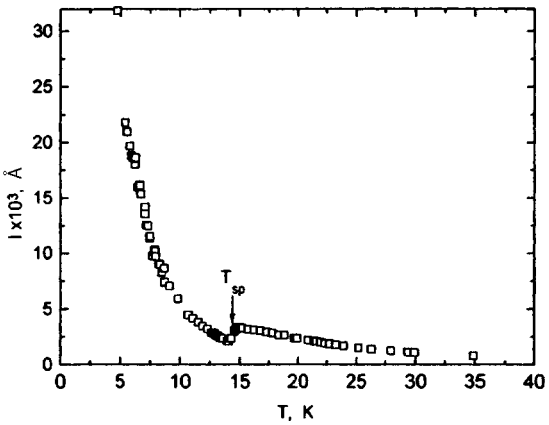

FIG. 3. Temperature dependence of the phonon mean free path in $CuGeO_3$ along the c axis.

low temperatures are displayed on an enlarged scale, one can see that features are observed in the curves $k(T)$ near the spin-Peierls transition. The critical temperatures were determined from the maximum of the derivative dk/dT near the spin-Peierls transition. The transition temperatures, established in this manner, into the dimerized state in $CuGeO_3$ ($T_{sp}=14.2$ K) and $Cu_{0.98}Zn_{0.02}GeO_3$ ($T_{sp}=10.6$ K) are in good agreement with the results of other measurements.[1,6–8] The thermal conductivity of the pure sample $k=21.5$ W/m·K near the spin-Peierls transition is much higher than the thermal conductivity of the doped sample $k=3$ W/m·K. This is due to the presence of a large number of defects in the doped sample.

At high temperatures the thermal conductivity of dielectrics is due mainly to phonon–phonon interactions accompanied by umklapp processes. This causes the thermal conductivity to decrease as $k\sim T^{-1}$ for $T>\Theta$, where Θ is the Debye temperature. The Debye temperature for $CuGeO_3$ was determined in Ref. 6 to be $\Theta=360$ K. At low temperatures $T<\Theta$ collisions of long-wavelength phonons do not lead to umklapp processes, and the phonon mean free path l is determined by scattering on defects. When l is comparable to the dimensions of the sample, the thermal conductivity k stops increasing and its behavior is determined by the specific heat C.

It can be conjectured that the maximum in the function $k(T)$ for $CuGeO_3$ is determined by phonon scattering by the surface. This conjecture, however, is at variance with the estimate of the phonon mean free path. From data on the thermal conductivity k, the specific heat C,[6] and the speed of sound v,[7] the temperature dependence of the phonon mean free path l can be determined using the gas-kinetic relation $k=(1/3)Cvl$. It is shown in Fig. 3. One can see that the maximum in the temperature dependence $k(T)$ at $T=23.3$ K is observed for carrier mean free paths much smaller than the geometric dimensions of the sample. This makes it impossible to attribute this feature to scattering of phonons by the boundary of the crystal. The most likely cause of the limitation on the phonon mean free path and hence on the thermal conductivity seems to be scattering by planar defects, examples of which are, cleavage planes in the crystal. We note that

$CuGeO_3$ crystals, being layered compounds, easily split into plates with thicknesses of the order of microns.

The minimum in the dependence $l(T)$ near the spin-Peierls transition temperature in $CuGeO_3$ is due mainly to a jump in the specific heat $\Delta C_p = 7.8$ J/kg·K;[6] the change in the velocity of longitudinal sound along the c axis is small at T_{sp}: $\Delta v/v = 10^{-3}$ (Ref. 7).

The dips observed in the temperature dependences of the thermal conductivity in $CuGeO_3$ and $Cu_{0.98}Zn_{0.02}GeO_3$ near the spin-Peierls transition are apparently due to actuation of an additional mechanism of phonon scattering, on critical fluctuations of the order parameter. The specific nature of the spin-Peierls compounds is that the density of states of the short-wavelength phonons increases as the transition temperature T_{sp} is approached.[10] Quasi-one-dimensional critical fluctuations which lead, specifically, to characteristic diffuse scattering of x rays[11] develop in spin-Peierls magnets long before static lattice distortions appear at T_{sp}. The appearance of such phonons as $T \to T_{sp}$ increases the probability of phonon–phonon interactions accompanied by umklapp processes, which is proportional to $(T - T_{sp})^{-1}$. However, as shown in Fig. 2, the experimental data are approximated best by a function $k(T) \sim (T - T_{sp})^{\alpha}$. In the case of $CuGeO_3$ $\alpha = 0.70 \pm 0.05$, and in the case of $Cu_{0.98}Zn_{0.02}GeO_3$ $\alpha = 0.76 \pm 0.03$. This means that as T_{sp} is approached from the high-temperature side, not only the mean free path of short-wavelength phonons but also the number of such phonons changes. It is interesting to note that the critical exponent α determined in this manner is close to the critical exponent $2\beta = 0.66$ determined from the intensity I of the additional crystallographic reflections near the spin-Peierls transition temperature in $CuGeO_3$:[11] $I \sim \delta^2 \sim (T - T_{sp})^{2\beta}$, where δ is the order parameter corresponding to dimerization of the lattice. However, below T_{sp} the order parameter corresponds to static dimerization of the lattice, and above T_{sp} it corresponds to dynamic lattice fluctuations.

The thermal conductivity of spin-Peierls magnets cannot be compared directly with that of compounds undergoing a Peierls transition.[12,13] In compounds exhibiting a metal–insulator transition, conduction electrons play the main role in heat transfer processes near the transition and against their background the anomalies due to a change in the phonon spectrum of the crystal are weak. An analogy can be drawn between the behavior of the spin-Peierls magnets and the thermal conductivity of magnetic dielectrics.[14] The magnon subsystem in such materials can be manifested in heat transfer processes in two ways. First, magnons as independent quasiparticles can themselves transfer heat[15] and, second, the magnetoelastic interaction of magnons with phonons opens up an additional phonon scattering channel. Thus, in easy-plane antiferromagnets a minimum of the thermal conductivity, due to scattering of phonons by critical fluctuations of the magnon subsystem near the Néel point, was observed against the background formed by the phonon maximum. However, the magnon spectrum in easy-plane antiferromagnets contains a gapless branch, so that at low temperatures magnons can be excited together with phonons. In spin-Peierls compounds below the transition temperature, an energy gap opens up in the spectrum of magnetic excitations. This suppresses the spin–phonon interaction mechanisms.

This work was supported by the Russian Fund for Fundamental Research through Grant 96-02-19474.

[a)]e-mail: vvp@mig.phys.msu.su

[1] M. Hase, I. Terasaki, and K. Uchinokura, Phys. Rev. Lett. **70**, 3651 (1993).
[2] J. W. Bray, H. R. Hart, L. V. Interrante *et al.*, Phys. Rev. Lett. **35**, 744 (1975).
[3] I. S. Jacobs, J. W. Bray, H. R. Hart *et al.*, Phys. Rev. B **14**, 3036 (1976).
[4] S. Huizinga, S. Komandeur, J. Sawatzky *et al.*, Phys. Rev. B **19**, 4723 (1979).
[5] L. P. Regnault, M. Ain, B. Hennion *et al.*, Phys. Rev. B **53**, 5579 (1996).
[6] Y.-K. Kuo, E. Figueroa, and J. W. Brill, Solid State Commun. **94**, 385 (1995).
[7] M. Poirier and M. Castonguay, Phys. Rev. B **52**, 16058 (1995).
[8] M. Hase, Y. Sasago, K. Uchinokura *et al.*, J. Magn. Magn. Mater. **140–144**, 1691 (1995).
[9] F. G. Aliev, V. V. Praydun, and L. I. Leonyuk, Preprint No. 26 [in Russian], Department of Physics, Moscow State University (1989).
[10] M. Arai, M. Fujita, K. Ubukata *et al.*, J. Phys. Soc. Jpn. **63**, 1661 (1994).
[11] Q. J. Harris, Q. Feng, R. J. Birgeneau *et al.*, Phys. Rev. B **52**, 15420 (1995).
[12] M. Kaveh, H. Gutfreund, and M. Weger, Phys. Rev. B **20**, 543 (1979).
[13] A. Smontara, K. Biljakovic, and S. N. Artemenko, Phys. Rev. B **48**, 4329 (1993).
[14] V. I. Ozhogin, A. V. Inyushkin, and N. A. Babushkina, J. Magn. Magn. Mater. **31–34**, 147 (1983).
[15] H. Sato, Prog. Theor. Phys. **13**, 119 (1955).

Translated by M. E. Alferieff